MINISTERE DE L'ENSEIGNEMENT SUPERIEUR ET DE LA RECHERCHE SCIENTIFIQUE
UNIVERSITE MOHAMED KHIDER - BISKRA
FACULTE DES SCIENCES ET DE LA TECHNOLOGIE
DEPARTEMENT DE GENIE ÉLECTRIQUE

*Thèse présentée en vue de l'obtention du diplôme de*

**Doctorat LMD en électrotechnique**

# *Contribution au diagnostic des défauts de la machine asynchrone*

Réalisé par: **GUEDIDI ASMA**

Soutenue publiquement le: 04/03/2024

**Devant le jury composé de:**

| | | | |
|---|---|---|---|
| Hammoudi Mohamed Yacine | MCA | Université de Biskra | Président |
| Guettaf Abderrazak | Professor | Université de Biskra | Rapporteur |
| Belhamdi Saad | Professor | Université de M'sila | Examinateur |
| Saadi Ramzi | MCA | Université de Biskra | Examinateur |

*Année Universitaire 2023/2024*

**ACKNOWLEDGEMENT**

First, I thank ALLAH for helping me throughout my research and enabling me to finish my thesis.

I would like to express my deep and sincere gratitude to my research supervisor **Pr. Guettaf Abderrazak** for his support, stimulating suggestions and encouragement helped me in all the time of research and writing of this thesis.

I would also like to thank deeply **Pr. Arif Ali**. It was a great privilege and honor to work under his guidance. I am extremely grateful for his listening and relevant advices.

I also want to say thank to all members of the jury. I am particularly grateful to **Pr. Hammoudi Mohamed Yacine** to participate as president of my Thesis Committee, and to **Pr. Belhamdi Saad** and **Pr. Ramzi Saadi** for accepting to report my thesis and for their advice, comments and questions.

I would like to thank particularly **Dr. Laala Widad**, **Pr. Bitam Salim**, **Pr. Zemmouri Noureddine**, **Pr. Titaouine Nacer**, **Pr Boumehraz Mohamed, Pr. Zouzou Salah Eddine**, **Pr. Ghoggal Adel** and **Pr. Ouafi Abdelkarim** for their support from both technical and human points of view during these years of intense work.

Guedidi Asma

I dedicate my dissertation work to my family, particularly my mother and my big brother Abdelrrafar.

**Abstract:**

Induction motors (IMs) are prevalent in both industrial and domestic applications. The implementation of an automatic condition monitoring system for IMs proves invaluable in detecting faults at their initial stages. This proactive strategy aims to prevent machinery malfunctions and potential catastrophic failures. Despite decades of research employing various approaches for IM fault diagnosis, the accurate identification of faults remains a complex task due to the intricate signal transmission paths and the influence of environmental noise. The primary objective of this thesis is to create an innovative intelligent system that enhances the reliability of health condition monitoring for induction motors (IMs) considering two cases: 1) The first one aims to design an automated fault diagnosis system utilizing ANN models to confront the complication of overlapping data in identifying broken rotor bar faults. Diverse signal processing techniques are incorporated into the system to refine and optimize the diagnostic accuracy for more effective fault detection. 2) The second one aims to create an automated fault diagnosis based on conventional neural network models. In this part, we focused on improving the performance of diagnostic systems. To this end, two solutions were proposed. Firstly, we aim to reinforce the quality of the images by merging the data images with the information map. Secondly, we focused on the architecture of an improved SqueezNet model associated with an attention block, which gives high precision in image classification. This model was validated by data relating to short-circuit and eccentricity faults. The results obtained are surprising.

**Key words**: Induction motor, mixed eccentricity, broken rotor bar, inter turn short circuit, discrete wavelet transform (DWT), variational mode decomposition (VMD), Artificial neural network (ANN), conventional neural network (CNN).

**Résumé :**

Les moteurs à induction (MI) sont répandus dans les applications industrielles et domestiques. La mise en œuvre d'un système de surveillance automatique de l'état des MI s'avère indispensable pour une détection précoce. Cette stratégie proactive vise à prévenir les dysfonctionnements des machines et les pannes potentiellement catastrophiques. Malgré des décennies de recherche utilisant diverses approches pour le diagnostic des défauts de MI, l'identification précise des défauts reste une tâche complexe en raison des chemins de transmission complexes des signaux et de l'influence du bruit ambiant. L'objectif principal de cette thèse est de créer un système intelligent innovant qui améliore la fiabilité de la surveillance de l'état de santé du moteurs à induction en considérant deux cas : 1) Le premier vise à concevoir un système automatisé de diagnostic de pannes utilisant des modèles de ANN pour faire face aux complication des données qui se chevauchent dans l'identification des défauts

comme la cassure des barres de la cage d'écureuil, l'excentricité et le court-circuit. Diverses techniques de traitement du signal sont intégrées au système pour affiner et optimiser la précision du diagnostic pour une détection plus efficace des défauts. 2) Le second vise à créer un diagnostic de panne automatisé basé sur des modèles de réseaux neuronaux conventionnels. Dans cette partie, nous nous sommes intéressés à l'amélioration des performances des systèmes de diagnostic. À cette issue, deux solutions ont été proposées. En premier temps, on vise à renforcer la qualité des images par la fusion des images de données avec la carte d'information. Dans un second temps, nous nous sommes concentrées sur l'architecture d'un modèle amélioré de SqueezNet associé avec un bloc d'attention qui donne une grande précision dans la classification des images. Ce modèle a été validées par des données relatives aux défauts de court-circuit et d'excentricité. Les résultats obtenus sont surprenants.

***Mots-clés :*** Moteur asynchrone, Excentricité mixte, cassure de barres rotoriques, court-circuit, transformée en ondelettes discrète (*TOD*), variationel mode décomposition (VMD), réseaux de neurone artificiel (RNA), réseaux de neurones conventionnel .

## ملخص :

الآلات الغير متزامنة (IMs) منتشرة في كل من التطبيقات الصناعية والمنزلية. إن تنفيذ نظام مراقبة الحالة التلقائي للـ IMs يثبت أنه لا يقدر بثمن في اكتشاف الأخطاء في مراحلها الأولية. وتهدف هذه الاستراتيجية الاستباقية إلى منع حدوث أعطال في الآلات، وانخفاض الإنتاجية، والفشل الكارثي المحتمل. على الرغم من عقود من البحث الذي يستخدم أساليب مختلفة لتشخيص أخطاء الرسائل الفورية، فإن التحديد الدقيق للأخطاء يظل مهمة معقدة بسبب مسارات نقل الإشارة المعقدة وتأثير الضوضاء البيئية. الهدف الأساسي من هذه الأطروحة هو إنشاء نظام ذكي مبتكر يعزز موثوقية مراقبة الحالة الصحية للمحركات الغير متزامنة مع الأخذ في الاعتبار حالتين: 1) يهدف الأول إلى تصميم نظام تشخيص الأخطاء الآلي باستخدام نماذج ANN لمواجهة المشكلة. تعقيد البيانات المتداخلة في تحديد أخطاء القضيب الدوار المكسورة. تم دمج تقنيات معالجة الإشارات المتنوعة في النظام لتحسين دقة التشخيص وتحسينها من أجل اكتشاف الأخطاء بشكل أكثر فعالية. 2) يهدف الثاني إلى إنشاء تشخيص تلقائي للأخطاء بناءً على نماذج الشبكات العصبية التقليدية. في هذا الجزء، ركزنا على تحسين أداء أنظمة التشخيص. وتحقيقا لهذه الغاية، تم اقتراح حلين. أولاً، نهدف إلى تعزيز جودة الصور من خلال دمج صور البيانات مع خريطة المعلومات. ثانياً، ركزنا على بنية نموذج SquezNet المحسن المرتبط بحجب الانتباه والذي يعطي دقة عالية في تصنيف الصور. تم التحقق من صحة هذا النموذج من خلال البيانات المتعلقة بأخطاء الدائرة القصيرة والانحراف .النتائج التي تم الحصول عليها مثيرة للدهشة.

***كلمات مفتاحية :*** الآلات الغير متزامنة، الانحراف المختلط، انكسار القضبان، دائرة مقصورة، التحويل المويجي المتقط، تحلل الوضع المتغير، الشبكات العصبية الاصطناعية، الشبكات العصبية التقليدية.

# List of figures

# List of tables

# Abréviations List

AI : Artificial intelligence
ANN : Artificial neural network
CNN; Convolution neural network
CPU: Central Processing Unit
DL: Deep learning
DWT: Discret wavelet transform
EMD : Empirical mode decomposition
EPRI: Electrical Power Research Institue
FFT: Fast Fourier transform
FN: False negatif
FP: False positif
GPU: Graphics Processing Unit
HHT: Hilbert-Huang Transform
HR: High resolution
HT: Hilbert transform
ILSVRC: ImageNet Large Scale Visual Recognition Challenge
IMF: Intrinsic Mode Function
ITSC: Inter turn short circuit
LSTM: Long Short-Term Memory Networks
MCSA: Motor current signature analysis.
ML: Machine learning
MLP: Multi-layer perceptron
PSD: Power Spectral Density
ResNet: The Residual Network
STTLS: Short Time Total Least Square
TL: Transfer Learning
TN: True negatif
TP: True positif
T-SNE: t-distributed stochastic neighbor embedding
VMD: Variational mode decomposition
VGG: Visual Geometry Group (VGG)

## *Summary*

## *Chapter II : Advanced signal processing methods dedicated to the diagnosis of asynchronous machine*



## *Chapter III : Machine Learning and Deep Learning*

## *Chapter IV : Fault diagnosis of broken bars using STTLS-Music and ANN*

## *Chapter V : Diagnostic of airgap eccentricity and ITSC by CNN*



## *Case study 1: diagnostic of airgap eccentricity using VMD and CNN*



## *Case study 2: diagnostic of inter turn short circuit (ITSC) fault using VMD and CNN*

# General Introduction

## 1. Context

Powered by the convergence of smart manufacturing, industrial big data and industry 4.0 innovations, the contemporary industrial landscape is witnessing a new revolution from traditional manufacturing industry to intelligent manufacturing industry [JIN 20]. Detecting abnormalities or faults is a critical aspect of smart manufacturing systems in Industry 4.0. This is because faults often do not lead to an immediate system shutdown but can potentially disrupt the entire production process, making their early identification crucial [Pai 21]. The industrial internet of things (IIoT) is expanding, and industries are actively seeking to harness its potential. Manufacturing process data is being gathered for various analytical purposes [PRI 20]. Nonetheless, the extensive big data generated by modern industries presents an unparalleled chance to gain a comprehensive insight into machine conditions. Consequently, it is crucial to capitalize on this opportunity and enhance diagnostic techniques to ensure precise assessment and prompt action when it comes to machine deterioration and breakdowns.

Modern industrial applications use squirrel cage induction motors (SCIM) due to their simplicity of construction, their specific power, their robustness, their relatively low cost. However, despite these advantages, it does not escape failures which can harm its operation and lead to its shutdown. These faults can be of electrical, mechanical or environmental origin. Consequently, it is recommended to detect a defect early in order to remedy it as quickly as possible and thus minimize the induced effects (stoppage of a production line, loss of products, etc.

Artificial intelligence (AI) tools, such as machine learning (ML) and deep learning (DL), have the potential to serve as crucial components in the early detection of faults in squirrel cage induction motors (SCIMs) and in the realization of Industry 4.0 goals. ML and DL algorithms are used to analyze the vast amounts of data generated by industrial processes. Nonetheless, there is a need for performance enhancement to ensure a precise diagnosis. This thesis is concerned with challenges associated with enhancing diagnosis systems, particularly those pertaining to data quality issues. The upcoming section will delve into the resolution of these problems.

## 2. Problem statements

In this thesis, our focus revolved around the challenge of creating an accurate intelligent diagnostic system using machine-learning (ML) techniques. To start, our primary objective is to delve into the field of fault diagnosis for induction motor using machine-learning techniques, particularly focusing on neural network models. As known, classical ML models like Support Vector Machine (SVM) and k-Nearest Neighbor have made notable strides in recent years. Nevertheless, they continue to exhibit certain limitations when confronted with the heightened demands of the industrial sector [Jia 2019]. For instance: i) These approaches often require manual feature extraction and selection, which poses limitations in complex big data analysis. ii) The processes of feature mining and decision-making are typically designed separately, resulting in unsynchronized optimization that consumes significant time and hampers performance. iii) As sensors become more diverse and machines more complex, coupled with the increasing volume of data characterized by higher dimensions and dynamics, traditional algorithms struggle to deliver satisfactory diagnostics [FAH 20]. Hence, one of the main research question tackled in this section is:

RQ1: How to deal with the limitations imposed by machine learning to create a robust intelligent system based on neural networks for detecting rotor broken bar faults?

In the second part of this thesis, our research is directed towards the automated classification of various inter-turn short circuit (ITSC) and air-gap eccentricity (AGE) faults using deep learning techniques applied to image data. Classifying the severity of ITSC and AGE from image data poses a challenge because visual features exhibit significant similarity in terms of both shape and color. In addition, the lack of data in training CNN models can result in overfitting and limited generalization. Hence, two key research questions addressed in this section are:

RQ2: How does the quality of data affect the performance of AGE and ITSC faults detection ?

RQ3: What strategies can be employed to address the lack of AGE and ITSC fault data ?

## 3. Contributions

In response to the previously mentioned challenges, two contributions are proposed: The first contribution seeks to create a novel automated fault detection system based on Music and artificial neural network (ANN) for rotor broken bars. The proposed approach encompasses three primary task: (a) a pre-processing phase aimed at enhancing data quality by reducing the impact of noise. (b) A feature extraction and selection step based on an embedded method (the improved music method). Finally, the performance of this artificial neural network classifier underwent thorough validation and verification.

The second contribution proposes an improvement SqueezNet combined with advanced signal processing method to diagnosis AGE and ITSC faults. In fact, this method comprises three fundamental components: a novel multi-sensor fusion technique, a knowledge map, and enhanced Convolutional Neural Networks (CNNs). Initially, raw data from various sensors undergoes a transformation into 2D data utilizing a unique image transformation method based on the Hilbert transform (HT) and variational mode decomposition (VMD). These transformed data are then concatenated with a novel information map containing both frequency fault information and rotational speed details. Subsequently, this resulting 3D multi-information image serves as input to an improved CNN model, which applies transfer learning based on an enhanced version of SqueezNet. This enhanced CNN model incorporates a novel attention mechanism module to precisely identify fault-related features.

## 4. Dissertation plan

The structure of this thesis is as follows:

The first chapter presents a state of the art that succinctly introduces various machine faults and provides an overview of commonly employed diagnostic methods for these faults. In the second chapter, an overview of signal processing methods used in diagnosis is presented, discussing their strengths and weaknesses. Chapter three provides an overview of artificial neural network and deep learning algorithms and methods. The fourth chapter deals with an experimental method for rotor broken bar diagnosis by combining TLS-music method and ANN for the development of a robust and powerful diagnostic system. In Chapter five, we introduce the primary contribution, which is focused on developing a precise classification method for ITSC faults based

on convolutional neural network. First, we integrate an information map to enhance the model performance by incorporating domain knowledge into the data-driven model. We introduce a novel self-attentive learning network designed to effectively capture the characteristics of ITSC faults in a robust manner. Finally, the thesis is concluded with a summary of contributions and a discussion of future possibilities and perspectives.

Chapter 1

# State of the Art

## I.1 Introduction

Currently, asynchronous machines are considered the most widely used electromechanical conversion tool in the industrial environment. This is justified by its simplicity of construction, its low purchase cost and its mechanical robustness. Despite its qualities, it undergoes a certain number of electrical, mechanical and chemical stresses during its life which can make it potentially faulty, which leads to an irreparable shutdown resulting in considerable economic losses. Hence the need for constant monitoring of the state of this device [MON 09]. Therefore, it is essential to develop an accurate diagnostic systems to detect in an early stage the faults that may occur in this type of machinery.

Proper monitoring of this machine requires a faults knowledge that include in particular its frequency characteristics and all the operating information of the motor in the both healthy and faulty states.

After these considerations, we will begin this chapter by recalling the various elements constituting this machine. Then we will present the different faults that can occur on each of them. At the end of this chapter, we discuss the diagnostic methods applied to the asynchronous machine.

## I.2 Constitution of the asynchronous machine

The asynchronous machine, also known as induction motor, is an electric machine allowing the conversion of energy by electromagnetic induction. It is composed of several components that work together to produce the rotational motion Fig I.1. It consists of several components that work together to produce a rotational motion. Some of the main mechanical parts of an induction motor are detailed below.

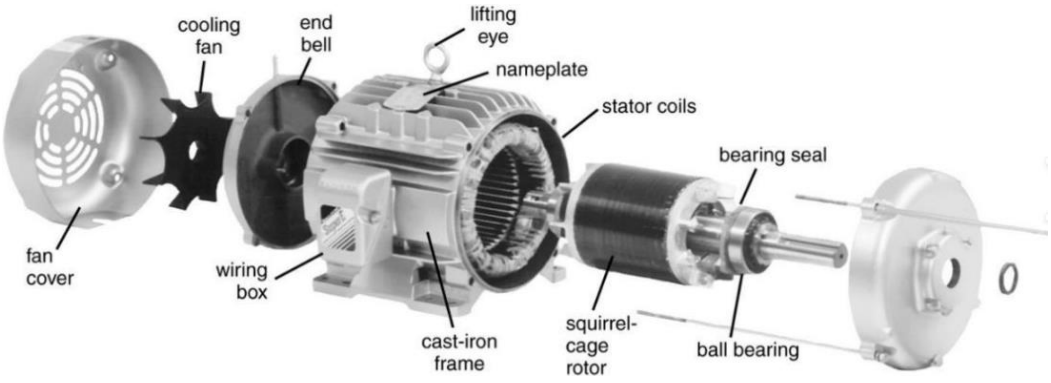


**Fig. I.1:** Exploded view of a squirrel cage induction motor [LAA 17].

### I.2.1 Stator

The stator is the fixed part of the induction motor. It is made up of a sheet metal carcass on which is fixed a stack of identical ferromagnetic sheets which constitute a hollow cylinder Fig. I.2. The

laminations of the magnetic circuit are dug on their inner periphery to form notches in which are housed identical coils which form a set of windings [WID 17]. The windings are clamped in the notches by fiber cables. Then, everything is dipped in a hot varnish which penetrates to the bottom of the notches and impregnates the entire windings. The insulation between the electrical windings and the steel sheets is done using insulating materials which can be of different types depending on the use of the asynchronous machine [DID 04]. The windings can be inserted in nested, wavy or even concentric ways. Concentric winding is very often used when the winding of the machine is mechanically carried out [MON 09].

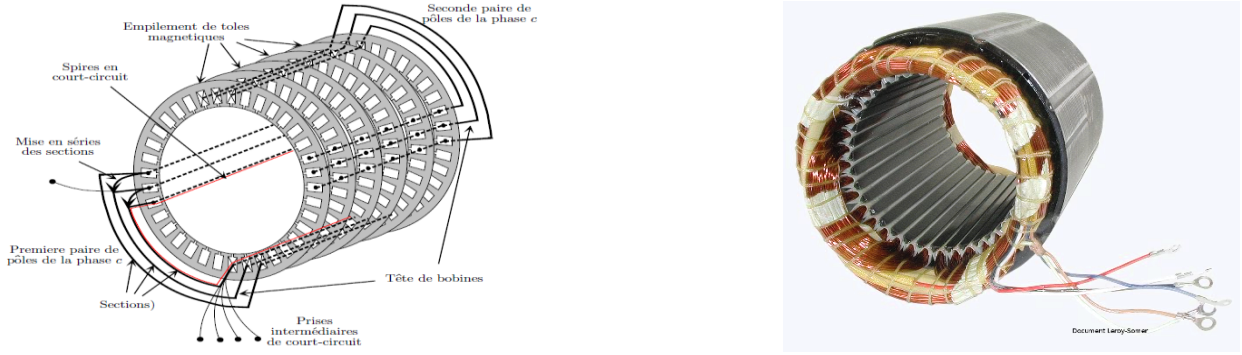


**Fig .I.2** Left Schematic representation of the asynchronous machine. Right: Photo of an asynchronous motor [DID 04]

### I.2.2 Rotor

The rotor is the rotating part of the induction motor, which allows the rotation of the mechanical load. The rotor magnetic circuit consists of a stack of steel sheets, generally of the same origin as those used for the construction of the stator. The rotor is separated from the stator by a very fine air gap of the order of 0.4 to 2 mm [MON 09]. The rotors of asynchronous machines can be of two types: wound or squirrel cage Fig I.3. Wound rotors are constructed in the same way as stator windings (inserting the windings into the rotor slots). The rotor phases are then available thanks to a system of brush rings positioned on the shaft of the machine. In the case of squirrel-cage rotors, the conductors are made by casting an aluminum alloy, or by preformed solid copper bars laminated into the rotor laminations [MED12]. There is generally no, or very little, insulation between the rotor bars and the magnetic laminations. Often these bars are uniformly inclined with respect to the axis of the motor. This arrangement has the effect of considerably reducing sub-harmonics and noise during the acceleration of the machine and giving a more uniform start-up and acceleration [DEV 02].

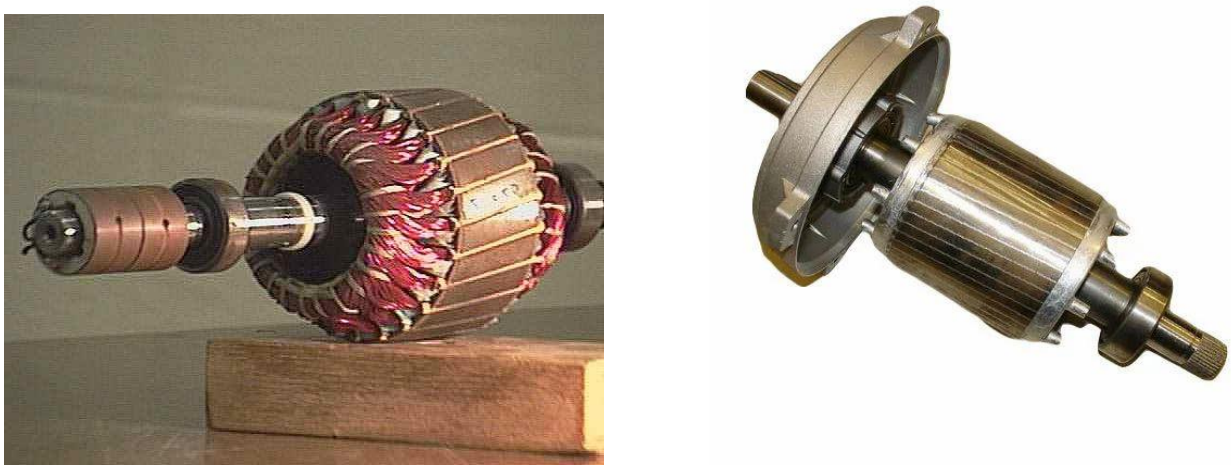

(a) (b)

**Fig I.3** a) Photo of wound rotor, b) Photo of squirrel cage rotor [LAA 17].

### I.2.3 Mechanical organ

The cast iron frame serves as a support, it acts as an envelope and provides protection against the external environment. The shaft is a transmission device which transmits the rotational motion from the rotor to the load. The end bell typically houses the bearings that support the rotor shaft, which allow the rotor to rotate smoothly. The end bell is usually made of a strong material such as cast iron or aluminum and is attached to the engine frame with bolts Fig I.1. It can have a smooth or ribbed surface for increased rigidity and cooling efficiency.

## I.3 Statistical study of MAS failures

Several statistical studies have been carried out on the reliability of electrical machines made by different industry groups.

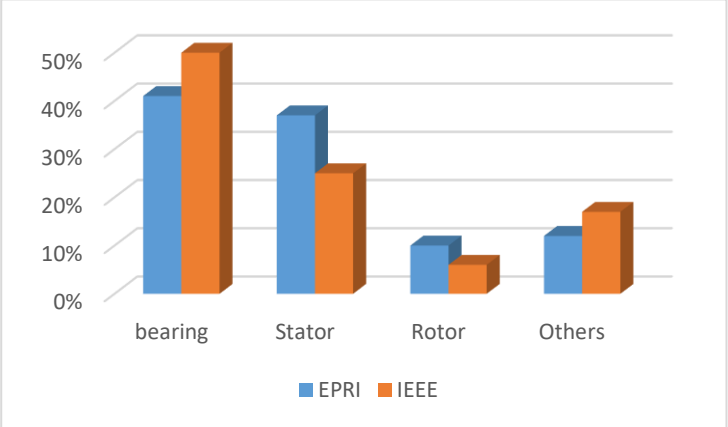


**Fig. I.4:** Breakdown rate distribution in asynchronous machines.

The main study, carried out by the company "General Electric", was published in EPRI (Electric Power Research Institute) in 1982; it covers approximately 5000 motors, of which approximately 97% were asynchronous three-phase squirrel-cage motors [ALI 09]. Figure I.4 summarizes the results of this study together with the results obtained from IEEE-IGA. Although each of these two studies concerns machines of varying power and operating under different conditions of use, the distribution tendencies are quite consistent. In both case studies, the results showed that the highest rates are for motor bearings, followed by stator faults and then rotor faults. [MON 09].

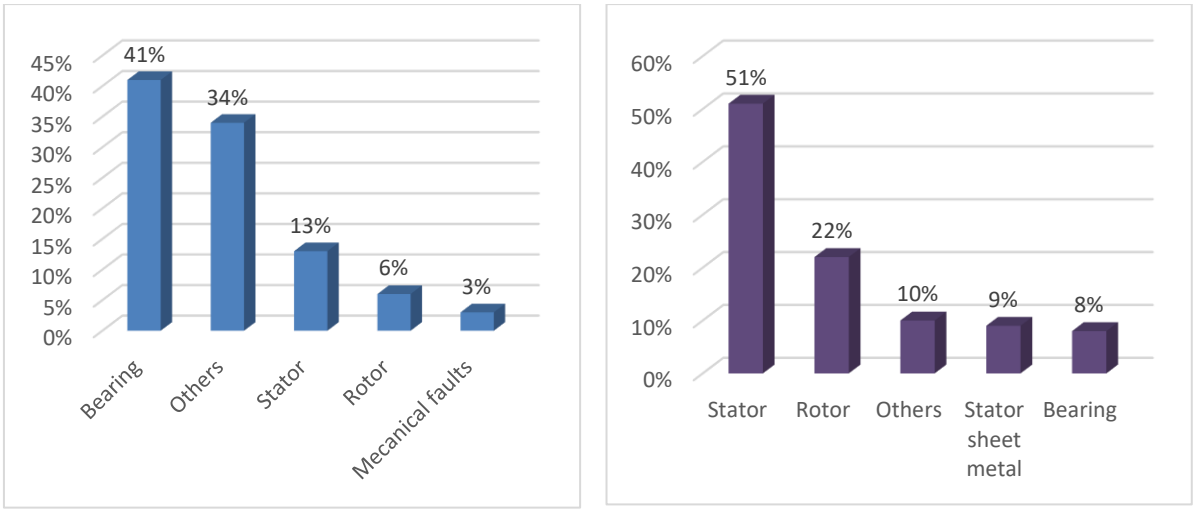


**(a)** **(b)**

**Fig. I.5:** Distribution of breakdowns for a) high-powered machines, b) medium-powered machines

Figure I.5 represents the results of statistical studies made by [THO 95, OND 06] and a German insurance company for industrial systems [ALL 88, BOU 01]. The first study is carried out on high power machines (from 100 kW to 1MW) while the second on machines concerns medium-power asynchronous (from 50 kW to 200 kW).

## I.4 Types of asynchronous machine faults

Failure occurs when the system fails to perform its function or achieve the expected performance according to the technical specifications. The alteration or cessation of the system ability to perform its required functions can be caused by various factors such as design errors, manufacturing defects, maintenance errors or extreme environmental conditions. It is important to note that a failure is the real consequence of faults, in particular when their occurrence is of a destructive nature for the main function of the system. In this section, we are interested in

identifying common faults of a squirrel cage asynchronous motor. These faults may be of electrical, mechanical or environmental origin. According to [BON 86. SID 05; SHA 15; KAM 16], faults can be classified according to their origin into two types as shown in Tab I.1: internal and external. Internal machine faults are caused by machine components (rotor and stator magnetic circuits, windings stators, mechanical air gap, rotor cage, etc.). While, the external faults sources are located outside the electric motor, but their consequences may cause damage to it. These malfunctions can be caused either by the supply voltages and the mechanical load, or by the environment of the use of the machine [MED 12].

Table I.1: Internal and external machine faults

| | | | |
|---|---|---|---|
| Failures of electrical machines | Internal defects | Mechanical | Stator/rotor friction |
| | | | Eccentricity |
| | | | Bearing defect |
| | | | Movement of conductors |
| | | Electrical | Stator faults |
| | | | Rotor faults |
| | | | Magnetic circuit fault |
| | | Thermal | insulation failure |
| | External defects | Mechanical | Bad assembly |
| | | | Machine overload |
| | | | Torque pulses |
| | | Electrical | Voltage transient |
| | | | Voltage fluctuation |
| | | | Voltage imbalance |
| | | Environmental | Temperature |
| | | | Humidity |
| | | | cleanliness |

It should be noted that the power supply of electrical machines also cause failures. The excitation of the windings by voltages with steep fronts (also known as voltage surges or transients) can indeed accelerate the aging of the insulation of the stator winding. For example, the excitation of the windings by voltages with steep fronts (also known as voltage surges or transients) can indeed accelerate the aging of the insulation of the stator winding. Voltage surges occur due to various reasons, such as lightning strikes, switching operations, and other electrical disturbances. When voltage surges occur, they cause high voltages to be applied to the windings, which can lead to partial discharges within the insulation. These partial discharges can cause small cavities within the insulation, which can grow over time and lead to the breakdown of the insulation. In this present work, we will be interested in the diagnosis of three faults of the asynchronous machine which are: broken bars fault, static and dynamic eccentricity faults and bearing faults. There are multiple causes of stator and rotor faults. A brief description of the most frequent faults is given in the following paragraphs.

### I.4.1 Stator faults

The stator windings are the most vulnerable parts to electrical faults and operating incidents. The most stator faults are attributed to insulation degradation. In fact, the rupture of this insulation can cause a permanent short circuit between turns of the same phase, a short circuit between two phases or a short circuit between phase and the metal frame. These faults most often have a mechanical origin (excessive vibrations, electrodynamic forces on the conductors), electrical (surface discharges, overvoltage) and thermal (overheating) [MON 09]. The most frequent cause of short-circuits between turns of the same phase, which can appear in the notches (Fig I.6. a) or at the level of the coil heads (Fig I. b), is too great a rise in temperature. This fault can lead to an increase in the current flowing in the winding concerned with a slight effect on the amplitude of the other phases [HEN 03, KHE 09, RED 17].

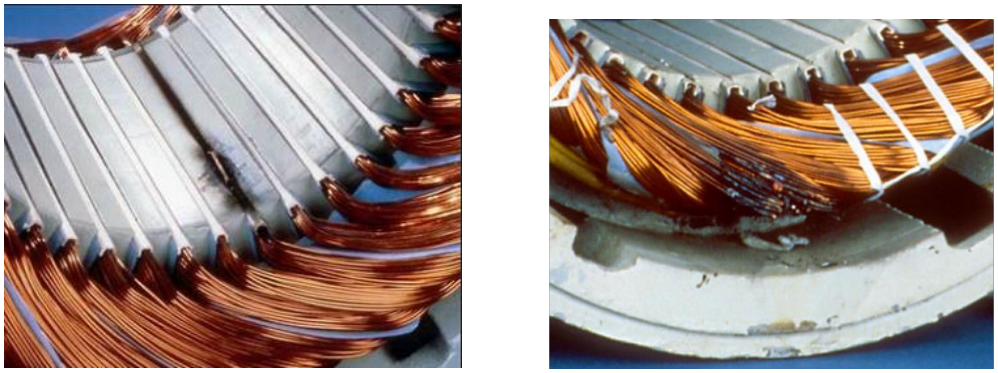

(a) (b)

**Fig I. 6** Failures in Stator Windings [KHA12]

### I.4.2 Rotor failure

#### I.4.2.1 Rotor broken bar and rings faults

The bar break fault is one of the most common rotor faults. Indeed, the cage is made up of aluminum or copper short-circuit bars and rings. Short circuit rings are the most sensitive to electrical faults. This is well justified because the currents circulating in these components are greater than those in the rotor bars. A failure in the rotor cage is usually located at the joint between a bar and ring as shown in Fig I.7. A total or partial rupture of one bar can be considered as an electrical rotor fault [DID 04]. This defect also has a cumulative effect. In fact, the current carried by a bar before being broken is distributed over the adjacent bars. These bars are then overloaded, which leads to their failure, and so on until the failure of a sufficiently large number of bars to cause the machine breakdown.

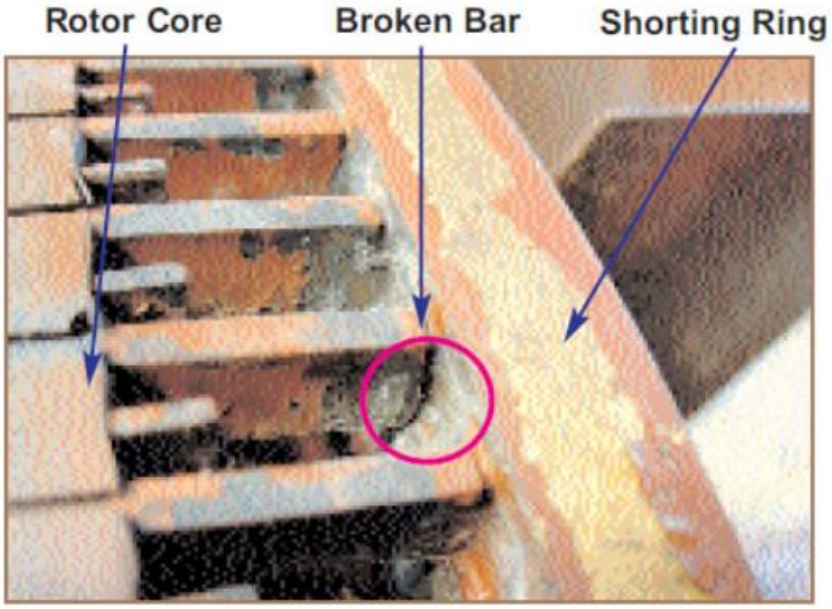


**Fig. I.7:** Rotor broken bars fault of an asynchronous motor [THO 95]

The probable causes of the rotor broken bars and rings can be due to several phenomena [DID 04];

- **Too frequent starts:** It is well known that during starts, the rotor current can reach ten times the nominal current, which causes excessive heating in the rotor circuit. The starting time is also characterized by minimal cooling and high mechanical forces, which overload the rotor bars.
- **Manufacturing defects:** For an injected rotor, physical defects can occur at the manufacturing stage due to molding defects, poor welding between the bars and the rings,

air bubbles between the layers that increase the electrical resistance of the bars. Therefore, there may be weak points in the bars; which can lead to a complete rupture of the latter.

- **Mechanical causes:** excessive vibration, shock in service.
- **Environmental constraints** caused by contamination or abrasion of the rotor cage.

### I.4.2.2 Eccentricity

The eccentricity of an electric machine is defined as an unequal air gap which exists between the stator and the rotor [LIU 21]. It is a phenomenon that exists from its manufacture and evolves over time. In practice, an air-gap eccentricity of up to 10% is tolerated [KAN 14]. Nevertheless, manufacturers usually try to keep the total eccentricity level even lower to reduce the magnetic attraction unbalance and to minimize vibration and noise [GHE 21]. The main cause which risks aggravating the eccentricity is the radial forces exerted on the shaft of the machine. In fact, the inherent offset generates an imbalance in the distribution of these forces between the stator and the rotor. These forces will be maximum where the thickness of the air gap is minimum. This fact can lead to friction between the rotor and the stator [KUM19], which can result in motor breakdown (Fig I.8).

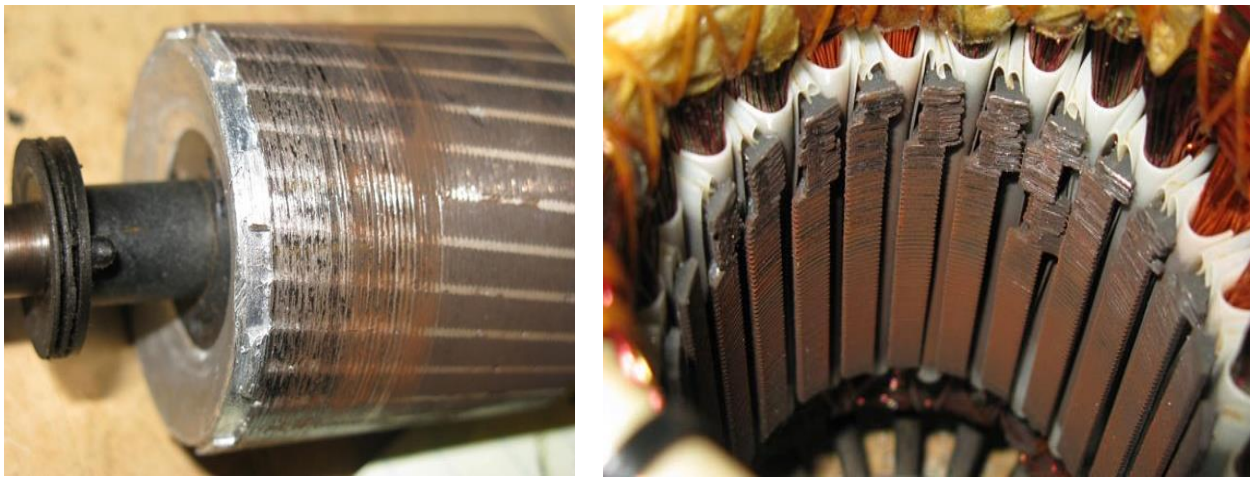

**Fig. I.8:** Examples of damage to the stator and rotor due to eccentricity fault in an asynchronous motor [KHA 12]

Generally, there are three types of eccentricities [LIU 21]:

- **Static eccentricity**

Static eccentricity occurs as a result of the ovality of the stator iron or the incorrect positioning of the rotor caused by the misalignment of the rotation rotor axis with respect to the axis of the stator during the construction phase [KLE 22] as shown in Fig I .9.a.

- **Dynamic eccentricity**

Dynamic eccentricity occurs as a result of the bending of the rotor shaft, bearing wear, and mechanical resonance [OKS 00]. In this case, the rotor center is not at its center of rotation figure (I.9.b) and therefore the position of minimum air gap thickness rotates with the rotor [AND 08, NAN 11]

- **Mixte eccentricity**

In reality, static and dynamic eccentricities tend to coexist figure. (1.6c). Even in good condition, the machine still has a certain degree of residual mixed eccentricity due to inevitable manufacturing errors [AND 08, NAN 11].

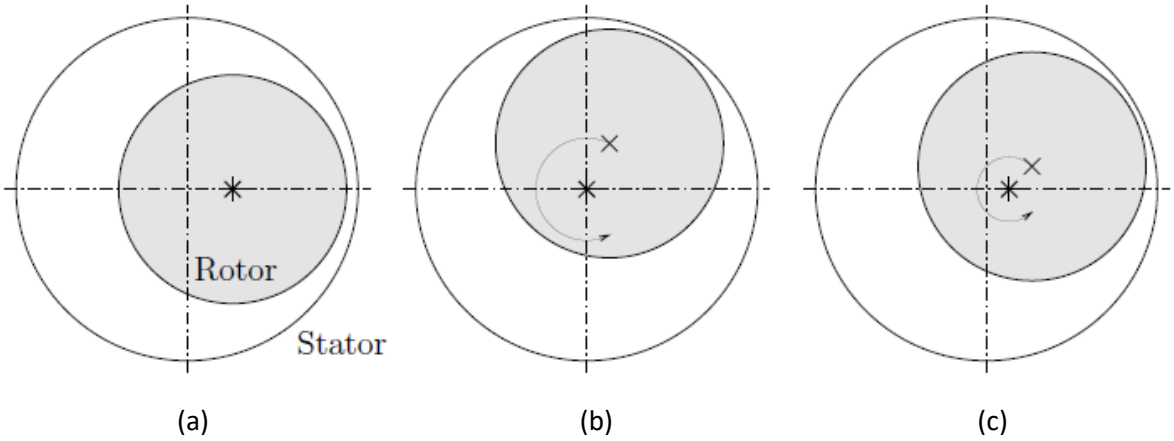


**Fig. I.9:** Types of eccentricity a) static b) dynamic) mixte [AND 12]

### I.4.2.3 Bearing fault

Rolling element bearings are one of the most widely used elements in machines and their failure is the single biggest cause for machine breakdowns [ERE 17]. The statistical studies presented in Figures (I.4 & I.5) show that the failures attributable to ball bearings are most dominating regardless of the considered machinery power range. They account for 40 and 50% of all machine failures. There are many types of bearings used in various applications. Each type of bearing has its own specific characteristics in terms of radial and axial loads supported, speed limit or allowable misalignment. In general, bearings are made up of four essential components, the outer ring, the inner ring, a row of balls held by a cage, as well as grease for lubrication [TRA 10]. Exploded view of the components of a single-row of roller bearing is presented in figure I.10.

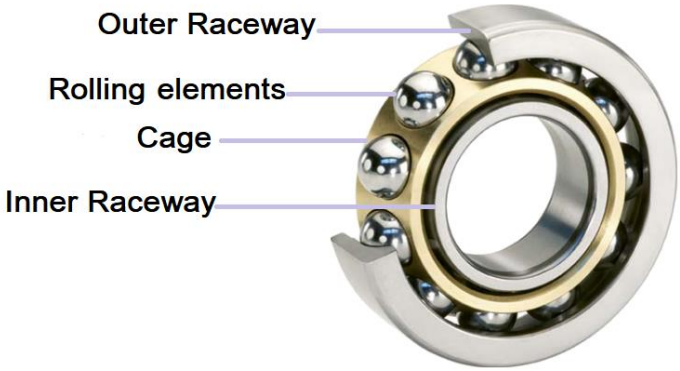


**Fig. I.10:** Exploded view of roller bearing [BAI 17]

The service life of a bearing is in fact a statistical data characterizing the number of operating cycles, under a specific stress, that the bearing can carry out before presenting a failure. It is important to note that the rated life is only an estimate and the actual life can vary considerably depending on the conditions of use and maintenance. Bearings that are subjected to high loads and speeds or that are used in severe environmental conditions may have a shorter life. Many external factors of bearings, which contribute to their wear and a reduction in their service life, will be described in a non-exhaustive manner.

- **Effects of Mechanical Stress:** The radial and axial mechanical stress can cause premature bearing wear. In fact, when the forces exerted on the bearing are too high, cracks, peeling of the raceways or balls may occur, which leads to increased wear [TRA 09].

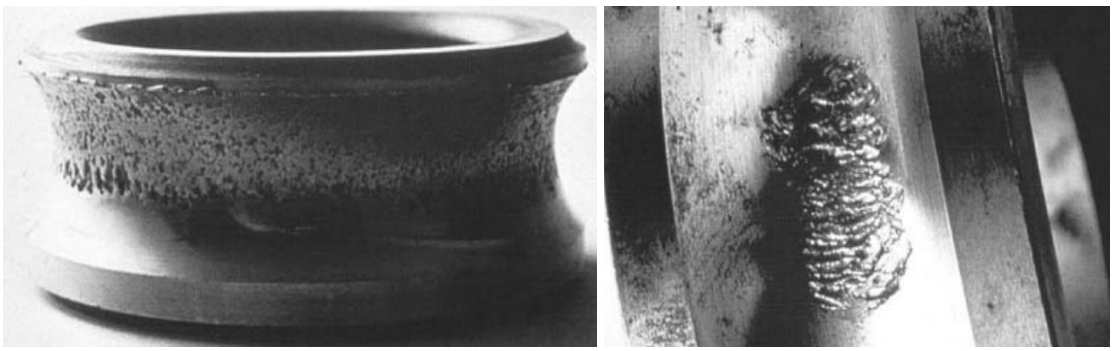

**Fig. I.11:** Degradation of the bearing raceway due to mechanical overloads [TRA 09].

- **Corrosion:** The bearing can be affected by corrosion if the rolling elements, rings and cage of the bearing are exposed to corrosive conditions. In the presence of a corrosive agent,

such as humidity, salt, acids or corrosive chemical products, the metallic materials constituting the bearing degrade; which leads to the reduction of the load capacity of the bearing [TRA 09].

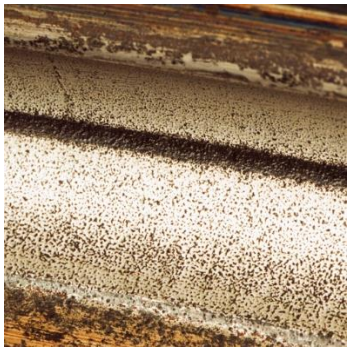

**Fig. I.12:** Pitting on the track surface due to corrosion [TRA 09].

- **Contamination:** Contamination is one of the main causes of bearing failure [POD 19]. When machines operate in contaminated environments, foreign particles such as dirt, dust, debris, and scrap metal can accumulate in the bearing and cause cracking or even chipping of bearing components.

- **Lubrication:** The lubricant is an essential element in the bearing, it helps to protect the metal surfaces at the ball-ring contacts. A lack of lubrication can lead to corrosion of the metal surfaces of the bearing, which can weaken the structure and cause irreversible damage [BEL 20]. In addition, a lack of lubricant can cause noise and vibration in the bearing, which affects the entire system.

**Fig. I.12:** Degradation caused by the deterioration of the lubricant [CAN 07].

- **Circulation of electric current**: As the bearings are metallic, an electric current can flow from the outer ring to the inner ring via the balls. The presence of lubricant at the level of the contacts leads to the appearance of a dielectric capacity; at the terminals of which a homopolar potential appears. When the latter is too great, a dielectric discharge phenomenon occurs; leading to the appearance of micro holes on the rolling surfaces at the points of discharge [SRA 09] as shown in Fig I.13.

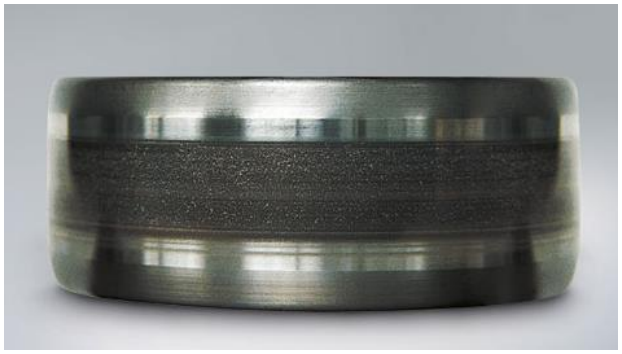

**Fig. I.13:** Effect on bearing of the flow of electric current [TRA 09]

## I.5 Spectral signatures of faults in the asynchronous machine

### I.5.1 Signatures of rotor slot harmonics

The magnetic induction in the air gap of squirrel cage motors is not necessarily sinusoidal. It can vary according to several parameters such as the arrangement of the stator winding, the spatial distribution of the magnetic materials in the magnetic circuit and the structure of the rotor cage. This structure can lead to the production of harmonics in the spectrum of the stator current, known as rotor slots harmonics (RSH), having the frequencies [DIA 22, YU 22]:

$$f_{he} = \left[ \frac{kN_b}{p}(1-g) \pm n_{ws} \right] f \qquad \text{(I.1)}$$

with , $n_{ws} = (\pm 1, \pm 3, \pm 5, \ldots)$, p is the pairs poles number, Nb is the rotor bars number,

$n_{ws}$ is the airgap magneto-motive force time harmonics order, and k is a positive integer. For k=1 and $n_{ws} = 1$, we define the harmonics of the main slots (Principal Slots Harmonics 'PSH').

### I.5.2 Signatures of stator faults

Stator faults can be caused by various reasons, such as insulation degradation which can be functional degradation related to aging or due to operating conditions and mechanical, thermal, electrical and environmental stresses. They usually start with a short-circuit between turns, before

progressing to more serious faults. The most common types of stator faults are phase-to-earth short-circuit faults, phase-to-phase short-circuit and turn-to-turn short-circuit.

Short-circuit diagnosis is based on the detection of frequency components given by the following expression [ALI 22]:

$$f_{st} = \left[ k \pm \frac{n(1-g)}{p} \right] f \qquad \text{(I.2)}$$

with k =1,3 et n = 1, 2,3, … (2p – 1) .

because this rotating flow wave is at the origin of the equivalent current components in the stator winding [KHA12]. We also find the so-called time harmonics 150 Hz, 250 Hz , which also appear in the case of a short-circuit between turns, and which are often present in any impedance imbalance, such as voltage imbalance.

### I.5.3 Signatures of rotor broken bar faults

A defect in the bar rotor will generate a kind of asymmetry which affects the configuration of the rotor, this fact leads to the decomposing of the distorted rotor magnetic field into a positive and a negative sequence rotating magnetic field. The negative sequence rotating magnetic field induces fault component with a frequency of $f_{lbc} = (1-2g)f$ in the stator winding [hindawi2]. Another component also appears in the stator current spectrum at a frequency $f_{rbc} = (1+2g)f$ . This component is due to speed fluctuations caused by torque oscillations [HAL 22]. In short, the presence of a broken bars, the spectrum of the statoric current contains lateral components on either side of its fundamental component whose frequencies are given by:

$$f_{rbc} = (1 \pm 2kg)f \qquad \text{with} \quad k = 1, 2, 3, . \qquad \text{(I.3)}$$

It should be noted that bar breaks generate frequency components in the torque and speed spectra given by $f_{rbc} = 2kgf$ ; k = 1,2 ,3,…

### I.5.4 Signatures eccentricity faults

As mentioned above, there is three type of eccentricity: static eccentricity (SE), dynamic eccentricity (DE) and mixed eccentricity (ME). The main origins of SE fault may be ovality of the stator core, inaccurate positioning of the rotor or stator at the manufacturing stage, wrong positioning and wearing of bearings. DE fault could be resulted from inclination of rotor shaft, wearing of bearings, mechanical resonance at critical speed, unbalanced magnetic pull (UMP)

brought about by SE and DE faults, shaft misalignment and unbalanced torque [FAI 16]. Some spectrum components are much more affected by eccentricity fault. These could be divided into two main groups: high frequency and low frequency. High frequency (HF) components are the sideband components around the principle slot harmonic (PSH) which are obtained as follows [THO 98] :

$$f_{ecc,HT} = \left[ \pm \upsilon + (kR \pm n_d) \frac{(1-g)}{p} \right] f \tag{I.4}$$

With k an integer, $\upsilon = 1, 2, 3, \ldots$ and $n_d$ is an eccentricity order. $n_d$ equal 0 for static eccentricity and 1, 2, 3, … for dynamic eccentricity.

It has been verified that in the case of ME fault, the following components are intensified :

$$f_{ecc,LF} = f \pm k f_r = f \pm k \frac{1-g}{p} f \tag{I.5}$$

With k positif integer.

### I.5.5 Signatures bearing faults

In a single row ball bearing, characteristic frequencies are associated with each element of the bearing, namely the outer ring, the inner ring, the balls and the cage [TRA 09]. These frequencies depend on the internal dimensions of the bearing, as well as the contact angle, and are given analytically by the equations (I.6)-(I.8). Fig I.14 schematizes the used notations.

$$f_{IR} = \frac{N}{2} \left( 1 + \frac{d_B}{d_p} \cos\theta \right) f_r \tag{I.6}$$

$$f_{OR} = \frac{N}{2} \left( 1 - \frac{d_B}{d_p} \cos\theta \right) f_r \tag{I.7}$$

$$f_{BA} = \frac{N}{2 d_B} \left( 1 - \left( \frac{d_B}{d_p} \cos\theta \right)^2 \right) f_r \tag{I.8}$$

With $f_{IR}$, $f_{OR}$, and $f_{BA}$ are the characteristic frequency of inner race, outer race, and ball faults, respectively, N is the number of rolling elements, $d_B$ is the rolling element diameter, $d_p$ is the pitch diameter, and $\theta$ is the contact angle.

Moreover, these frequencies are calculated from the approximation by considering that the ball/ring contacts are perfectly punctual and that the rolling of the balls is done without slipping. In real bearings, there is always rolling and sliding of the balls on the tracks at the same time.

When a localized defect appears at a point on one of the bearing elements, it causes a vibration at the characteristic frequency associated with the element in default.

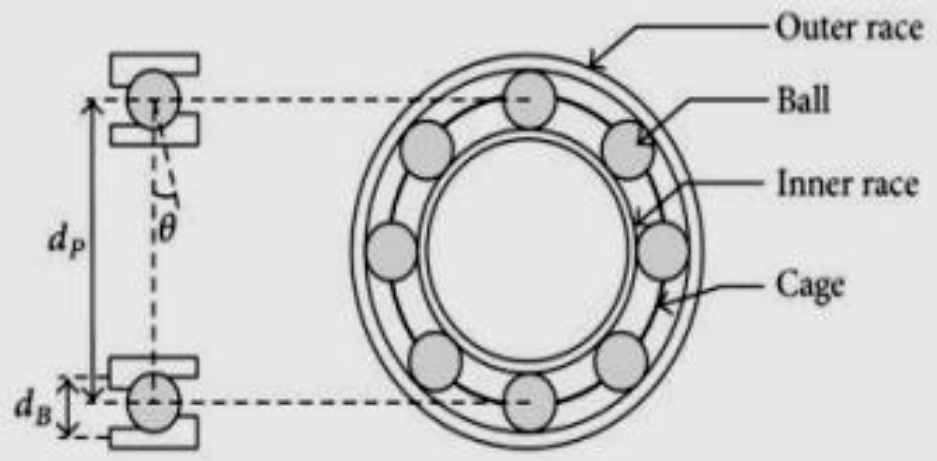


**Fig. I.14:** Structure and Dimensions of a bearing [LAA 17]

## I.6 Signals used for fault diagnosis in squirrel-cage induction motors

The primary objective of seeking fault signatures or indicators is to understand the system behavior by identifying the type and source of each fault accurately. In fact, the occurrence of electrical or mechanical faults in the induction motor lead to the modification of certain quantities characterizing the state of the machine. Manifestations of such defects are noticeable through several signals, the commonly used for fault diagnosis in squirrel-cage induction motors are presented in the following sections.

### I.6.1 Diagnostic by the use of stator current

Electrical motor stator current signals have been widely used to monitor the condition of induction machines and their downstream mechanical equipment. Numerous research works have demonstrated that analyzing the spectrum of the stator current effectively detects a significant portion of electrical and electromagnetic faults in asynchronous motors. This monitoring technique, widely known as MCSA (Motor Current Signature Analysis), has been extensively discussed in several works [BON 22, YAT 23]. Induction machine faults diagnosis based on MCSA consists of faults characteristics extraction based on signal processing techniques followed by a fault detection procedure.

### I.6.2 Diagnosis by analysis of the stator current envelope

Different types of faults can indeed modulate the amplitude and/or frequency of the stator current signal. The Hilbert transform (TH) finds application in demodulating amplitude and/or frequency modulated signals. Specifically, by obtaining the modulus of the analytical signal through TH applied to the stator current, the envelope of the stator current is defined. Analyzing this envelope allows for the extraction of valuable information that can significantly improve the machine diagnosis.

### I.6.3 Diagnosis by analysis of the phase of the current spectrum

Traditionally, detecting faults in asynchronous machines relies on frequency analysis of indicative signals. Typically, this analysis involves taking the modulus of the current transformation absorbed by the machine. In an alternative approach, the authors in [DID 04] suggested utilizing the phase of the stator current spectrum. His work demonstrated that the information contained in this phase quantity is more relevant than its modulus, enabling deductions to be drawn about the presence of a rotor fault in the asynchronous machine.

### I.6.4 Diagnosis by Park vector analysis

Park vector analysis, also known as the "d-q transformation" is indeed a well-established technique used in the field of electrical engineering to analyze and diagnose faults in induction motors [SHA 13, IRF 19, NEJ 00,]. It is a mathematical transformation method that simplifies the representation of three-phase electrical quantities (currents and voltages) into a (d-q frame). By transforming the variables into this frame, certain fault signatures and patterns associated with different types of faults become more apparent and easier to identify.

### I.6.5 Diagnosis by instantaneous power analysis

The instantaneous power of a phase, obtained by multiplying the supply voltage with the absorbed stator current of the motor, carries more valuable information than just analyzing the current by itself. This approach has been utilized in several studies to detect faults in asynchronous motors [DRI 08, DRI 09, LIU 04]. By studying the patterns and characteristics of the instantaneous power under different operating conditions, it becomes possible to identify abnormalities and fault signatures, enabling timely fault detection and proactive maintenance. Ultimately, this contributes to improving the overall reliability and performance of asynchronous motors in various industrial applications.

### I.6.6 Diagnosis by analysis of induced stator voltages

This method relies on conducting a phase opening test while the machine operates without any load. By examining the frequency content of the voltages induced in the stator windings due to the rotor flux during the disconnection of the motor from the supply power, valuable information about the condition of the rotor cage can be obtained. One significant benefit of this approach is its immunity to disturbances like time harmonics and imbalances originating from the power source. However, a notable limitation of this technique is its inapplicability to machines that are integrated into a production system.

### I.6.7 Diagnosis through dispersion field analysis

The Diagnosis through dispersion field analysis is a diagnostic approach applied to rotating electrical machines. In these machines, the leakage flux originates from various components like the magnetic core, coil heads, and short-circuit ring. The external leakage field is divided into two components known as the axial external field, aligned with the axis machine, and the radial external field, perpendicular to the axis machine, reflecting the air gap induction.

Researchers have emphasized the analysis of the axial leakage flux in the machine to detect stator and rotor faults [AHM 08, ROM 13, SHA 20]. In fact, the presence of any fault leads to the electrical imbalance, affecting the magnetic field distribution both inside and outside the machine. Consequently, the dispersion field provides information about the presence of a fault. This method allows the detection of stator and rotor faults using a reasonable flux sensor. However, a disadvantage of this technique lies in the sensor connection.

To summarize, this approach involves analyzing the leakage flux in rotating electrical machines to detect stator and rotor faults. It relies on information from both the axial and radial fields and utilizes a cost-effective flux sensor for fault detection.

### I.6.8 Diagnosis by electromagnetic torque analysis

The electromagnetic torque produced in electrical machines results from the interaction between the stator and rotor fields. As a consequence, any fault, whether in the stator or rotor, directly impacts the electromagnetic torque. Analyzing the spectral content of the torque signal provides valuable insights into the health machine status. However, a significant limitation of this method is the requirement for costly equipment to acquire this information [BOG 12, KON 14, YAN 23]. To address this challenge, an alternative approach involves estimating the electromagnetic torque from the measured voltages and currents of the machine. Nevertheless, this solution faces difficulties due to variations in parameters, which restricts its applicability and accuracy.

### I.6.9 Diagnosis by vibration analysis

Vibration analysis is a non-destructive testing technique used to analyze the state of the induction motor in the industrial installations in order to carry out maintenance preventive conditional monitoring. Extensive research has been conducted on the vibrations of asynchronous machines [MOH 21, ALT 22, MUH 22]. This approach has proven effective in detecting various well-known defects, such as air gap irregularities, stator winding issues, imbalance problems, bearing fault and more.

## I.7 Diagnosis through the use of artificial intelligence tools

Data-driven intelligent fault diagnosis methods typically consist of two main steps: feature extraction and fault recognition. In the first step, advanced signal processing techniques are used to extract relevant information from the data, which is crucial for reducing input dimensionality and eliminating random noise [CHE 20]. This involves employing spectral analysis and time-frequency analysis to derive meaningful health indicators [LI 18, SON18]. The second step, fault recognition, involves the use of traditional classification techniques like Artificial Neural Networks (ANNs), Support Vector Machines (SVMs), and k-NN. These methods are popular due to their fast implementation and good classification performance [GRY 12, AFR 22, DRE 22, ZHA 22]. However, their shallow architectures pose a limitation as they struggle to effectively learn discriminative features from raw high-dimensional inputs. The diagnosis performance heavily relies on the expertise of the diagnosticians and the quality of the diagnostic features extracted.

Recently, there has been a surge of interest in utilizing Deep Learning (DL)-based approaches for intelligent fault diagnosis. DL models are designed with multiple non-linear processing layers, creating hierarchical architectures that excel at learning representations from raw or preprocessed mechanical data. These data types encompass time series series [SUN 18, HUA 18, CAN 19], spectra [YAN 19, MIS 22], and time frequency maps [ZHA 20, YE 21, JIA 23]. The adoption of DL techniques in fault diagnosis has shown promising potential for effectively analyzing and interpreting various types of faults, leading to improved diagnostic capabilities. A wide range of deep network architectures and their variants have been utilized to address various diagnosis tasks. These architectures include Auto Encoders (AE) [ZHE 22, YAN 22], Deep Belief Networks (DBN) [HUI 22, ZHA 22], Long Short-Term Memory (LSTM) networks [EGA 17, BAI 20], and Convolutional Neural Networks (CNN) [HAN 20, LIA 20]. By employing these DL approaches, researchers aim to enhance the accuracy and efficiency of fault diagnosis in diverse applications.

## I.8 Conclusion

In this chapter, we began by providing a non-exhaustive description of the construction of the squirrel-cage asynchronous machine, followed by an introduction to the various types of faults that may impact it. To address the diversity of methods employing different signals, we also presented an overview of the most commonly used signals for diagnosing faults in asynchronous motors. We delved into their strengths and limitations to gain a better understanding of their applicability in various scenarios. This exploration enabled us to grasp the challenges and possibilities related to fault diagnosis, opening up avenues for future advancements in this field.

Chapter 2

# Advanced signal processing methods dedicated to the diagnosis of asynchronous machine

## II.1 Introduction

Over the past two decades, there has been a notable industrial focus on fault diagnosis and protection of induction machines. The primary aim has been to enhance reliability and availability, ultimately optimizing the operational efficiency of systems employing electrical machines. Early fault diagnosis is of utmost significance in achieving these objectives. Induction machines can be categorized into two main types of faults: electrical failures and mechanical failures. As described in the previous chapter, the primary electrical faults can be categorized into stator failures and rotor failures, whereas mechanical faults encompass bearing failures, shaft misalignments, and static/dynamic air-gap eccentricities. To diagnose these faults, a range of methods is utilized, which includes measurement techniques like coils wound around motors (axial flux or stray flux), vibration analysis, acoustic analysis, and motor current signature analysis (MCSA). Numerous studies have been conducted to characterize faults by analyzing various signals. Concerning electrical faults, it has been observed that fault conditions lead to alterations in the stator and/or rotor magnetomotive force fields, resulting in the emergence of new frequency components in stator and/or rotor current signatures. For mechanical fault analysis, nonlinearity in air-gap permeance, load torque oscillations due to load unbalance, and bearing vibrations introduce magnitude or phase modulations into the stator current signal. Hence, to explore different fault phenomena, several signal processing methods can be utilized, which generally fall into two main categories: stationary techniques and non-stationary techniques. In the following sections, we will introduce and discuss the most commonly employed methods for diagnosing faults in rotating machines.

## II.2 Stationary techniques

The techniques described here can be divided into two main classes: non-parametric techniques, which include the periodogram and its extensions, and high-resolution techniques.

### II.2.1 Periodogram and its extensions

The periodogram is a method of estimating the power spectral density (PSD) of a random process x(n), which is defined as follow [ELB 17]:

$$P_x(f) = \frac{1}{N}\left|\sum_{N+0}^{N-1} x(n) e^{\frac{-j\,2\pi fn}{F_s}}\right|^2 \qquad \text{(II.1)}$$

The periodogram is commonly computed using the Fast Fourier Transform (FFT) algorithm due to its efficiency in calculating the Discrete Fourier Transform (DFT) quickly.

When rectangular windows are used, unwanted ripples appear in the signal spectrum. To address this issue, it is usual to employ weighting windows, which help improve the visualization of the spectrum components. As a result, expression (1) becomes [DID 04]:

$$P_{xw}(f) = \frac{1}{N}\left|\sum_{N+0}^{N-1} w(n)x(n)e^{\frac{-j\,2\pi fn}{F_s}}\right|^2 \qquad \text{(II.2)}$$

The term w(n) incorporated into the equation represents the mathematical representation of the selected weighting window. Among the well-known weighting windows are the Hanning window, the Hamming window, and the Blackman window. Each of these windows allows the user to control the desired trade-off between the width of the main lobe and the attenuation of the height of the largest secondary lobe in the frequency spectrum. This enables customization of the window characteristics based on specific requirements.

It is important to highlight that the periodogram suffers from bias (the average of the estimates deviates from the true parameter being estimated) and inconsistency (the variance does not converge to zero as the data record length approaches infinity) when used as an estimator for the power spectral density. This is performed using Welch periodogram; The Welch periodogram is obtained through a specific procedure. First, the signal is divided into overlapping segments. For each segment, the periodogram is computed and multiplied by a corresponding time-window. Afterward, the resulting periodograms are averaged together. This averaging process defines the Welch periodogram. Therefore, the Welch periodogram is given by:

$$P_w(f) = \frac{1}{L}\sum_{k=1}^{L} P_{xw}{}^{k}(f) \qquad \text{(II.3)}$$

where $P_{xw}(f)$ represents the periodogram of the windowed signal $w(n)x(n)$ .

The introduction of overlapping segments leads to an increase in the number of segments used for computation. This, in turn, results in a reduction of the estimator's variance and enhances the frequency resolution. Figures II.1 (a) and II.1 (b) provide a visual representation of the stator current periodogram and the Welch periodogram, respectively. To compute the periodogram, a signal length of 10 s and a sampling frequency of 10 kHz were used, along with the Hamming window.

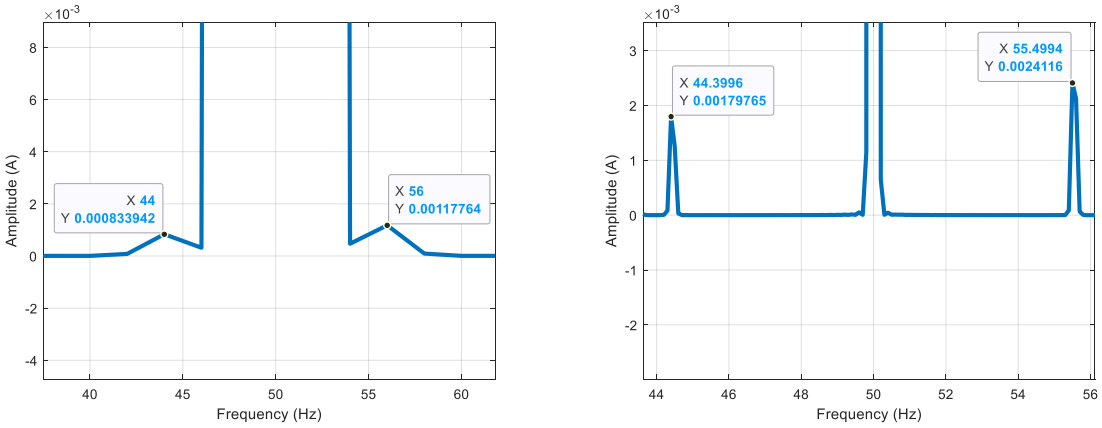


(a) Periodogram. (b) Welch periodogram.

**Fig. II.1** Stator current. PSD 1 with broken bar fault.

Employing the Welch method, the data was divided into overlapping segments, each with a 60% overlap. Modified periodograms of these overlapping segments were computed and then averaged to derive the Power Spectral Density (PSD) estimate. It is important to note that each segment was windowed using a Hamming window of the same length as the segment. The Welch periodogram significantly enhances the estimation performance, as illustrated in Figure II.1. It remarkably reduces the variance and improves the frequency resolution. The visual representation demonstrates how the Welch method effectively produces a more precise and reliable estimation of the signal spectrum content compared to periodogram method.

### II.2.2 High resolution techniques

High-Resolution (HR) methods indeed trace their origins to Prony work in 1795 and have been further developed by researchers like Kumaresan, Clergeot and Fuchs [Kum 84, CLE 89, FUC 96]. These methods employ linear prediction techniques to estimate a sum of exponentials.

Additionally, there is another group of HR methods known as "subspace methods" that leverage the properties of the covariance matrix signal. By determining the rank of this matrix, these methods can separate the data space into two distinct subspaces: the signal space, which contains sinusoidal components, and the noise space, which is orthogonal to the signal space [SAH 12].

#### II.2.2.1 Prony method

Prony's method enables the modeling of a sampled signal by combinations of damped complex exponentials. The complex representation of a modal signal containing F complex exponentials can be expressed as follows [LAA 17]:

$$x(n) = \sum_{k=1}^{F} h_k w_k^n \qquad n = 0, \ldots N-1 \tag{II.4}$$

$$h_k = A_k e^{j\phi_k} \tag{II.5}$$

$$w_k = e^{(-\alpha_k + j2\pi f_k)T_e} \tag{II.6}$$

The model parameters $A_k$, $f_k$, $\phi_k$, $\alpha_k$ represents respectively the amplitude, the frequency, the phase shift and the damping factor of the kth component.

The main challenge lies in accurately estimating the variables, as the system described by equation (II.4) is nonlinear and its solution poses considerable complexity. To overcome this challenge, the Prony method adopts a three-stage approach. This method comprises solving two linear systems and conducting a search for the roots of a polynomial. As a consequence of this process, the samples x(n) can be represented through the following recurrence equation [LAA 17]:

$$x(n) = -\sum_{k=1}^{F} a_k x(n-k) \qquad N \geq 2F \tag{II.7}$$

Initially, the first step consists in calculating the coefficients ak by solving the following linear system:

$$\mathbb{S}A = -X \tag{II.8}$$

Where

$$\mathbb{S} = \begin{bmatrix} x(F) & x(F-1) & \ldots & x(1) \\ x(F+1) & x(F) & \ldots & x(2) \\ \vdots & \vdots & \vdots & \vdots \\ x(2F-1) & x(2F-2) & \ldots & x(F) \end{bmatrix}; \quad A = \begin{bmatrix} a_1 \\ a_2 \\ \vdots \\ a_F \end{bmatrix}, \quad X = \begin{bmatrix} x(F+1) \\ x(F+2) \\ \vdots \\ x(2F) \end{bmatrix} \tag{II.9}$$

The parameters $a_k$ are determined by solving equation (II.8). Then a polynomial characteristic with roots $z_k$ can be formed using the parameters $a_k$ as follows:

$$P(z) = \sum_{i=0}^{F} a_i z^{F-i} = \prod_{k=1}^{F} (z - w_k), \qquad a_0 = 1, \tag{II.10}$$

Therefore, the damping coefficient and the frequency can be deduced directly from the roots $z_k$ of polynomial (II.10):

$$f_k = \frac{1}{2\pi\Delta T}\tan^{-1}\left[\frac{\mathrm{Im}(z_k)}{\mathrm{Re}(z_k)}\right] \quad et \quad \alpha_k = \frac{\ln|z_k|}{\Delta T} \tag{II.11}$$

Finally, the roots $z_k$ are used to write the F equations of (II.4) in a matrix form:

$$\begin{bmatrix} 1 & 1 & \dots & 1 \\ w_1 & w_2 & \dots & w_p \\ \vdots & \vdots & & \vdots \\ w_1^{F-1} & w_2^{F-1} & \dots & w_F^{F-1} \end{bmatrix} \begin{bmatrix} h_1 \\ h_2 \\ \vdots \\ h_F \end{bmatrix} = \begin{bmatrix} x(0) \\ x(1) \\ \vdots \\ x(F-1) \end{bmatrix} \tag{II.12}$$

The complex parameters $h_k$ can be determined by solving equation (II.12). Therefore, the amplitude and phase angle can be obtained using the following relationships:

$$A_k = |h_k| \quad \varphi_k = \tan^{-1}\left[\frac{\mathrm{Im}(h_k)}{\mathrm{Re}(h_k)}\right] \tag{II.13}$$

### II.2.2.2 Multiple signal classification (MUSIC) method

The Multiple signal Classification (MUSIC) algorithm is a popular subspace-based method for parameter signal estimation. It aims to estimate the frequencies present in a signal from the eigenvalues and associated Eigenvectors of the covariance matrix of measurement data. The signal subspace is assumed to represent the underlying structure of the discrete signal x[n] as a collection of complex sinusoids embedded in the noise b(n):

$$\begin{aligned} x(n) &= \sum_{i=1}^{p} s_i(n) + b(n) \\ &= \sum_{i=1}^{P} B_i e^{j\phi_i} e^{j2\pi f_i n} + b(n),\ n = 0,1,\dots,N-1 \end{aligned} \tag{II.14}$$

Where $B_i, f_i$ *and* $\phi_i$ are respectively the amplitude, frequency and phase of the ith complex sinusoid, b(n) is the white noise with the zero mean and a $\delta^2$ variance. (II.14) can be written in condensed form as:

$$X(n) = AY + \mathrm{B}(n) \tag{II.15}$$

With $Y = \left[\overline{A}_1 e^{j2\pi f_1 n} \quad \overline{A}_2 e^{j2\pi f_2 n} \quad \dots \quad \overline{A}_p e^{j2\pi f_p n}\right]^T$, $\overline{A}_i = a_i e^{j\phi_i}$

$A \in \mathbb{C}^{N\times P}$ is the Vandermonde matrix which is défined as :

$$A=\begin{bmatrix} f(f_1) & f(f_2) & \cdots & f(f_p) \end{bmatrix}=\begin{bmatrix} 1 & 1 & \cdots & \cdots & 1 \\ e^{j2\pi f_1} & e^{j2\pi f_2} & \cdots & \cdots & e^{j2\pi f_p} \\ e^{j4\pi f_1} & e^{j4\pi f_2} & \cdots & \cdots & e^{j4\pi f_p} \\ \vdots & \vdots & & & \vdots \\ e^{j2(N-1)\pi f_1} & e^{j2(N-1)\pi f_2} & \cdots & \cdots & e^{j2(N-1)\pi f_p} \end{bmatrix}$$

and $f(f_i)=\begin{bmatrix} 1 & e^{j2\pi f_i} & \cdots & e^{j2\pi(N-1)f_i} \end{bmatrix}^T$, $x(n)=\begin{bmatrix} x(n) \\ x(n+1) \\ \vdots \\ x(n+N-1) \end{bmatrix}$, $B(n)=\begin{bmatrix} b(n) \\ b(n+1) \\ \vdots \\ b(n+N-1) \end{bmatrix}$

The MUSIC approach relies on eigenvector decomposition of x[n] to derive two orthogonal subspaces. The autocorrelation matrix $R_X$ of the signal x[n] can be expressed as [ELB 17]:

$$R_X = E\left[X(n)X^H(n)\right] \tag{II.16}$$

The correlation matrix (II.16) can be seen as the sum of two matrices: the signal autocorrelation matrix $R_S$ and the noise autocorrelation matrix Rn. This relationship can be defined as follow:

$$R_X = R_s + R_n = V\Lambda V^H + \sigma^2 GG^H \tag{II.17}$$

where $\Lambda$ is a diagonal matrix that contains the p largest strictly positive eigenvalues $\sigma_p$ sorted in decreasing order. The matrix $V=\begin{bmatrix} v_1 v_2 \cdots v_p \end{bmatrix}$ defines the signal subspace, which contains the P eigenvectors associated with the main eigenvalues. While the noise subspace matrix $G=\begin{bmatrix} v_{p+1} \cdots v_N \end{bmatrix}$ encloses the (N-P) eigenvectors of $R_X$ associated with the remaining eigenvalues.

The sought P modes $\{f_i\}_{i=0,\ldots,P-1}$ are the unique solutions of the equation [SAH 12]:

$$\left\| G^H f(f_i) \right\|^2 = 0 \tag{II.18}$$

The main steps of the MUSIC algorithm are summarized follows:

1. Collect the signal samples: Obtain a sequence of data samples x[n] = [x[n], x[n + 1], ..., x[n + M − 1], where M is the number of data samples in a window.
2. Compute the covariance matrix Rx of the signal samples x[n]. The covariance matrix provides information about the correlation between different samples.

3. Eigenvalue decomposition: Perform eigenvalue Decomposition (EVD) of the covariance matrix Rx to obtain its eigenvalues ($\lambda_1 \geq \lambda_2 \geq ... \geq \lambda_N$) and corresponding Eigenvectors ($v_1$, $v_2$, ..., $v_N$).
4. Estimate the model order: Based on the eigenvalues, determine the number of significant eigenvalues (P) that correspond to the signal subspace. This step essentially helps to estimate the number of modes present in the data.
5. Construct the noise subspace G. Select the remaining eigenvectors (N-P) to form the noise subspace. These eigenvectors represent the noise-only components of the data.
6. Extract the roots of the equation (II.18).

However, in practice, the equation (II.18) is not strictly valid due to the presence of noise. As a result, R. O. Schmidt [SCH 86] proposed an enhancement to address this issue. The improvement involves identifying the P largest local maxima of the function below, effectively searching for the peaks of the Music pseudo-spectrum

$$P(f_i) = \frac{1}{\left\| G^H f(f_i) \right\|^2} \tag{II.19}$$

### II.2.2.3 Estimation of Signal Parameters via Rotational Invariance Techniques (ESPRIT)

Esprit is a method based on the signal subspace. It exploits the property of invariance by translation of the sub-signal space to estimate the parameters of the modes (frequencies, amplitudes, phases, etc.). As A and V cover the same signal subspace, then there is a linear transformation presented by the invertible matrix T of dimension PxP, defined as a transition matrix between the two bases, such as:

$$V = AT \tag{II.20}$$

When we partition the matrix A into two contiguous sub-matrices, each with N-1 rows, we establish the subsequent relationship: $A_2 = A_1\Phi$

with $A_1$ *et* $A_2$, the extracted matrices from A after excluding its final and initial rows, as illustrated below:

$$A = \begin{pmatrix} A_1 \\ - \end{pmatrix} = \begin{pmatrix} - \\ A_2 \end{pmatrix} \tag{II.21}$$

The matrix $\Phi$ can be seen as a rotation operator. It is a diagonal matrix of dimension $P \times P$ , defined by:

$$\Phi = \begin{bmatrix} e^{j2\pi f_1} & & & \\ & e^{j2\pi f_2} & & \\ & & \ddots & \\ & & & e^{j2\pi f_p} \end{bmatrix} \quad \text{(II.22)}$$

Similarly, we decompose the matrix V into two adjacent blocks $V_1$ *et* $V_2$ :

$$V = \begin{pmatrix} V_1 \\ - \end{pmatrix} = \begin{pmatrix} - \\ V_2 \end{pmatrix} \quad \text{(II.23)}$$

By the use of (II.17) , it is possible to demonstrate

$$R_Y V = V\Lambda \rightarrow AR_X A^H V + \sigma^2 V = V\Lambda \quad \text{(II.24)}$$

from (II.24), we obtained :

$$V = AC \quad \text{(II.25)}$$

with $C = R_X A^H V(\Lambda - \sigma^2 I)^{-1}$ .

According to (II.21) and (II.23), we have $V_2 = A_2 C$ *et* $V_1 = A_1 C$ , consequently:

$$V_2 = V_1 \Psi \quad \text{(II.26)}$$

with

$$\Psi = C^{-1} \Phi C \quad \text{(II.27)}$$

The quation (39) shows that $\Phi$ *et* $\Psi$ are similar, and therefore they have the same eigenvalues.

The process of finding the rotation matrix $\Phi$ is equivalent to finding the eigenvalues of the matrix $\Psi$ , which is obtained by solving the following system:

$$V_2 = V_1 \Psi \quad \text{(II.28)}$$

ESPRIT is a method based on the signal subspace. It is used to estimate the parameters of the modes (of a signal. ESPRIT exploits the invariance property by translation of the sub-signal space to achieve this estimation.

The ESPRIT method can be summarized as follow [SAH 12]:

1. Select $N \geq P$
2. Compute the covariance matrix Rx of the signal samples x[n].
3. Calculate the eigenvalues of the autocorrelation matrix.

4. Estimate the model order
5. Form the signal subspace composed $V = [v_1 \quad \dots \quad v_P]$ by eigenvectors corresponding to the P largest eigenvalues.
6. Estimate the matrix $\Psi$, by resolving the system equations $V_2 = V_1 \Psi$
7. Search for the eigenvalues $\left\{e^{j2\pi f_1}, \dots, e^{j2\pi f_p}\right\}$ of $\Psi$.
8. Finally, the estimated frequencies $\left(f_i \ pour 1 \le i \le p\right)$ can be calculated by $f_i = \frac{\angle(\Psi_i)}{2\pi}$.

In practice, these two last high resolution techniques outperform parametric methods, particularly when dealing with low signal-to-noise ratio (SNR) signals. However, it is worth noting that the computation time for this method is a more critical factor compared to alternative methods. In addition, these approaches calculate the frequency components of a signal but doesn't give information about their amplitudes [ELB 21]. Hence, to address this limitation, an additional technique is employed, which relies on the total least squares (TLS) method. Figure II.(a) and (b) give the stator current spectrum, for healthy and one broken rotor bar (BRB) cases, using root-music and esprit methods.

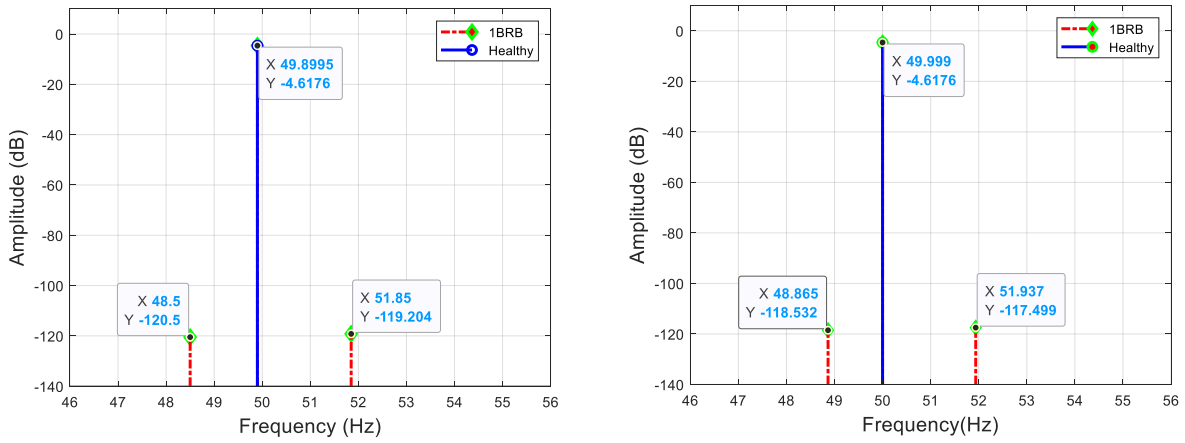


(a) Root-Music method (b) Esprit method

**Fig. II.2** Stator current spectrum using subspace techniques.

## II.3 Non stationary techniques

### II.3.1. Time-Frequency, Time-Scale methods

Spectral estimation methods mentioned previously are not well-suited for monitoring in nonstationary environments because they struggle to handle transient or faulty operational conditions effectively. In situations involving nonstationary conditions, the detection of faults

under disturbances is commonly carried out using representations that combine time-frequency and time-scale information. These methods encompass, but are not restricted to, techniques such as the Short-Time Fourier Transform (STFT), Continuous Wavelet Transform (CWT), Wigner–Ville Distribution (WVD), the Hilbert–Huang Transform (HHT), vibrational mode decomposition (VMD).

### II.3.1.1 Spectrogram

The spectrogram is generated through the utilization of the Short Time Fourier Transform (STFT). The STFT involves breaking down the temporal signal into segments and applying a Fourier transformation (FT) to each segment [LIN 20]. This process helps identify the sine frequency and phase characteristics of localized portions within a measurement signal as it progresses chronologically. In fact, the signal undergoes analysis within a temporal window denoted as 'h(n)', where it is assumed to exhibit stationary behavior. The window's length is chosen in such a way as to validate the stationarity assumption. This selection has a direct impact on the resolution of the decomposition. In fact, a short temporal window leads the increase of the temporal resolution but the frequency resolution decreases, and conversely. Therefore, if a higher frequency resolution is required, a larger analysis window must be employed, potentially challenging the stationarity assumption. Classical time window such as the rectangular, Hanning, Hamming or Gaussian windows analyze the signal over a fixed period. This resolution remains constant across the time–frequency domain, indicating that the Short-Time Fourier Transform (STFT) operates as a single-resolution method (Fig. II.3).

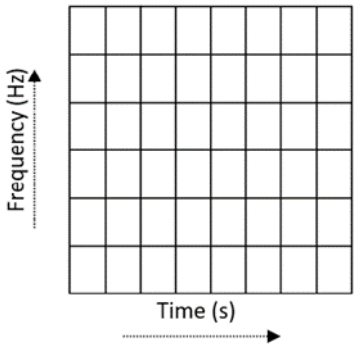


**Fig. II.3** Time-frequency representation space

The window's shape and length are parameters that need to be defined at the outset of the analysis. This assumes a thorough prior understanding of the signal to be analyzed. Consider discrete signals x(n) characterized by a period of N, as well as a time window denoted as h[n], the formula employed for calculating the STFT is given by [ELB 21]:

$$S_x(m,l) = \sum_{N+0}^{N-l} x(n)h(n-m)e^{-\frac{j2\pi ln}{N}} \quad \text{(II.29)}$$

For each $0 \leq m \leq N$, $S_x(m, l)$ is calculated for $0 \leq l \leq N$ with N fast Fourier transform (FFT) procedures of size N.

The spectrogram is employed for examining the frequency characteristics and fluctuations within a non-stationary signal. The spectrogram of the stator current in healthy case with two BRBs faults is given in Figure II.4.a and b. It can be clearly see the existence of the magnitude ripple of the fundamental frequency in the case of the broken bars defect compared to the healthy state. This indicates the stator current amplitude modulation induced by BRB fault.

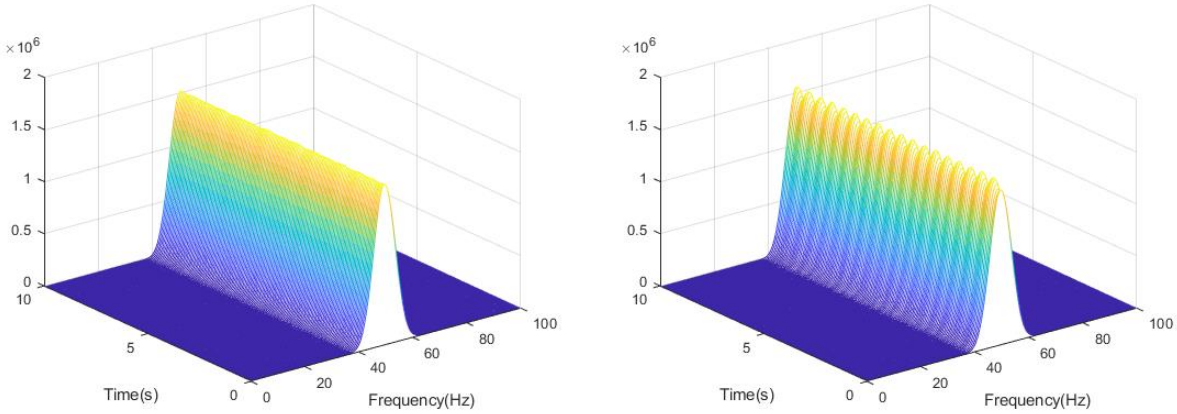


(a) Healthy state (b) Faulty state

**Fig. II.4** The Spectrogram for healthy rotor and rotor with 1BRB

### II.3.1.2 The scalogram

The scalogram relies on computing the Discrete Wavelet Transform (DWT). The DWT involves decomposing the signal into shifted and scaled iterations of a mother wavelet. The analysis is conducted using a function Ψ known as the fundamental wavelet (or mother wavelet), which allows for the determination of desired signal attributes for detection. In order to analyze transient components of varying durations, the wavelet transform decomposes signals using a set of translated and scaled wavelets. The width of the window is thus adjusted for each individual spectral component, leading to a time-frequency resolution distinct from that of the Short-Time Fourier Transform (STFT). In other words, wavelet analysis consists of comparing the signal to be analyzed with a family of functions $\psi_{a,b}$. from the same function, the mother wavelet $\psi$, by the action of two operators [KIA 07]: The temporal translation operator enables the selection of the

moment for analysis and the scale dilation operator subjects the function ψ to a scale change by a factor of 'a'. This is equivalent to performing a dilation on the graph of ψ(t), which involves scaling by the parameter 'a' along both the time axis and the amplitude axis. The analysis functions are thus expressed as follows [KHA 12]:

$$\psi_{a,b}(t) = \frac{1}{\sqrt{a}}\psi\left(\frac{t-b}{a}\right), \quad (a,b) \in \mathbb{R} \tag{II.30}$$

The wavelet transform of $x \in L^2(\Re)$ at time $t$ and scale $a$ is computed by projecting $x(t)$ onto the wavelet family $\psi_{a,b}(t)$; $t \in \Re$ and $a,b \in \Re^+$. The resulting time-scale representation is known as the continuous wavelet transform (CWT), and its definition is as follows:

$$T_x(a,b) = \frac{1}{\sqrt{|a|}}\int_{-\infty}^{\infty} x(t)\psi^*\left(\frac{t-b}{a}\right)dt \tag{II.31}$$

Its frequency-domain version is given by:

$$T_x(a,b) = \int_{-\infty}^{\infty} X(t)\psi^*(af)e^{j2\pi fb}df \tag{II.32}$$

Where ψ(t) represents the mother wavelet, a and b is the translation and the scale parameters respectively.

ψ(t) needs to be localized both in time and in frequency. To achieve this, it must satisfy certain admissibility conditions [MAL 99]:

1. $\int |\Psi(f)|^2 \frac{df}{|f|} = c_\Psi < \infty$ (II.33)

2. $\int \Psi(t)dt = 0$ (II.34)

The wavelet can be interpreted as a band-pass filter with a central frequency fc. The values of the coefficients are higher when the frequency of the analyzed signal aligns with that of the wavelet. The variation of the parameter 'a' makes it possible to determine the band around the frequency, where represents the width of the band of the wavelets.

The wavelet transform offers the capability to examine varying frequencies at distinct resolutions. It achieves high temporal resolution for high frequencies and sharp frequency resolution for low frequencies. The Discrete Wavelet Transform (DWT) operates as a multi-resolution method, guiding the input signal through a sequence of high-pass filters (details denoted by H) for high-frequency analysis, and a series of low-pass filters (approximations represented by L) for low-

frequency analysis.This DWT approach delivers superior temporal resolution for high frequencies and enhanced frequency resolution for low frequencies. This approach is utilized to study the stator current envelope for broken bar fault detection, the obtained scalogram is shown in figure II.6.

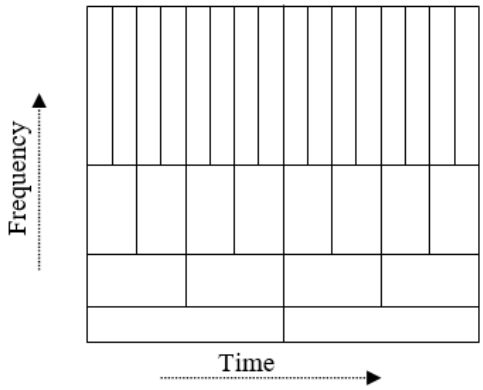


**Fig. II.5** The wavelet transform tiling.

## A. Discrete wavelet transform (DWT)

To apply the wavelet transform on digital signals, a discretization of the resolution parameter and the position parameter is necessary [KHA 12]. This discretization of the time-frequency plane involves constructing a non-uniform grid defined by the parameters of the equation (II.35):

$$(b,a)=(kb_0a_0^j,a_0^j),\ avec\ b_0>0,\ a_0>1,\ \ j\in\mathbb{Z} \tag{II.35}$$

An atom of this discrete transform is defined as outlined in equation (II.35).

$$\psi_{m,n}(t)=\frac{1}{\sqrt{{a_0}^m}}\psi\left(\frac{t-nb_0a_0^m}{a_0^m}\right) \tag{II.36}$$

Finally, (II.26) give the DWT of the signal of the discreet signal as follow:

$$T_x(m,n)=\frac{1}{\sqrt{{a_0}^m}}\int x(t)\psi\left(\frac{t-nb_0a_0^m}{a_0^m}\right) \tag{II.37}$$

DWT is only possible if the wavelets are orthogonal. Orthogonality in this context means that the wavelet functions are perpendicular to each other and they form an orthogonal basis. This means that each signal can be decomposed into a linear combination of these orthogonal wavelet functions, allowing efficient decomposition of signals into different frequency scales or levels of detail while avoiding interference or overlap between the components of the decomposition. Multi-

resolution analysis is a methodology employed in signal processing and data analysis, designed to investigate a signal across various levels of detail. The primary objective of this technique is to gain a more intricate and comprehensive insight into the signal by scrutinizing its constituent elements across distinct frequency bands or resolutions. In the formalization of multi-resolution analysis, there exist two options for discretization. The initial choice involves a continuous decomposition, with $a_0$ is very close to 1 and $b_0$ is sufficiently small. In this case, an examination of frequencies becomes imperative based on the coefficients of dilation, as dictated by a power evolution of j. The second option ($a_0$ =2, $b_0$ =1) corresponds a dyadic sampling of the time-frequency plane. The set of points is termed the dyadic grid, as depicted in figure (II.7). An atom unit of this discrete transformation is consequently defined as [MAL 99]:

$$\psi_{j,k}(t) = \frac{1}{\sqrt{2^j}} \psi\left(\frac{t - 2^j k}{2^j}\right) \qquad \text{(II.38)}$$

The discrete wavelet transform of x(t), computed from $\psi_{j,k}(t)$ is given by the following formulation:

$$T_{dx}(j,k) = \int x(u)\psi^*_{j,k}(u)du \qquad \text{(II.39)}$$

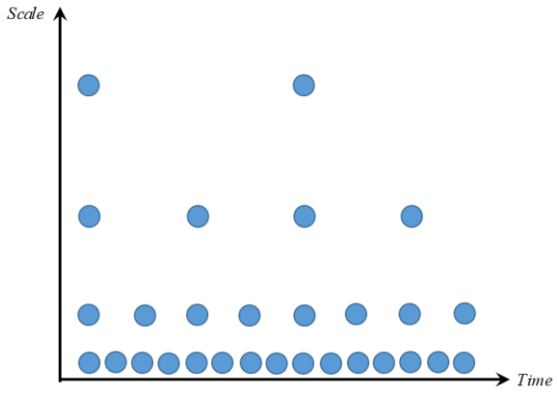


**Fig. II.7** Dyadic grid

One of the reasons for the success of the wavelet transform is its efficient hardware implementation. The prevailing approach for executing a wavelet transform centers around the utilization of filter banks structured in a pyramid configuration, a methodology pioneered by [Mal 99]. At each level, two Finite Impulse Response (FIR) filters compute the wavelet coefficients (details) and scale coefficients (approximations), they then have respectively high-pass and low-pass characteristics. To keep the same number of output and input samples, the convolution products from the filters are undersampled by a factor of two. Subsequently, solely the output

stemming from the low-pass filter referred as the approximation is subjected once more to processing via the two filters. The process for two levels of decomposition is shown in figure (II.6), where G and H denote the discrete high-pass and low-pass filters, and the symbol $\downarrow 2$ signifies a decimation by a factor of 2, implying that every alternate coefficient is retained. This leads to the formation of a cascading algorithm, facilitating the derivation of all resolution levels lower than the initial one through iterative steps. Consequently, for the nth level of decomposition, the corresponding approximation and detail coefficients are denoted as $A_n$ and $B_n$, with a frequency band respectively $\left[0, f_e/2^{n+1}\right]$ and $\left[f_e/2^{n+1}, f_e/2^n\right]$ [BEN 07].

The approximation and detail signals give the temporal evolution of the frequency components inherent in the original signal, each encompassing distinct frequency bands. However, due to the non-ideal nature of the filtering process, there is a tendency for some overlap to occur between neighboring frequency bands. The impact of this phenomenon can result in distortion depending on how the Time-Frequency representation is utilized. This is especially pertinent when specific frequency components of a signal reside near the border of a frequency band. Employing wavelet functions equipped with higher-order filters can serve as a remedy, as they have the capability to mitigate this issue by narrowing the width of the overlapping region between adjacent bands.

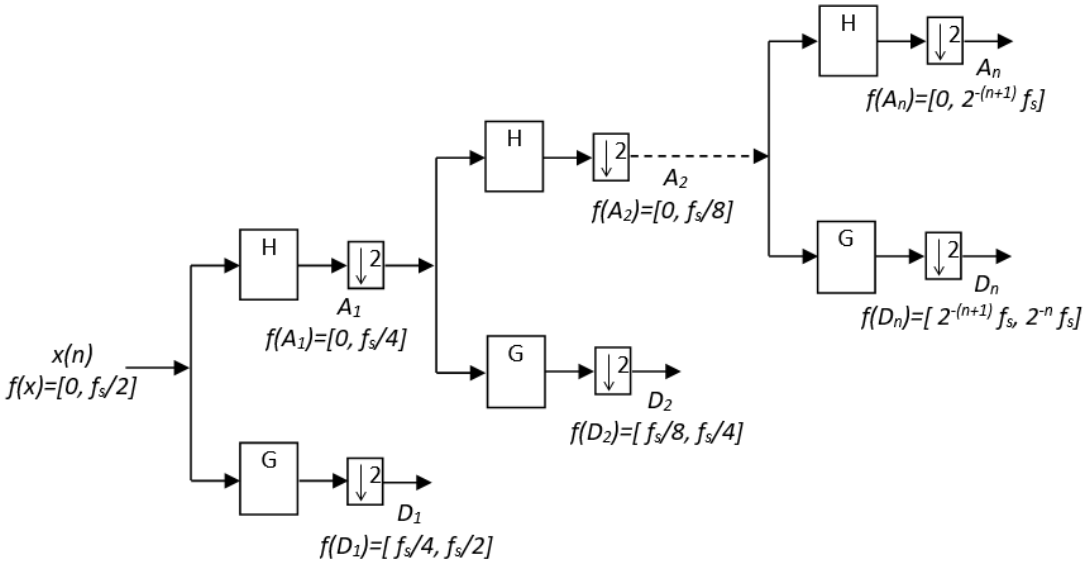


**Fig. II.8** Principle of the decomposition by the DWT at level n

In the context of multi-resolution analysis, it is imperative to predefine both the mother wavelet and the number of levels to be employed. The decision regarding the number of levels is guided by a relationship that links the sampling frequency with the low frequency components to be extracted such as [KHA 12]:

$$l > \frac{\log(f_s / f_b)}{\log(2)} - 1 \qquad \text{(II.40)}$$

with $f_s, f_b$ are respectively the sampling frequency and the low frequency component (default component).

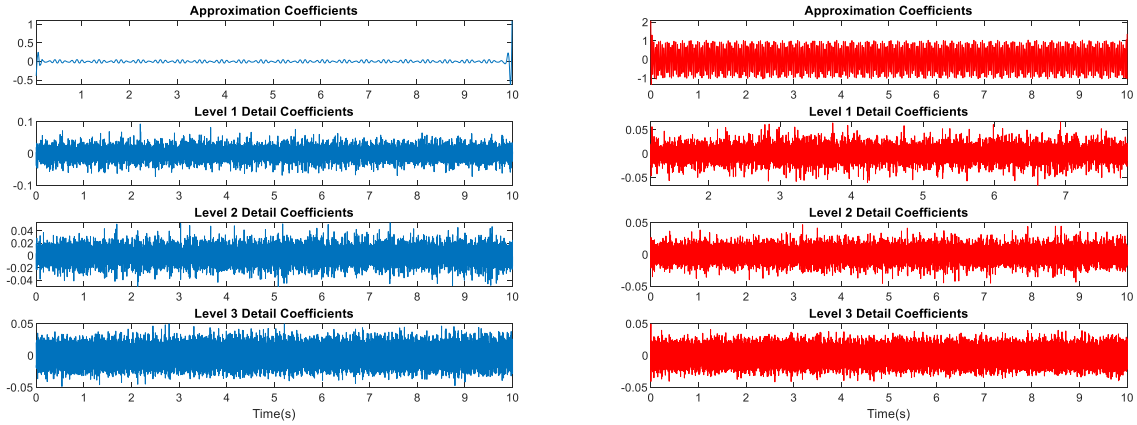


(a) (b)

**Fig. II.9** DWT of stator current (a) healthy rotor (b) rotor with 1BRB

Figure II.9 depicts the time-domain signals of both the approximation and the first three details, for the healthy state and 1BRB fault condition. These signals are acquired through the processing of the stator current using the Discrete Wavelet Transform (DWT).

## B. Packet wavelet transform (PWT)

The Packet Wavelet Transform (PWT) is an advanced version of the Discrete Wavelet Transform (DWT) that offers enhanced flexibility in signal decomposition. Unlike the DWT, which predominantly involves decomposing a signal into approximation and detail coefficients at different scales, the PWT takes the process further. In PWT, both the approximation and detail coefficients are subjected to additional rounds of decomposition. This multi-level decomposition provides a more comprehensive insight by considering various sub-components of the signal. As a result, the PWT offers a higher level of granularity in signal analysis compared to the DWT.

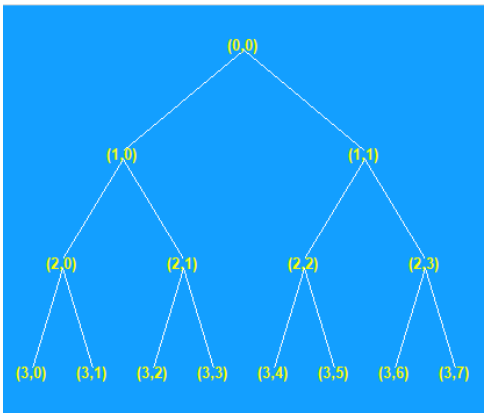


**Fig. II.10** The binary tree of decomposition into dyadic wavelet packets

Figure II. 10illustrates the extended pyramid algorithm used to acquire the coefficients. This decomposition tree can be visualized as an array of coefficients, where the each row cells undergo decomposition into two subtrees that correspond to orthogonal subspaces.

### II.3.1.3 Hilbert Huang transform (HHT)

Hilbert-Huang Transform (HHT) stands as a specialized adaptive technique designed for the analysis of nonlinear and nonstationary signals. At its heart lies the Empirical Mode Decomposition (EMD) method, which facilitates the partitioning of intricate datasets into a defined and often constrained set of elements termed intrinsic mode functions (IMFs). HHT encompasses the process of dynamically decomposing a signal into a summation of mono-component signals, each characterized by modulation in magnitude and/or frequency, holding a distinct frequency value for every sample. This procedure further involves the computation of instantaneous frequency and magnitude for each of these components through the utilization of the Hilbert transform (HT). The HHT method is composed of main steps:

1. The intrinsic mode functions (IMFs) are derived from the target signal through the application of the Empirical Mode Decomposition (EMD) algorithm.
2. Following this, the Hilbert transform (HT) is executed on these IMFs, as demodulation technique. This process encompasses both the estimation of instantaneous frequency and amplitude.

#### A. Empirical mode decomposition

Empirical mode decomposition (EMD) is adaptable computational approach, empowers the decomposition of a signal into an assembly of oscillatory constituents [LOU 05]. Employing a sieving process called sifting, this technique disentangles a signal into basic functions known as

Intrinsic Mode Functions (IMFs), characterized by amplitude and/or frequency modulation (AM-FM) (LOU 04). The EMD algorithm meticulously accounts for localized signal oscillations, facilitating the partitioning of data into distinct time-scale elements. This decomposition technique adheres to two fundamental properties [AHM 22].

- An IMF is defined by the presence of a solitary extremum located between two successive zero crossings.
- An IMF exhibits an average value of zero.

Applying the criteria outlined earlier, the signal y(t) can be separated into IMFs denoted as $U_n(t)$, along with a residual component r(t). This decomposition offers a representation of the signal in the following form [AHM 22]:

$$y(t) = \sum_n u_n(t) + r(t) \tag{II.41}$$

The procedure can be outlined through the subsequent steps as elucidated in reference [ELB 17].

Step1 Initialize: n = 1, $r_0(t) = y(t)$

Step2 Extract the nth IMF as follows:

1. Set $h_0(t) = r_{i-1}(t) and\ i = 1$
2. Identify all the local extrema of $h_{i-1}(t)$.
3. Connect between Maxima (resp. minima) by a cubic spline line as the upper envelope $U_{i-1}(t)$ (resp lower envelope $L_{i-1}(t)$ ).
4. Calculating the average value $m_{i-1}(t) = \frac{U_{i-1}(t) - L_{i-1}(t)}{2}$
5. Acquired $h_i(t) = h_{i-1}(t) - m_{i-1}(t)$
6. If $h_i(t)$ satisfies the IMF criteria then set $u_n(t)=h_i(t)$ and $r_i(t) = r_{i-1}(t) - x_n(t)$, otherwise increase i=i+1, and return to stage(2)

Step 3: If $r_n(t)$ represents a residue, stop the sifting process; if not, increase n → n + 1 and start at step 1 again.

The intrinsic mode function (IMF) represents a component distinguished by modulation in both magnitude and frequency, taking on the resemblance of a narrowband signal. The extraction of IMFs employs non-linear techniques, whereas their reassembly for precise signal reconstruction adopts a linear approach. EMD's efficacy as a flexible and adaptable analytical tool for non-stationary signals has been demonstrated [KAR 11]. It possesses the capability to faithfully capture

the instantaneous frequency characteristics of a signal. Figure II 9 show the results of applying Empirical Mode Decomposition (EMD) to the stator current, considering both the healthy state and faulty state with two BRB faults. This process yields the extraction of several Intrinsic Mode Functions (IMFs) for each signal.

## B. Calculation of Instantaneous Amplitude and Frequency

The extraction of the instantaneous frequency (IF) and instantaneous amplitude (IA) of each IMF can be achieved through the application of the demodulation techniques. An established and effective method for this purpose is the application of the Hilbert transform. When the Hilbert transform is utilized in combination with EMD, this fusion is denoted as the Hilbert-Huang Transform (HHT). The utilization of the Hilbert transform (HT) serves to compute the analytical signal, characterized by the absence of negative-frequency components. In the case of a discrete signal x[n], the discrete version of the Hilbert transform is defined by [AMI 20]:

$$HT\left(x\left(t\right)\right)=y\left(t\right)=\frac{1}{\pi}\int_{-\infty}^{+\infty}\frac{x\left(\tau\right)}{\left(t-\tau\right)}d\tau \tag{II.42}$$

The analytical signal Z(t) associated with x(t) can be expressed as:

$$Z\left(t\right)=x\left(t\right)+jy\left(t\right)=a(t)e^{j\theta(t)} \tag{II.43}$$

Once the analytical signal is computed, the IA and IF are given by:

$$a(t)=\sqrt{x^{2}(t)+y^{2}(t)} \tag{II.44}$$

$$\theta(t)=\arctan\left(\frac{y\left(t\right)}{x\left(t\right)}\right),\ and\ \ f\left(t\right)=\frac{d\theta(t)}{2\pi}F_{s}, \tag{II.45}$$

Ultimately, the depiction in the time-frequency domain is achieved by presenting the progression of IA and IF for each IMF on the time-frequency plane.

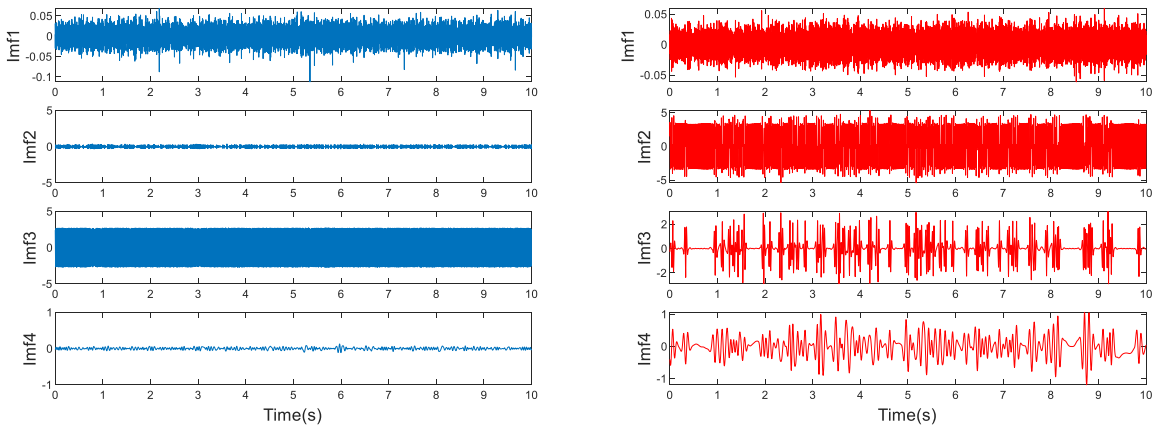

(a) (b)

**Fig. II.11** IMFs computed using empirical mode decomposition. (a) Healthy rotor (b) rotor with 1BRB

### II.3.1.4 Variational mode decomposition

Dragomiretskiy and Zosso introduced in [DRA 13] a novel time-frequency signal processing method known as variational mode decomposition (VMD), which is a quasi-orthogonal technique. VMD dissects the input signal into a set of sub-signals known as intrinsic mode functions (IMFs) using a constrained variational problem. In this approach, each IMF is treated as an amplitude-modulated and frequency-modulated (AM-FM) signal with a specific center frequency (wk) and limited bandwidth. The formulation of the constrained variational problem is as follows [DRA 13]:

$$\min_{\{u_k\}\{\omega_k\}} \left\{ \sum_{k=1}^{K} \left\| \partial_t \left[ \left( \delta(t) + \frac{j}{\pi t} \right) * u_k(t) \right] e^{-j\omega_k t} \right\|_2^2 \right\} \quad \text{(II.46)}$$

$$\text{s.t} \qquad \sum_{k=1}^{K} u_k(t) = f(t)$$

In order to address the constrained variational problem, the approach involves the introduction of an augmented Lagrangian, and from this, the unconstrained variational problem is derived as:

$$L\left(\{u_i\},\{\omega_i\},\lambda\right) = \alpha \left\{ \sum_{k=1}^{K} \left\| \partial_t \left[ \left( \delta(t) + \frac{j}{\pi t} \right) * u_i(t) \right] e^{-j\omega_k t} \right\|_2^2 \right\} + \left\| f(t) - \sum_{k=1}^{K} u_i(t) \right\|_2^2 + \left\langle \lambda(t), f(t) - \sum_{k=1}^{K} u_i(t) \right\rangle \quad \text{II.47}$$

Where α represents the balancing parameter for the data-fidelity constraint, and λ (t) signifies the Lagrange multipliers.

The iterative expressions for uk and ωk are derived using the approach of the alternate direction method of multipliers in the following manner:

$$u_k^{n+1}(\omega) = \frac{f(\omega) - \sum_{i<k} u_k^{n+1}(\omega) - \sum_{i>k} u_k^{n}(\omega) + \frac{\lambda^n(\omega)}{2}}{1 + 2\alpha(\omega - \omega_k^n)^2}$$

$$\omega_k^{n+1} = \frac{\int_0^{\infty} \omega \left| u_k^{n+1}(\omega) \right|^2 d\omega}{\int_0^{\infty} \left| u_k^{n+1}(\omega) \right|^2 d\omega} \quad \text{(II.49)}$$

The main procedures of VMD can be summarized as follows:

Step 1: Initialize $u_k^1, \omega_k^1, \lambda_k$ and maximum iterative time N;

Step 2: Update $u_k$ $\omega_k$ according (II.48) and (II.49)

Step 3: Update $\lambda$ based on

$$\lambda^{n+1}(\omega) = \lambda^n(\omega) + \tau\left(f(\omega) - \sum_k u^{n+1}(\omega)\right)$$

Step 3 : If $\sum \frac{\left\|u_k^{n+1} - u_k^n\right\|_2^2}{\|\ \ \|^2} < \varepsilon$ stop iterating otherwise return to step 2.

## II.4 Conclusion

This chapter introduces both traditional and contemporary signal processing approaches. Its primary objective is to demonstrate how these methods can enhance fundamental diagnostic techniques and foster the creation of innovative ones. These methods, based on their utilization, are categorized in frequency, time, and time-frequency domains. They hold relevance across diverse induction machine signals operating under varied conditions. In fact, selecting appropriate signal processing methods for fault detection in different operating conditions of induction machines is crucial. Particularly, in situations involving transients or variations in speed and load, the acquisition of short data is required. The most effective diagnostic outcomes emerge when the chosen method aligns well with the characteristics of the observed phenomena.

Chapter 3

# Machine Learning and Deep learning

## III.1 Introduction

In contemporary times, artificial intelligence (AI) powered intelligent systems heavily rely on machine learning techniques. Machine learning entails the ability of systems to learn from specialized training data, enabling them to automate the construction of analytical models and address related tasks. Deep learning, a subfield of machine learning, revolves around the utilization of artificial neural networks as illustrated in Fig.III.1. Deep learning models often surpass the performance of shallow machine learning models and conventional data analysis methods, making them highly sought-after for various applications. This chapter aims to provide a comprehensive overview of machine learning and deep learning, shedding light on the systematic foundation of present-day intelligent systems [JAN 21].

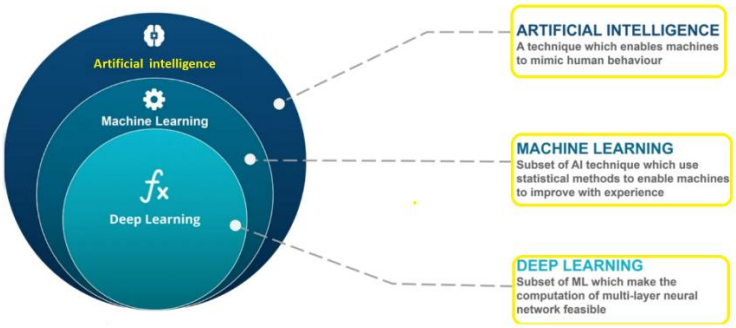


**Fig III.1** Specialization of AI algorithms

## III.2 Machine learning categories:

This section reviews the categorizes of machine learning (ML) which can be divided into three groups as presented in Fig.III.2, which is supervised learning, unsupervised learning and reinforcement learning. More details in the following sections.

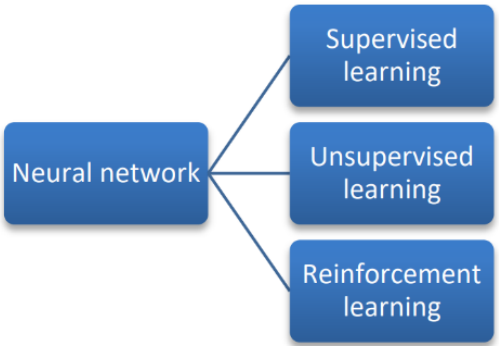


**Fig III.2** Types of learning in Neural Networks

### II.2.1 Supervised learning

In supervised learning, systems utilize datasets with labeled examples, denoted as x for the input data and y for the corresponding true prediction. These labeled pairs form a training set, which is employed to discover a deterministic function capable of mapping any input to the correct output. The primary objective is to make accurate predictions for future input-output observations while minimizing errors to the greatest extent possible [MAR 03].

Supervised learning problems can be categorized into two main types: regression and classification. In classification problems, the aim is to predict a categorical label or class for a given input, such as determining whether a patient has a "disease" or "no disease." On the other hand, regression problems involve predicting a continuous numerical value for a given input, such as estimating the "dollars" or "weight" associated with a particular scenario. [BEL 21]

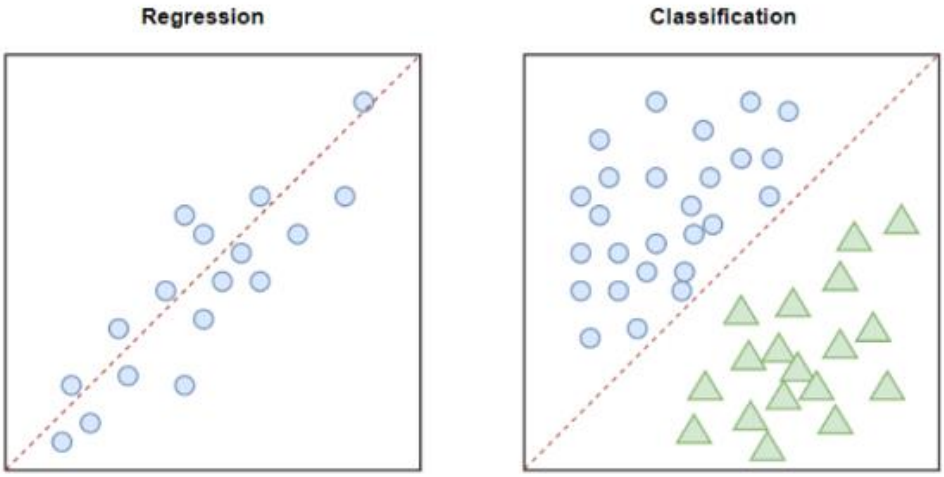


**Fig. III.3** Supervised learning [BEL 21].

### II.2.2 Unsupervised learning

Unsupervised learning is a learning approach wherein the algorithm seeks to uncover patterns and structures within unlabeled input data. This type of learning is particularly valuable for exploratory data analysis, enabling the identification of hidden patterns within large datasets. Typically, unsupervised learning systems employ clustering or association algorithms to perform classification tasks. Clustering algorithms are employed to group similar data points based on their shared features, as illustrated in Fig. III.4. On the other hand, association algorithms aim to discover interesting relationships or associations among variables within a dataset. [BEL 21]

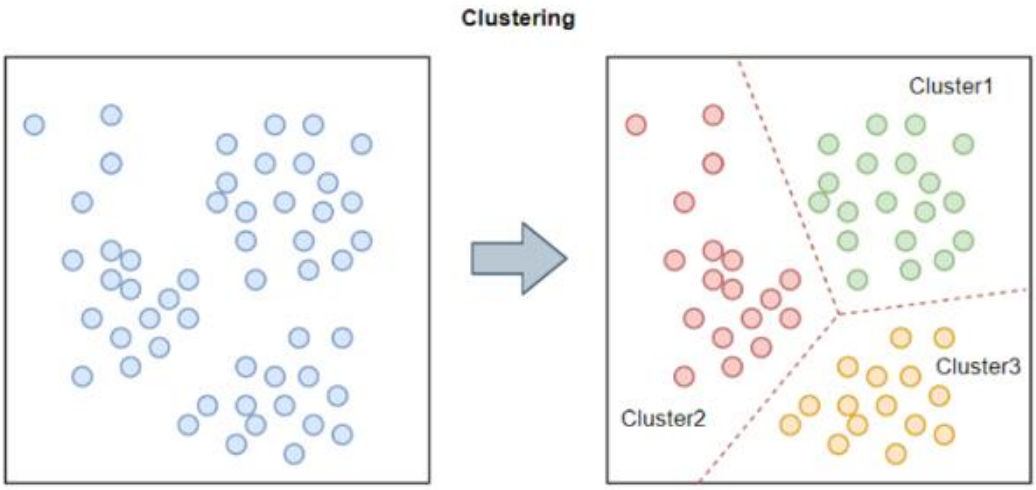


**Fig. III.4** Unsupervised learning [BEL 21].

### III.2.3 Reinforcement learning

Reinforcement learning, categorized as a machine learning algorithm, empowers software agents and machines to autonomously evaluate the most effective behavior within a specific context or environment to enhance their efficiency [KAE 96]. It follows an environment-centric approach, where the learning process is driven by rewards or penalties. The ultimate objective of reinforcement learning is to utilize insights gained from environmental interactions to take actions that maximize rewards or minimize risks [MOH 16]. This learning approach is particularly valuable in training AI models that can enhance automation and optimize the operational efficiency of complex systems such as robotics, autonomous driving, manufacturing, and supply chain logistics. However, it is not recommended for solving basic or straightforward problems [SAR 21].

## III.3 Artificial neural network

Artificial Neural Network (ANN) is a computational model that is designed to simulate the structure and function of the biological neural networks in the brain. It consists of a collection of processing units called neurons, which are interconnected through weighted connections. [BOU 2007]. A typical network model has a set of input patterns and a set of output patterns .The role of the network is to perform a function that associates each input pattern with an output pattern [GUP 99]. The ANN can be trained to recognize a pattern given in the training data by modifying the weights according to a learning rule [BOU07]. The goal of the learning algorithm is to enable the network to make accurate predictions or decisions in real-world application. Many different networks, such as multilayer feedforward networks, recurrent and statistical networks, have been

developed for different purposes. They have a great deal to offer when the problem of interest is made difficult by one or more of the following feature, such as lack of physical or statistical understanding of the problem and nonlinear relationships of the data [GUP 99]. Since most of the traditional linear models are often limited in their ability to model nonlinear relationships between variables. ANNs, on the other hand, are highly flexible and can model complex nonlinear relationships between variables. In short, interest in neural networks is motivated by the following significant properties:

- They learn by experience (not by modeling or programming).
- They can generalize
- most ANN architectures can be implemented online with little computational burden
- They are easy to extend and modify
- they could be easily adapted by the incorporation of new data as they became available
- they can model complex nonlinear relationships between data without requiring a detailed understanding of the underlying physics or statistics

The architecture of an ANN can vary depending on the specific task and the complexity of the data. Some common architectures include feedforward neural networks; Radial basis functions are reviewed as following:

### III.3.1 Multilayer feedforward network:

A multilayer feedforward network is a type of artificial neural network that uses multiple layers of nodes to process input data and produce output. The typical architecture of a multilayer feedforward network is shown in figure III.5. It consists of an input layer, one or more hidden layers, and an output layer. The input layer receives input data in the form of numerical values. Then, passes this data to the hidden layers, where the majority of computation is performed. In fact, each hidden layer contains a set of artificial neurons where this latters work as an elementary processor that receives a number of input of the previous layers and via synaptic coefficients, a set of weights and biases are applied to the entries. The result of this calculation will be subjected to an activation function in order to generate the output function given by:

$$y = f\left[w_n f\left[w_{n-1} \ldots f\left[\ddot{w}_1 u + b_1\right] + \ldots + b_{n-1}\right] + b_n\right] \qquad \text{(III.1)}$$

Where $w_n$ is the weight matrix associated with the ith layer, the vector $b_i$ (i = 1, 2 ... n) represents the threshold values for each node in the ith layer, and f[.] is a nonlinear activation operator. The $w_n$ and $b_i$ are the parameters to be estimated.

The activation function is typically a sigmoid function, a hyperbolic tangent function, or a rectified linear unit (ReLU) function.

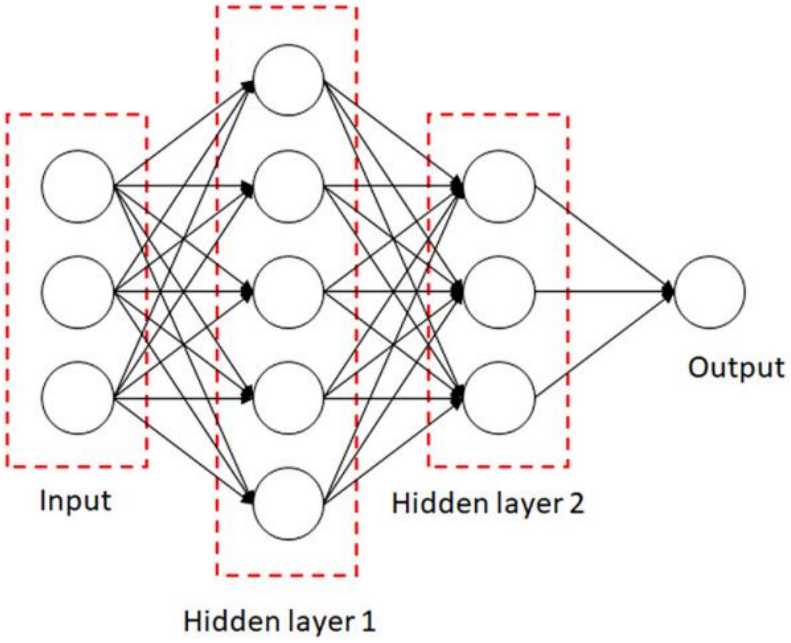


**Fig. III.5** Multi-layer neural network with three inputs, two hidden layers and one output layer.

### III.3.2 Radial Basis Function Networks

A viable alternative to the multilayer perceptron (MLP) is the radial basis function (RBF) network, which is a multilayer feedforward network with a single layer of input, output and a nonlinear processing units hidden layer as presented in Fig. III.6. The output y of an RBF network with an input vector $u \in R^n$ is described by [GUP 99]:

$$y = f(u) = \sum_{i=1}^{N} w_i R_i + w_0 \qquad \text{(III.2)}$$

Where N is the number of neurons in the hidden layer, $w_i$ are the weights of the network. The functions Ri represent the radial basis activation function that is given by:

$$R_i(u) = \phi\left(\|u - c_i\|\right), c_i \in R^n \qquad \text{(III.3)}$$

Where the function $\phi$ has a maximum value at the origin and equal to zero as its argument tends to infinity. Ci is the center vector for i neuron. There are many choices of the function. Gaussian function is commonly chosen in the radial basis function. When the radial basis functions are specified, the only adjustable parameters of the network are the weights. Since these are linearly related to the output y and hence the output error, they can be adjusted using a straightforward least squares approach. This, in turn, has made radial basis networks attractive in identification and control [GUP 99].

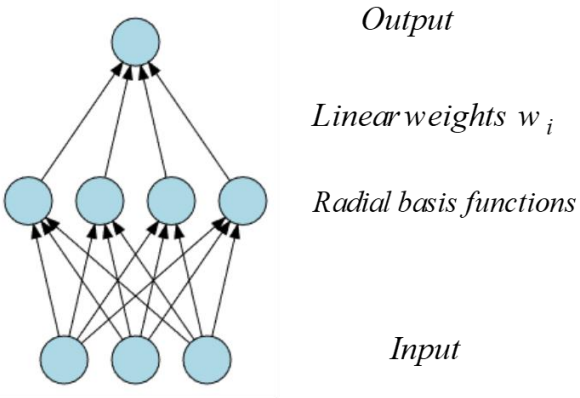


**Fig. III.6** Radial basis functions (RBF) neural network structure

### II.3.3 Recurrent Neural Networks

MLPs have been shown to be useful for modeling static relationships between inputs and outputs in a wide range of applications such as image classification, Medical or fault diagnosis. However, there is a need to increase capabilities of ANN to deal with dynamic models either. For this reason, Recrecurrent neural networks were proposed. RNN are designed to model relationships between input and output taking into account the sequence or temporal nature of the data. RNNs have feedback connections that allow them to maintain a state and use information from previous inputs to inform the processing of the current input. This makes them well suited for tasks that involve predicting or generating sequences of data [GUP 99].

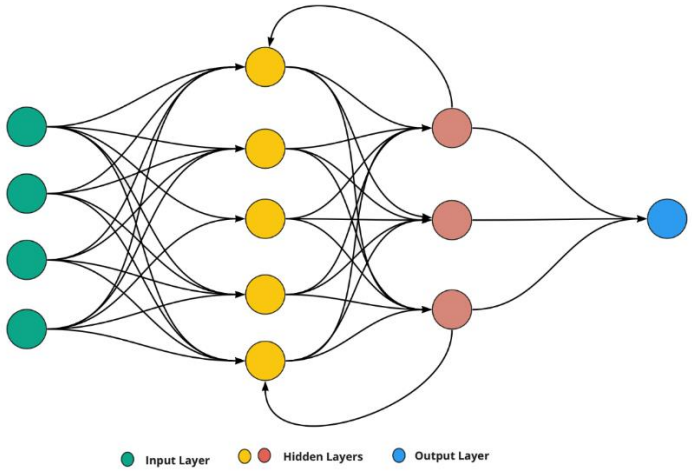


**Fig. III.7** Recurrent Neural Networks

## III.4 Deep Learning

Deep learning (DL), as one of the fastest growing sub-areas of ML, has offered powerful capabilities beyond the reach of humankind and has been increasingly used in wide range of applications [WAN 21, DIN 22]. Unlike the traditional fault diagnosis techniques, DL can extract the features of input samples layer by layer using deep networks and perform automatic feature extraction and classification by the nonlinear activation functions at each layer. Therefore, it requires no manual extraction and gets rid of human intervention and expert knowledge [WAN 21, DIN 22]. The successes of deep learning are built on a foundation of significant algorithmic details and generally can be understood in two parts: construction and training of deep learning architectures. Deep learning architectures are basically artificial neural networks of multiple non-linear layers and several types have been proposed according to input data characteristics and research objectives. In this section, we categorized deep learning approaches into three groups, which is the convolution neural network, deep neural networks (DNNs), Long Short-Term Memory Networks, and explained each group in detail.

### III.4.1 Long Short-Term Memory Networks

Long short-term memory (LSTM) is an advanced version of the standard RNN. The key innovation in LSTM is the addition of gating units mechanism proposed by Hochreiter and Schmidhuber [HOC 97], that helps to overcome the vanishing gradient problem in RNN and therefore allow the network to selectively remember or forget information from previous time steps. As illustrated in Fig .III.8, the common LSTM unit is composed of a cell state (denoted by Ct), a forget gate (ft), an input gate (it), and an output gate (ot). The three gates regulate the flow

of information into and out the channel and important information over arbitrary time intervals can be remembered. The formulas for the three gates and the LSTM structure are as follows [WEI 21]:

$$f_t = \sigma\left(W_{fx} x_t + W_{fh} h_{t-1} + b_f\right) \quad \text{(III.4)}$$

$$i_t = \sigma\left(W_{ix} x_t + W_{ih} h_{t-1} + b_i\right) \quad \text{(III.5)}$$

$$o_t = \sigma\left(W_{ox} x_t + W_{oh} h_{t-1} + b_o\right) \quad \text{(III.6)}$$

$$C_t = f_t \odot C_{t-1} + i_t \odot \tilde{C}_t \quad \text{(III.7)}$$

$$\tilde{C}_t = \tanh\left(W_{Cx} x_t + W_{Ch} h_{t-1} + b_C\right) \quad \text{(III.8)}$$

$$h_t = o_t \odot \tanh(C_t) \quad \text{(III.9)}$$

where $f_t$, $i_t$, $o_t$, are the forget gate, input gate and output gate, respectively; σ() denotes the sigmoid activation function, $W_{fh}$, $W_{ih}$, $W_{oh}$, $W_{Ch}$ are the interconnected weight matrices of the three gates and cell state, respectively; $W_{fx}$, $W_{ix}$, $W_{ox}$, $W_{Cx}$ denote the input weight matrices in the three gates and the cell state, respectively; bf, bi, bo, bC are the corresponding bias terms; $C_t$, $C_{t-1}$ and $C_{\sim t}$ are the current cell state, previous cell state and the candidate cell state, respectively; ⊙ represents Hadamard product (or element product) of matrix.

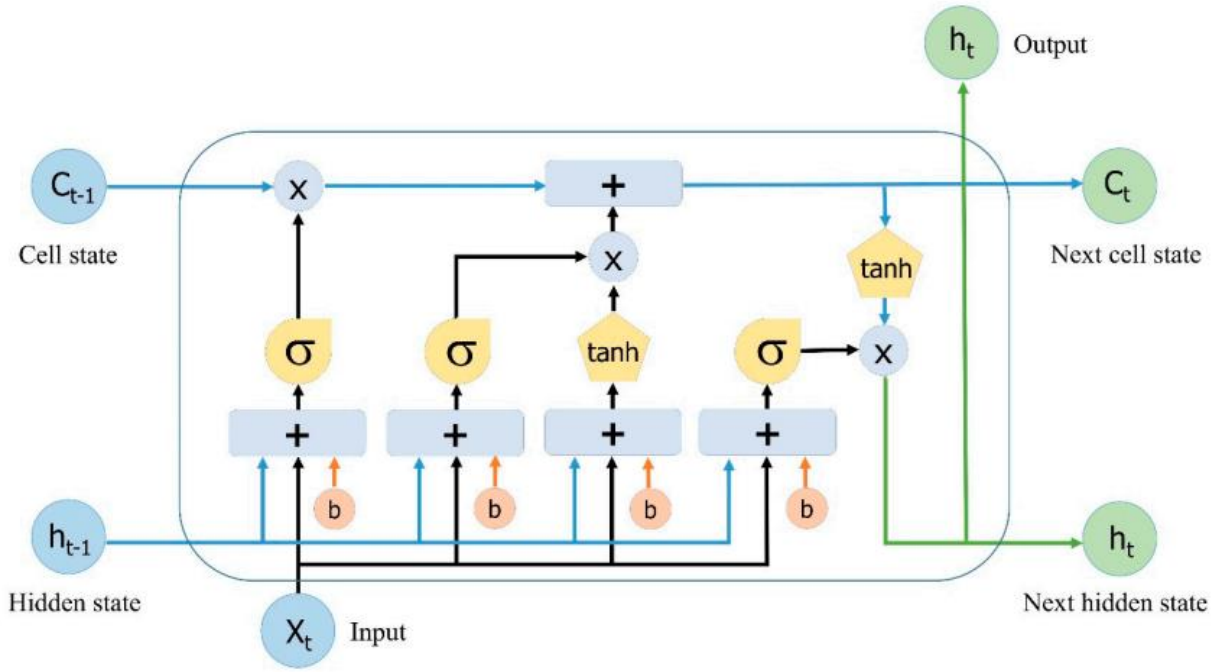


**Fig. III.8** Long short-term memory (LSTM) structure [LE 19].

### III.4.2 Autoencoder

Autoencoders are a kind of supervised deep learning models that was proposed by Geoffrey Hinton [HIN 11]. Their main purpose is learning in an unsupervised manner an informative representation of the data that can be used for various implications such as clustering [BAN 20]. It is very useful in the field of unsupervised machine learning. They can be used for data compression and feature extraction. They composed of two main parts: an encoder and a decoder [BAL 12].

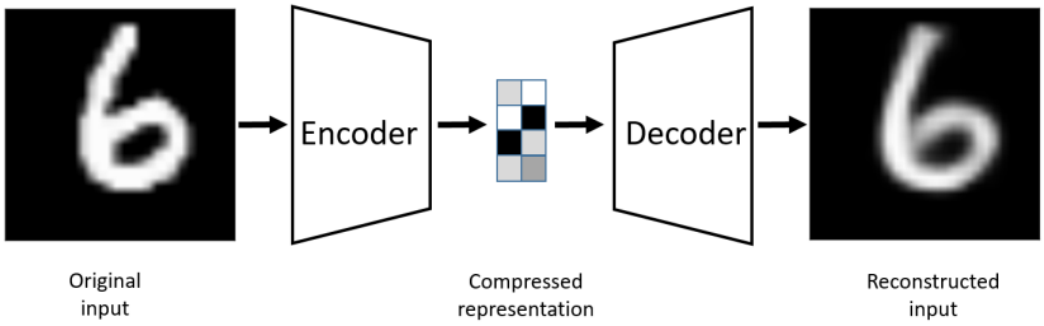


**Fig. III.9** An auto encoder example. The input image is encoded to a compressed representation and then decoded [BAN 20].

### III.4.3. Convolution neural network (CNN)

Convolutional Neural Networks (ConvNets) represent a formidable class of deep learning models that possess specialized architecture for effectively handling and interpreting visual information and data such as images and videos. The introduction of these networks stands as one of the most influential innovations in the realm of computer science driving remarkable advancements in critical tasks as Image Recognition, Object Detection, and Image Segmentation [ADI 19]. This achievement prompted researchers, engineers, and developers from various sectors to explore and exploit CNN in solving complex problems, which was not possible with traditional methods [ALB 17]. This transformation has also encompassed and revolutionized the fault diagnosis sector by enabling more accurate and robust fault detection in diverse systems, including industrial machinery, power grids, transportation networks, and healthcare devices.

### III.4.3.1 Convolutional neural network elements

Before to diving into the experimental details of this thesis, we first introduce the basic terminologies and elements regarding the CNN to obtain a good grasp of it, since this thesis is based on CNN, we start with its fundamental components.

- **Convolution:**

The convolutional layer is a fundamental component in deep learning, playing a crucial role in extracting patterns from data. It achieves this by applying a set of filters, also known as kernels, to the input images, effectively extracting valuable features. The core operation of the convolutional layer involves performing a dot product calculation between the filter values and the pixel values of the images. This operation serves as the main assumption underlying the process of feature extraction in the convolutional layer. This process also involves sliding the filter over the image, resulting in the formation of a matrix known as the Convolved Feature, Activation Map, or Feature Map. The outline of the convolution function can be given by [DIN 17]:

$$x_n^{r,k} = \psi\left(\sum_m w_n^r * x_m^{r-1} + b_n^r\right) \tag{III.10}$$

Where $x_m^{r-1}$ and $x_n^{r,k}$ are respectively, the $mth$ input of level r −1 and $nth$ output feature maps of level r in the convolution process. $w_n^r$ is the convolution kernel between the $mth$ input feature map and the nth output feature map and k is the number of the kernels. $b_n^r$ is the bias of the nth output feature maps.

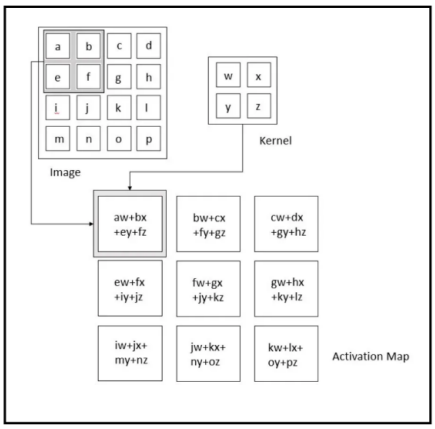


**Fig. III.10** Convolution principle

It can be seen that the different feature maps as input share the same kernels and bias. * Denote the convolution operator and ψ (•) is a nonlinear activation function, which is set to be "sigmoid" or "ReLU" [DIN 17].

- **Nonlinearity:**

After the convolution layer, the next component in the neural network architecture is the non-linearity layer. This layer plays a crucial role in modifying or filtering the output generated by the previous layer. Its purpose is to introduce saturation or limitations to the output. Traditionally, sigmoid and tanh functions have been widely employed as popular choices for non-linearity. Fig. III. 11 displays various commonly used types of nonlinearity. Nevertheless, in recent times, the Rectified Linear Unit (ReLU) has gained significant popularity due to several compelling reasons [ALB 17].

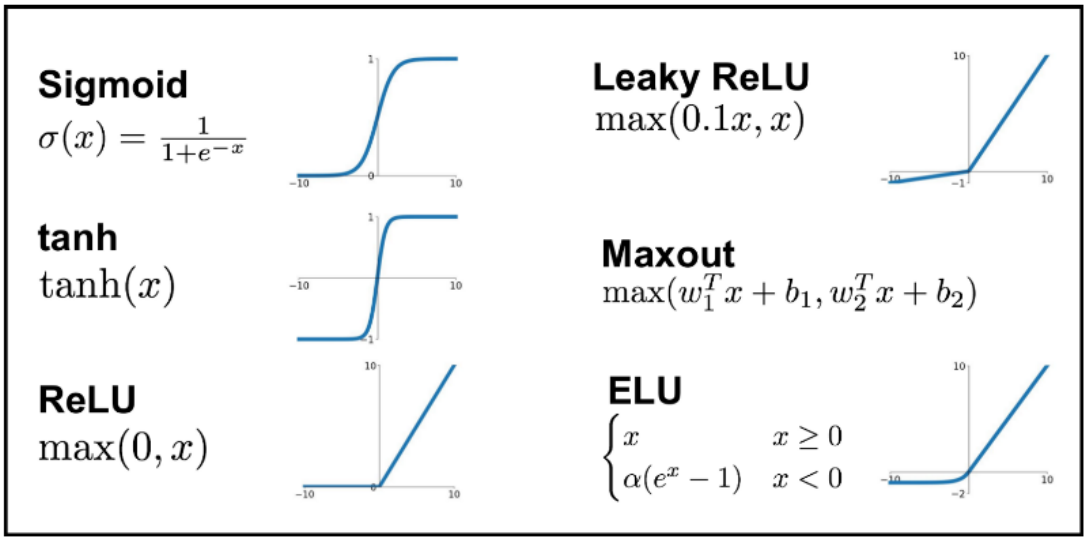


**Fig. III.11** Different types of nonlinearity

- **Pooling**:

Pooling layers, also known as downsampling layers, are essential in reducing the dimensionality of the input, effectively decreasing the number of parameters involved. Like convolutional layers, pooling operations involve the traversal of a filter across the input data. However, pooling filters differ from convolutional filters in that they lack weights. Instead, the pooling filter applies an aggregation function to the values within its receptive field, producing an output array. Commonly, two main types of pooling operations are employed [AFA 23]:

- Max pooling: During the movement of the filter across the input, the pixel with the highest value is selected and propagated to the output array. Notably, this approach is more commonly utilized compared to average pooling due to its effectiveness (Fig. III.12).
- Average pooling: As the filter traverses the input, it computes the average value within its receptive field and transmits it to the output array.

In summary, pooling layers play a vital role in CNNs by balancing complexity, improving efficiency, and reducing the risk of overfitting. While information loss occurs, the benefits gained from pooling contribute to more effective and scalable deep learning models.

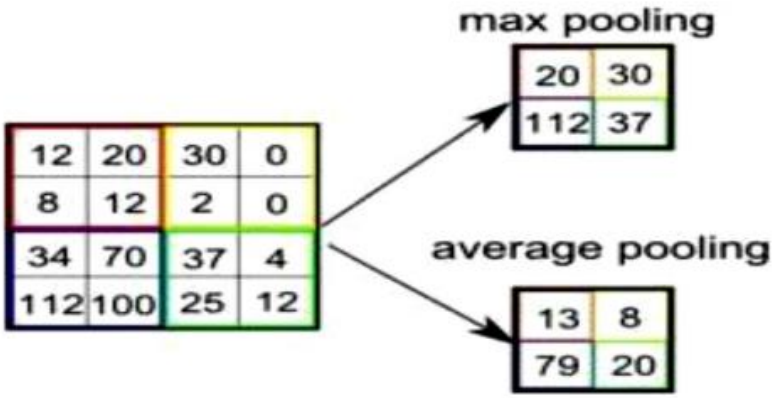


**Fig. III.12** Simple pooling operation

- **Fully Connected Layer**

The Fully Connected (FC) Layer, also known as the dense layer, is designed to establish comprehensive connectivity among all neurons within the layer. In contrast to convolutional and pooling layers that primarily operate on localized spatial regions, the fully connected layer establishes connections between each neuron and every neuron in both the preceding and succeeding layers . This global connectivity allows for information flow and interaction across the entire network, enabling a more holistic understanding of the data [AFA 23]. In general, the role of the Fully Connected Layer is to perform classification based on the features extracted by preceding layers and their respective filters (see Fig. III.13). While convolutional and pooling layers often employ Rectified Linear Unit (ReLU) functions, the FC layers typically utilize the softmax activation function for accurate classification. This activation function assigns a probability value between 0 and 1 to each class.

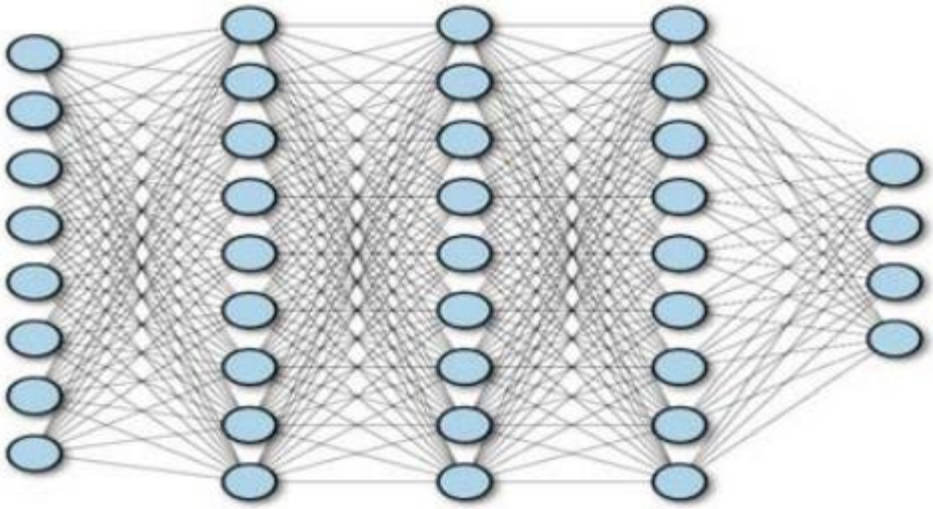

**Fig. III.13** Example of CNN using Fully connected layer [HOS 19]

- **BatchNormalisation**

Batch normalization (BN) is a technique used to improve the training of deep neural networks. It is a form of regularization that allows the network to learn faster and reduces the chances of overfitting. Batch normalization works by normalizing the activations of the neurons in each layer. This ensures that the distribution of the activations remains the same even as the network learns. This allows the network to train faster and reduces the chances of overfitting. Batch normalization is a relatively new technique and is still being researched. However, it has already shown to be promising and has been used in a number of successful deep learning models. The computation of BN is written by [LUO 18] as follow:

$$y = g(\hat{h}), \hat{h} = \gamma \frac{h - \mu\varepsilon}{\sigma\varepsilon} + \beta, h = w^T x \qquad \text{(III.11)}$$

- **Dropout**

Dropout in neural networks involves temporarily excluding units (both hidden and visible) from the network, along with their corresponding connections. This exclusion is random, as shown in Figure 1.

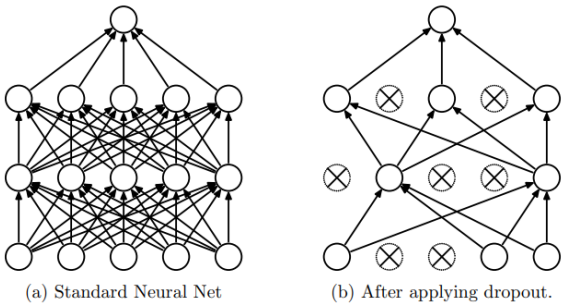


**Fig. III.14** (a) Standard Neural Net Model (b) After applying dropout [SRI 14].

Each unit is independently retained or dropped based on a fixed probability p. This probability can be determined using a validation set or set to a common value such as 0.5, which has been found to yield favorable results for a wide range of network architectures and tasks [SRI 14].

### III.4.3.2 Popular CNN architecture

In the past decade, multiple CNN architectures have been introduced, each playing a crucial role in enhancing the performance of various applications. CNN architecture has undergone several modifications since 1989, including structural reformation, regularization techniques, parameter optimizations, and more. However, it is important to acknowledge that significant improvements in CNN performance have largely been driven by the reorganization of processing units and the development of innovative blocks. Notably, the most noteworthy advancements in CNN architectures have revolved around the exploration of network depth. In this part, we will examine a range of popular CNN architectures, starting from AlexNet model in 2012 and concluding with the High-Resolution (HR) model in 2020. By analyzing the distinctive features of these architectures, such as input size, depth, and robustness, researchers can effectively select the most suitable architecture for their specific task [ALZ 21].

- **AlexNet**

AlexNet revolutionized the field of Computer Vision by popularizing Convolutional Neural Networks (CNNs). This model is developed by Alex Krizhevsky et al [ZHE 12] , this groundbreaking architecture consisted of five convolutional layers followed by three fully connected layers. In the ImageNet Large Scale Visual Recognition Challenge (ILSVRC) held in 2012, AlexNet showcased its superiority by achieving remarkable results. [COS 17].

- **VGGNet**

VGGNet, developed by the Visual Geometry Group (VGG) group at Oxford and the runner-up in ILSVRC 2014, introduced significant improvements over AlexNet. With a total of 19 layers, VGGNet's key contribution was highlighting the crucial role of network depth in achieving superior performance. VGGNet demonstrated that increasing the number of layers positively impacted accuracy. While VGGNet achieved remarkable accuracy on the ImageNet dataset, its deployment on GPUs, even those with modest sizes, posed challenges due to substantial computational requirements. The network's large width in convolutional layers led to inefficiencies in terms of memory usage and processing time. In other words, VGGNet's success lay in emphasizing the importance of network depth for improved performance. However, its practical deployment faced obstacles due to significant computational demands arising from its wide convolutional layers [COS 17].

- **GoogleNet**

GoogLeNet, the winning entry of ILSVRC 2014 developed by Szegedy et al [SZE 15]. at Google, introduced several key innovations. Its inception module played a pivotal role in significantly reducing the network's parameter count. The inception module accomplished this by approximating a sparse convolutional neural network with a more compact and dense construction. By employing convolutional filters with reduced width and incorporating convolutions of different sizes, GoogLeNet effectively captured details at multiple scales. A noteworthy aspect of the inception module was the inclusion of a bottleneck layer, which greatly reduced computational requirements. Another notable change introduced by GoogLeNet was the replacement of fully connected layers (FCLs) with a simple global average pooling operation. This pooling operation averaged the channel values across the 2D feature map after the final convolutional layer, leading to a significant reduction in the overall number of parameters. This was a departure from architectures like AlexNet, where FCLs accounted for a large portion of the network's parameters. GoogLeNet achieved an impressive top-5 accuracy of 93.3% on the ImageNet dataset while exhibiting superior speed compared to the VGG architecture. This success was attributed to GoogLeNet's wider and deeper network design, which enabled the removal of FCLs without compromising accuracy [COS 17].

- **Residual Network**

The Residual Network (ResNet), created by Kaiming He et al [KAI 18], emerged as the victor in the prestigious ILSVRC 2015 competition. A remarkable aspect of ResNet was its

unprecedented depth, consisting of an astonishing 152 layers—a tenfold increase compared to the prevailing network architectures at the time of its inception. This achievement was made possible by incorporating skip connections and extensively employing batch normalization techniques. Furthermore, ResNet employed global average pooling followed by a classification layer. In terms of performance, ResNet surpassed both VGGNet and GoogLeNet in accuracy while maintaining computational efficiency, particularly outperforming VGGNet. The ResNet-152 variant, specifically, achieved an impressive top-5 accuracy rate of 95.51% [COS 17].

- **SqueezNet**

SqueezNet, as highlighted in [LAN 16], achieves nearly the same accuracy as AlexNet while possessing a significantly reduced parameter count of 50 times less. The key focus of SqueezNet lies in minimizing network parameters by employing a 1x1-convolution kernel to reduce the feature map. The network construction incorporates the concept of stacking. At the heart of SqueezNet lies the Fire module, which serves as the core component. This module consists of two layers: a squeeze layer utilizing a 1x1-convolution kernel, and an expand layer utilizing both 1x1 and 3x3 convolution kernels. The architectural structure of the Fire module is illustrated in Fig. III. 15 [ZHO 20]. In the depicted figure, the input to the Fire module structure is H×W×N, resulting in an output of H×W×(E1+E3). The Fire module encompasses three adjustable parameters: S1, E1, and E3. These parameters denote the number of convolution kernels, representing the output channel dimension. Notably, the resolution of the feature map remains unchanged, only the number of channels is altered. To reduce network parameters, it is essential to minimize both the quantity of 3×3 convolution kernels and the number of channels input into these kernels. This reduction in the number of 3×3 convolution kernels is achieved by substituting them with 1×1 convolution kernels. Additionally, the squeeze layer employs a 1×1 convolution kernel to constrain the number of channels produced by the squeeze layer. By employing these strategies, SqueezeNet effectively decreases the number of network parameters while preserving the feature map resolution [ZHO 20].

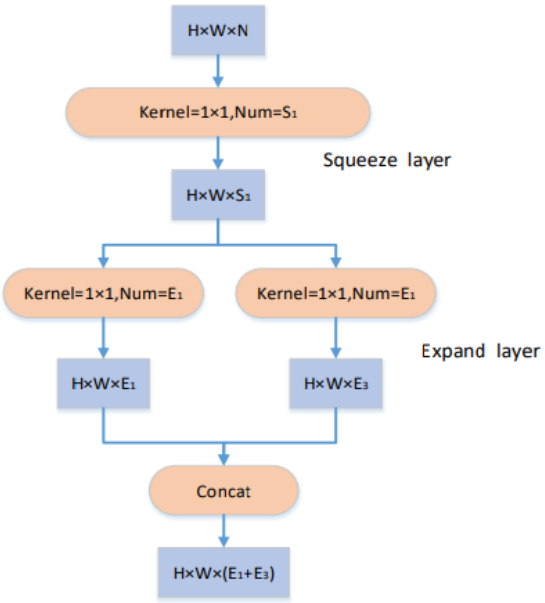


**Fig. III.15** Fire module structure [ZHO 20].

Table 1 illustrates the comprehensive network structure of SqueezeNet, which relies on the stacked implementation of Fire modules. The Fire modules exhibit an increasing number of convolution kernels as the network progresses. Specific components in the architecture include the initial independent convolutional layer (Conv1) and subsequent utilization of the maximum pooling layer (Max pool) after Fire4 and Fire8. Following the last convolutional layer (Conv10), an average pooling layer (Avg pool10) is applied. The deliberate placement of pooling operations at later stages, such as Avg pool10, aims to generate larger activation maps within the convolutional layers. Larger activation maps have been associated with higher classification accuracy. The size of the activation map depends on both the input data dimensions and the choice of layers subjected to pooling. By incorporating larger strides early in the network, the activation graphs of most layers would be smaller. Consequently, SqueezeNet strategically employs a stride of 1 for most layers, while strides larger than 1 are primarily applied towards the end of the network. This approach ensures that a majority of layers maintain large activation maps, leading to enhanced accuracy [ZHO 20].

Table.III.1 SqueezNet overall network structure

| Layer name | Output size | Filter size/stride |
|---|---|---|
| Input image | 224x224x3 | |
| Conv1 | 111x111x96 | 7x7/2(x96) |
| Max pool1 | 55x55x128 | 3x3/2 |
| Fire2 | 55x55x128 | |
| Fire3 | 55x55x256 | |
| Fire4 | 55x55x256 | |
| Max pool4 | 27x27x256 | 3x3/2 |
| Fire5 | 27x27x256 | |
| Fire6 | 27x27x384 | |
| Fire7 | 27x27x384 | |
| Fire8 | 27x27x512 | |
| Max pool8 | 13x13x512 | 3x3/2 |
| Fire9 | 13x13x512 | |
| Conv10 | 13x13x1000 | 1x1x1/1(x1000) |
| Avg pool10 | 1x1x1000 | 13x13/1 |

- **MobileNet**

MobileNetV1, as highlighted in [HOW 17], introduces a significant innovation known as depthwise separable convolution. This architectural approach completely replaces traditional standard convolutions throughout the network. The streamlined design of MobileNetV1 leverages depthwise separable convolutions as the foundation. MobileNetV1 stands out by omitting pooling layers entirely and employing depthwise separable convolutions with a stride of 2 for downsampling operations. This enables downsampling while reducing parameters and computations. By utilizing depthwise separable convolutions, MobileNetV1 achieves a substantial reduction in the number of parameters and calculations required. The model incorporates two essential hyperparameters: the width factor and the resolution factor. The width factor enables adjustments to the input and output dimensions, thereby allowing control over the parameter count. Similarly, the resolution factor enables resizing of the input data, providing control over the computational requirements. In MobileNetV1, multiplying the input and output channel dimensions by a width factor (typically ranging from 0 to 1) and scaling the input data by a

resolution factor further contributes to the reduction in model size and computational load. These techniques enable customization of the network to strike a balance between model complexity and efficiency [ZHO 20].

- **ShuffleNet**

ShuffleNetV1, described in [ZHA 18], tackles the limitations of information flow between channels resulting from group convolutions through the implementation of a shuffle operation. Fig. III.16 (a) illustrates that when group convolutions are utilized with three groups, each group performs its own convolution operations independently, leading to a reduction in the network's feature extraction capability. To uphold the network's recognition accuracy, Fig. III.16 (b) demonstrates that the feature map obtained after group convolution is reorganized. This reorganization ensures that the input information for the subsequent group convolution originates from different groups. This operation is depicted in Fig. III.16 (c). It is important to note that the

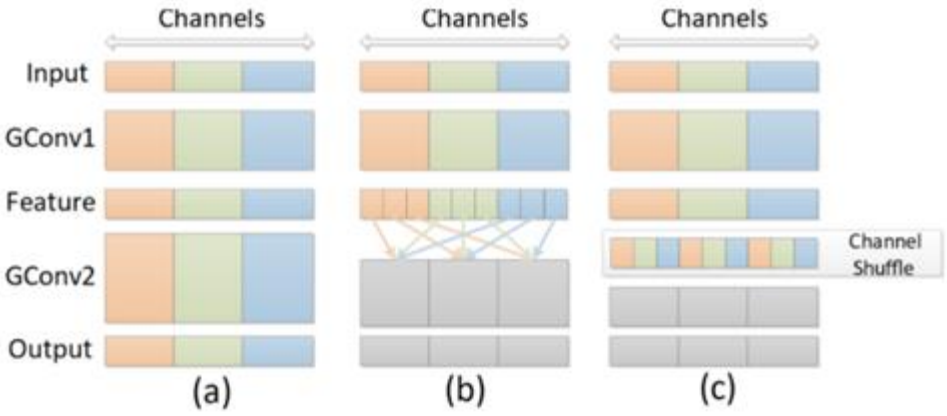


Fig.III.16 Channel shuffle with two stacked group convolutions. GConv stands for group convolution. a) two stacked convolution layers with the same number of groups. Each output channel only related to the input channels within the group. No cross talk; b) input and output are fully related when GConv2 takes data from different groups after GConv1 ; c) an equivalent implementation to b) using channel shuffle [ZHO 20].

channel shuffle operation is not conducted randomly; rather, it systematically disrupts the channels in an evenly distributed manner.

- **EfficientNet**

EfficientNet addresses the challenge of improving model generalization performance by simultaneously adjusting the depth, width, and resolution of the network. It recognizes that simply

increasing a single parameter will lead to saturation in model accuracy. In order to optimize these three parameters, EfficientNet introduces a compound coefficient that enables dynamic enhancement through model scaling. The compound coefficient, as depicted in Fig. III.17, ensures a balanced adjustment of the network's depth, width, and resolution, thereby maximizing overall performance. By achieving this balance, EfficientNet significantly reduces the number of parameters and computations without sacrificing accuracy. This approach allows for efficient utilization of network resources while maintaining high-quality results [ZHO 20].

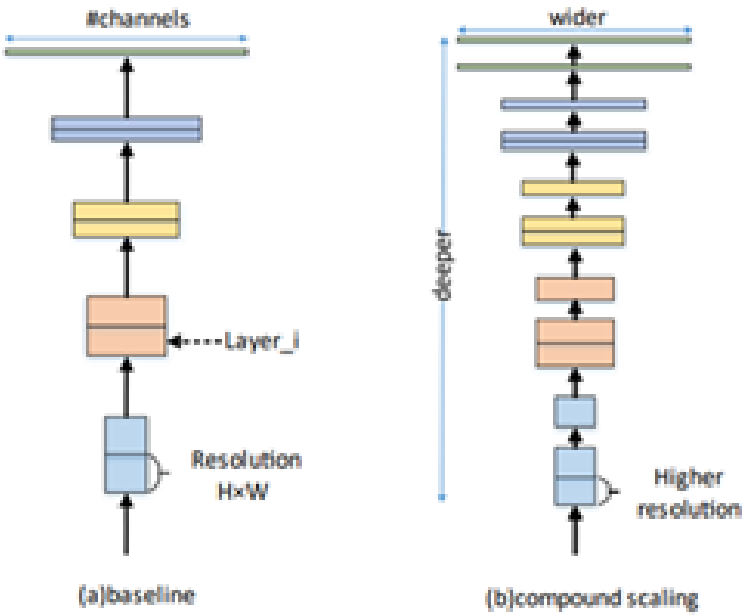


**Fig. III.17** Baseline and compound scaling [ZHO 20]

To scale the compound model effectively, the initial step involves conducting a grid search to establish the relationship between various parameters of the baseline network while adhering to fixed resource constraints. This search determines the suitable scale factors for depth, width, and resolution. Utilizing these coefficients, the baseline network is expanded to create the desired network size. The success of this model extension heavily relies on the design of the baseline network. In order to optimize both accuracy and efficiency, a novel baseline network is devised using Neural Architecture Search (NAS) techniques. NAS enables the exploration of diverse architectural configurations to identify an optimal network structure. By leveraging NAS, the baseline network is carefully crafted to strike the right balance between accuracy and computational efficiency, laying the foundation for effective scaling of the compound model.

### III.4.4 Transfer learning

Transfer learning is a machine learning technique that involves taking a model originally created for one task and using it as the foundation for a model to perform a different task. In simpler terms, it is an approach within deep learning and machine learning where knowledge gained from one model is applied to another [TOR 10]. With this method, pre-trained models serve as the starting point for tasks in computer vision instead of constructing models from scratch. This approach addresses the challenges posed by the significant computational and storage resources typically required for developing Deep Learning models. However, it is important to emphasize that transfer learning is effective in deep learning only when the features learned from the initial task are broadly applicable [PAN 09]. Transfer learning has emerged as the preferred method for working with deep learning models. The reasons are outlined below:

- **Data Efficiency**: Transfer learning allows deep learning models to leverage pre-existing knowledge gained from large and diverse datasets. This is particularly valuable when you have limited data for a specific task, as the model can transfer knowledge from a related domain or task.
- **Faster Training**: Starting with pre-trained models significantly reduces the time and computational resources required to train a deep learning model from scratch. Fine-tuning on a new task is generally quicker compared to training a brand-new model.
- **Improved Performance**: Transfer learning often leads to better model performance, especially when the pre-trained model has been trained on a vast and diverse dataset. It can capture high-level features that are generally useful across multiple tasks.
- **Generalization**: Pre-trained models are trained on extensive and varied data, enabling them to learn general features that are not specific to a single task. This enhances the model's ability to generalize to new, unseen data**.**

### III.5 Model evaluation

Evaluating a model is a crucial step throughout the development of the model. Evaluation metrics have a correlation with machine learning tasks. Figure III.18 illustrates various evaluation metrics based on the type of tasks (classification, regression, etc.) all have different metrics. In this section, we are going to shed light on the evaluation metrics used for classification [BEL 21].

- **Accuracy** refers to the whole number of instances that may be classified correctly. It is given by:

$$Accuracy = \frac{TP + TN}{TN + TP + FP + FN} \quad \text{(III.12)}$$

- **Sensitivity** measures the quantity of TP instances, which are correctly identified by the classifier. It is given by:

$$Sensitivity = \frac{TP}{TP + FN} \quad \text{(III.13)}$$

- **Specificity** measures the quantity of TN instances, which are correctly identified by the classifier. It is given by:

$$Specificity = \frac{TN}{TN + FP} \quad \text{(III.14)}$$

- **Precision** measures the amount of predicted TP that is truly related to the TP class. It is given by:

$$\text{Pr}ecision = \frac{TP}{TP + FP} \quad \text{(III.15)}$$

- **F1-score** is a combination of precision and sensitivity. Therefore, a high value of F-measure shows a high value of both precision and sensitivity. It is given by:

$$F1 - score = 2\frac{precision * sensitivity}{precision + sensitivity} \quad \text{(III.16)}$$

## III.6 Conclusion

In this chapter, we offer a comprehensive overview of Machine Learning (ML) and Deep Learning (DL), which are frequently categorized as components of Artificial Intelligence (AI) technology. These technologies play a pivotal role in shaping the analytical models that drive both current and forthcoming intelligent systems. Our presentation encompasses the conceptualization of ML, shallow ML, and DL, along with insights into their respective algorithms and architectural designs.

Chapter 4

# Fault diagnosis of broken rotor bars using STTLS-Music and ANN

## IV.1 introduction

The rapid evolution of the manufacturing industry has significantly increased the importance of machine fault diagnosis. Ensuring the reliable operation of equipment and production processes has become paramount. Consequently, there has been extensive exploration and refinement of various methods in recent years, marked by a noticeable and rapid evolution of intelligent algorithms. Among these methodologies, Artificial Neural Networks (ANNs) have emerged as a prominent example of intelligent diagnostic models. Over the past decade, ANNs have undergone thorough investigation and widespread utilization [JIA 20]. In this context, this chapter presents a novel contribution: the development of an automated fault diagnosis system based on ANN models to address the challenge of overlapping data in the diagnosis of broken rotor bar faults using diverse signal processing techniques. First, we present distinctive methodologies tailored for the identification and examination of obstacles associated with faults in broken rotor bars. These challenges involve issues such as frequency leakage and overlapping data, and our methodologies employ both traditional and advanced signal processing techniques. Specifically, we utilize Fast Fourier transform, Hilbert transform, and discreet wavelet transform. While the proposed approach offers a solution to these challenges through the implementation of improving multiple signal classification (MUSIC) and ANN technology.

## IV.2 Motivation

Early identification of faults in induction motors is of paramount importance due to their crucial role in industrial applications. Among these faults, the Broken Rotor Bar (BRB) fault stands out as particularly significant due to its potential for causing extensive damage. The rotor bars may fail due to various stresses, including thermal, magnetic, mechanical, dynamic, residual, and environmental stresses. Artificial neural networks (ANNs) are increasingly being integrated into the field of rotating machinery fault diagnosis. This adoption is primarily attributed to their remarkable learning capabilities, enabling ANNs to effectively tackle new problems by leveraging existing information. In rotating machinery fault diagnosis, an ANNs is usually trained on features extracted from acquired signals. To achieve an efficient diagnostic process in terms of both time and accuracy, various techniques have been employed. The authors in [DEF 21, SIN 21] presented an approach to diagnosis of BRB fault using discrete wavelet transform and neural network algorithm. The authors in [LAA 20, RAM 20, Yan 21, KUM 23] propose an approach for the detection of broken rotor bar (BRB) fault in three phase induction motor drive using Hilbert transform (HT) and artificial neural networks (ANNs). A rotor fault diagnosis method based on

the combination of Modified Ensemble Empirical Mode Decomposition (MEEMD) energy entropy and ANN is proposed in [Yan 21]. In spite of the various techniques quoted for the detection improvement of BRB, there is still an unresolved issue pertaining to the overlap of data between fault and load effects during analysis. This issue is particularly prominent in cases where the fault-related harmonic is closely linked to the load values. In order to tackle this problem, the first contribution of this thesis aims to propose a solution.

To begin with, we will introduce various distinct signal processing methodologies to elucidate and accentuate the issue of overlapping data. The initial method will center on the utilization of non-parametric techniques. In this section, we will study this issue using at first Fast Fourier transform, Hilbert transform technique and finally, the discrete wavelet transform along with Hilbert transform to the stator current signal for the purpose of diagnosing the fault associated with broken rotor bars using the envelope signal. However, before employing these techniques to confirm the presence of this defect in the envelope signal extracted by the Hilbert transform, we will establish a theoretical foundation demonstrating the occurrence of the broken rotor bar signature in the envelope signal.

Subsequently, we will compute the energy of the resulting DWT coefficients using a specific criterion to assess the performance of this method in diagnosing broken rotor bars. On the other hand, in the following section, we will propose a new method based on improved MUSIC and ANN to solve the challenges encountered in the analysis of the aforementioned methods. Within this framework, we will improve this technique to accommodate non-stationary signals .In this proposed technique. This hybrid approach aims to establish a robust methodology for the automated early detection and localization of broken rotor bar faults in induction machines, all while circumventing and solving the issue of overlapping data.

## IV.3 Stator Phase Current Amplitude in Case of Broken Rotor Fault

The current signature in the stator phase during a broken bar fault condition exhibits sideband frequencies. It can be expressed as [KIA 09]:

$$i_A(t) = i_f \cos(\omega t - \varphi) + \sum_k i_l^k \cos\left((\omega - \omega_f^k)t - \varphi_l^k\right) + \sum_k i_r^k \cos\left((\omega + \omega_f^k)t - \varphi_r^k\right) \quad \text{(IV.1)}$$

Where $i_f$ is the fundamental value of the phase stator current, $\omega$ is the fundamental angular frequency, $\varphi$ is the phase shift angle of the phase stator current. $\omega_f^k = 2ks\omega$ and $i_l^k, i_r^k, \varphi_l^k$ and $\varphi_r^k$

$(k = 1,2,3,...)$ are the amplitude and phase shift angle of the left and right side band fault characteristics respectively.

The stator current can be expressed as:

$$i_A(t) = A(t)\cos\omega t + B(t)\sin\omega t = C(t)\sin\left(\varphi(t)\right) \quad \text{(IV.2)}$$

Where:

$$A(t) = I_f \cos(\varphi) + \sum_k \begin{pmatrix} (I_l^k \cos\varphi_l^k + I_r^k \cos\varphi_r^k)\cos(2\pi(2k\ s\ \omega)t) + \\ (I_r^k \sin\varphi_r^k - I_l^k \sin\varphi_l^k)\sin(2\pi(2k\ s\ \omega)t) \end{pmatrix} \quad \text{(IV.3)}$$

$$B(t) = I_f \sin(\varphi) + \sum_k \begin{pmatrix} (I_l^k \sin\varphi_l^k + I_r^k \sin\varphi_r^k)\cos(2\pi(2k\ s\ \omega)t) + \\ (I_l^k \cos\varphi_l^k - I_r^k \cos\varphi_l^k)\sin(2\pi(2k\ s\ \omega)t) \end{pmatrix} \quad \text{(IV.4)}$$

$$C(t) = \sqrt{A(t)^2 + B(t)^2} \quad \text{(IV.5)}$$

$$\varphi(t) = \omega t + \arctan A(t)/B(t) \quad \text{(IV.6)}$$

Based on equations (IV.3) and (IV.4), the presence of broken rotor bars leads to rotor asymmetry, causing modulation in the stator current amplitude at a frequency ( $2ks\omega$ ). This modulation can be extracted using the Hilbert transform (HT), which is a classical method based on applying a mathematical operation that is used to calculate the instantaneous phase and magnitude of modulated signals. The mathematical operation of HT for the stator current signal $i_A(t)$ can be defined as follows [GUE 2020]:

$$HT(i_A(t)) = y(t) = 1/\pi t * i_A(t) = 1/\pi \int_{-\infty}^{\infty} i_A(\tau) d\tau / (t-\tau) \quad \text{(IV.7)}$$

The so-called analytic signal i(t) is formed by the combination of the real signal with its Hilbert transform given by:

$$i(t) = i_A(t) + jy(t) = a(t)\exp(k\varphi(t)) \quad \text{(IV.8)}$$

Where a(t) and φ(t) is the stator current instantaneous amplitude and its phase.

$$a(t) = \sqrt{i_a(t)^2 + y(t)^2} \quad \text{(IV.9)}$$

$$\varphi(t) = \arctan\left(y(t) / i_A(t)\right) \quad \text{(IV.10)}$$

a(t) is the instantaneous amplitude of $i(t)$ known as envelope of $i_A(t)$ and $\varphi(t)$ is the instantaneous phase of $i(t)$

## IV.4 Dataset description

The experimental test rig used in the investigation of the rotor broken bars occurrence is presented in Fig. IV.1. The experimental tests were carried out on three-phase, 50 Hz, 4-pole, 1.1kw and 3kw squirrel-cage induction motors with 28 bars. Three different rotors were used in the experiments for both induction motors: A healthy one and two others with one and two broken rotor bars. Mechanical load has been provided by a separately synchronous generator feeding a variable resistor. Only one stator current was captured using Hall-Effect clamp probe, and was acquired on 4 s with a sampling frequency of 10 kHz using the NI cDAQ-9184 acquisition device. The acquired data are transferred to the personal computer using an Ethernet cable.

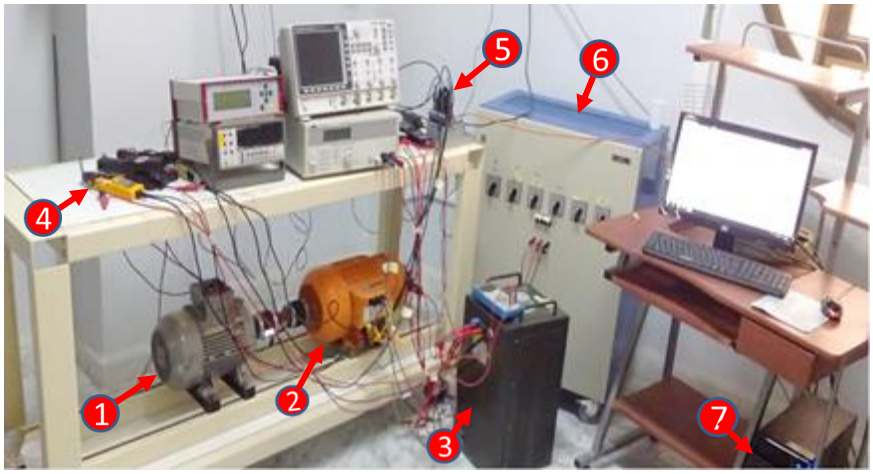


**Fig. IV.1** Experimental test bench: (1) 3-phase, 3kW, Induction motor, (2) Synchronous motor, (3) DC-power supply, (4) stator current sensors, (5) NI cDAQ-9184 acquisition device (6) variable resistor, (7) (Pc) data processing unit.

## IV.5 Diagnosis of BRB fault with classical Signal Processing methods

In this section, our focus shifts towards exploring the issue of overlap that emerges when analyzing and diagnosing broken rotor bar faults. To tackle this challenge comprehensively, we will use three distinct signal-processing methods, each rooted in the theories presented in chapters II. By examining these methods, we aim to find effective alternatives for accurate fault detection and diagnosis to solve this issue.

### IV.5.1 Analysis based on Fast Fourier Transform

Figure IV.2 illustrates the spectral analysis of the current signal using the Fast Fourier Transform (FFT) for a single broken bar under varying load conditions. The results clearly demonstrate that the load significantly influences the amplitude of the sideband Broken Rotor Bar (BRB) components. As the load increases, the amplitudes of these sidebands also increase proportionally. However, although, this method gives a high resolution analysis of the BRB sideband frequencies but it is clearly fail in such cases when the load is at very low level. In this situation, the slip s is very low and the sideband components practically overlap the supply frequency (frequency leakage). This makes it difficult to detect their presence and to use them for the diagnosis.

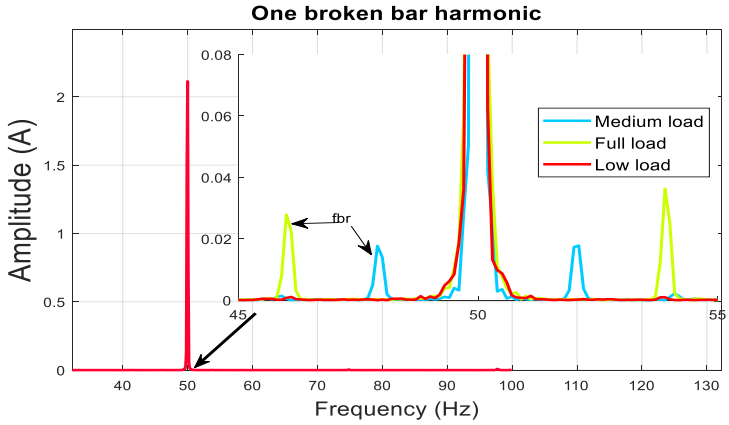


**Fig. IV.2** The FFT spectrum of the stator current signal

### IV.5.2 Analysis Based on Hilbert Transform method

In order to surmount the drawback mentioned in the previous section; which is embodied by the harmful effect, at low load, of the fundamental harmonic on the detection of BRB harmonics. It is easier to analyze the envelope of the stator current than the current itself. This is well justified by equations (IV.3), (IV.4) and (IV.5).

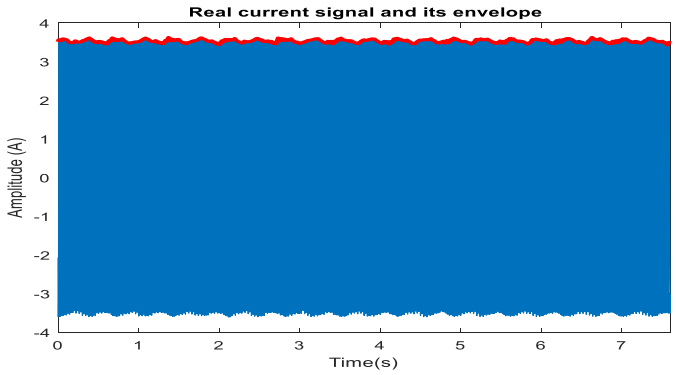


**Fig. IV.3** The raw stator current and its envelope

Multiple experiments were conducted on both healthy and faulty rotors, varying the load conditions in each test. During these experiments, the stator current of one phase was collected and processed using the Hilbert transform to extract its envelope. By applying the FFT, the envelope spectrum was obtained. In Figure (IV.3), the raw stator current signal and its corresponding envelope are presented, while Figure (IV.4) show of cases the envelope spectrums observed under different load conditions.

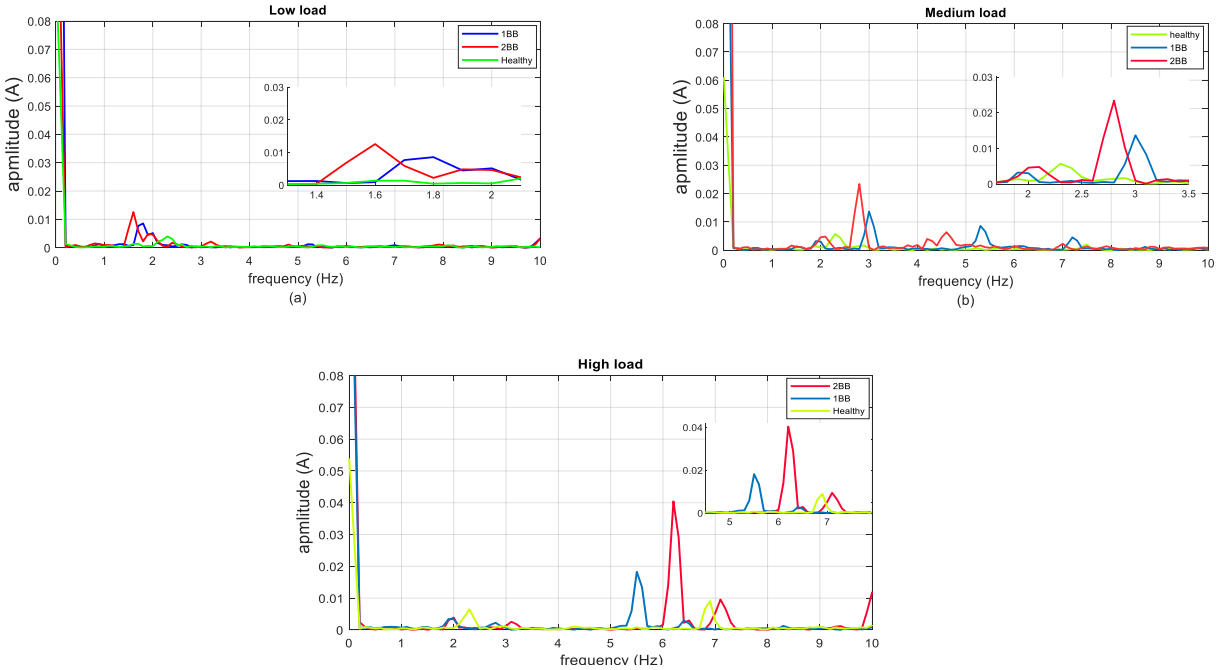


**Fig.IV.4** Spectrum of envelope under different load value

Analyzing the results, it becomes evident that the most significant amplitude components in the envelope spectrum were directly linked to the harmonics associated with broken rotor bars and DC components. We can also observe that even for the envelope state, the BRB harmonics still vary according to the load value. And their magnitude increase accordingly with both the load value and the fault severity. This problem will cause a data overlapping issue during the diagnosis. Therefore, there must be some kind of solution to solve this issue to separate them.

In the previous studies, the utilization of FFT is applicable only in the stationary signals. To overcome this limitation, an alternative method which use the discreet wavelet transform along with Hilbert transform is presented.

### IV.5.3 Analysis Based on Discreet Wavelet Transform on the envelope signal

In this section, we will explore the analysis of broken rotor bar faults by employing the Discrete Wavelet Transform (DWT) on the stator current envelope signal. Since the characteristics of the

broken rotor bar fault are typically concentrated in the low-frequency range, we can effectively extract this information by applying the discrete wavelet transform within the frequency band of [0 Hz; 10 Hz]. This frequency range is selected based on the envelope spectrum, utilizing the frequency decomposition presented in table 1 and shown in figure IV.5.

**Table.IV.1** Frequency decomposition for A9 and high order of DWT coefficients

| Wavelet decomposition | Frequency components (HZ) |
|---|---|
| A9 | [0, 9.76] |
| D8 | [19.53; 39.06] |
| D7 | [39.06; 78.12] |
| D5 | 156.25; 312.5] |
| D4 | [312.5; 625] |

Figure IV.5 present the DWT decomposition of the envelope (approximation and details) at medium load with two broken bars under medium load operating conditions.

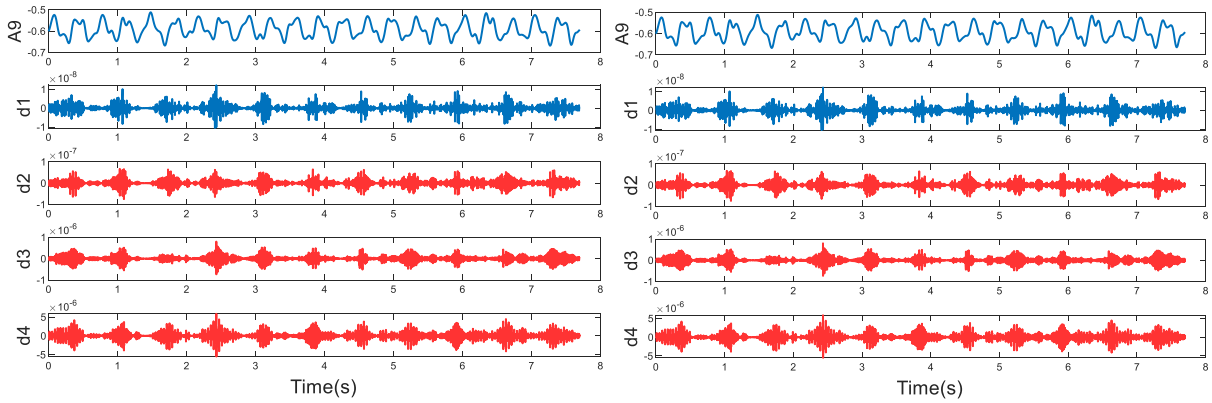


**Fig.IV.5.** The DWT decomposition of the envelope ( approximation and details) at medium load with two broken bars

Upon analyzing Figure IV.5, it becomes evident that the signals display observable oscillations, particularly in the approximation components (A9) and details (d6, d7, d8). These oscillations provide strong evidence of the presence of a defect. In our quest to locate the signal corresponding to the fault frequency (2sf), we meticulously examined the energy evolution of the approximation

signal (A9) and details (d6, d7, and d8) for various states: one broken bar, two broken bars, and the healthy state under different loads.

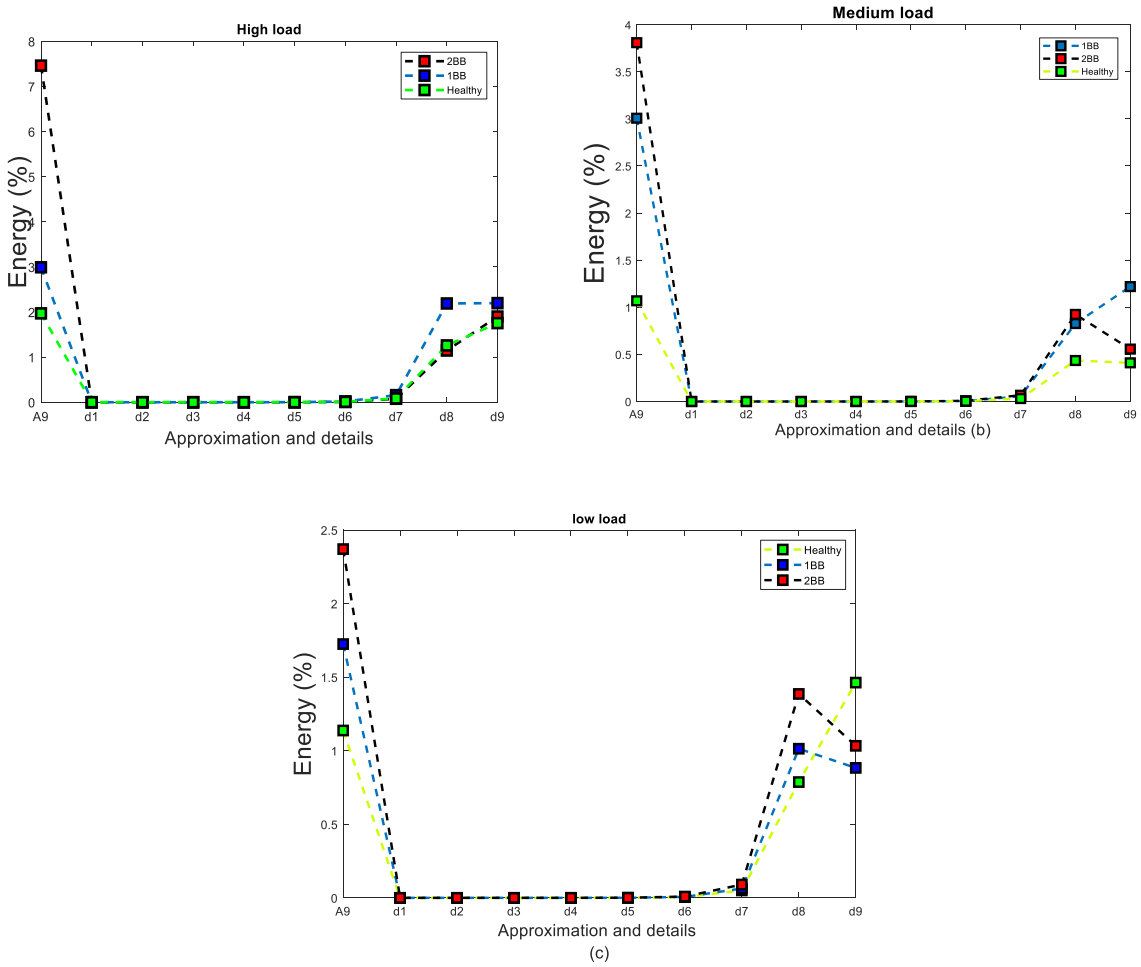


**Fig. IV.6** The evolution of the energy of the approximation and details signals for different fault severity under different rated load

According to these results, the most important energy are localized in (A9, d9, d8). However, there is no significant variation in the energy of (d1,d2,d3,d4,d5,d6,d7) which is remain quietly the same at any rated load in all states (healthy, one broken bar, two broken bars).Therefore, it cannot distinguish between healthy state or faulty state nor the rated load as well as for (d9,d8). Conversely, the energy of the approximation signal (A9) resulting from the 9-level decomposition shows a clear increase according the rated load and fault degree (healthy, one broken bar, two broken bars) which make it the ideal indictor for broken rotor bar fault under different load values. To further confirm this, the spectrum of the approximation signal (A9) and details (d6, d7, and d8) is presented in Figure IV.7. The analysis of these spectrums confirms that (A9) corresponds to the

fault signal at frequency (2fs). Therefore, (A9) can be effectively utilized as the fault diagnosis index during the feature selection step.

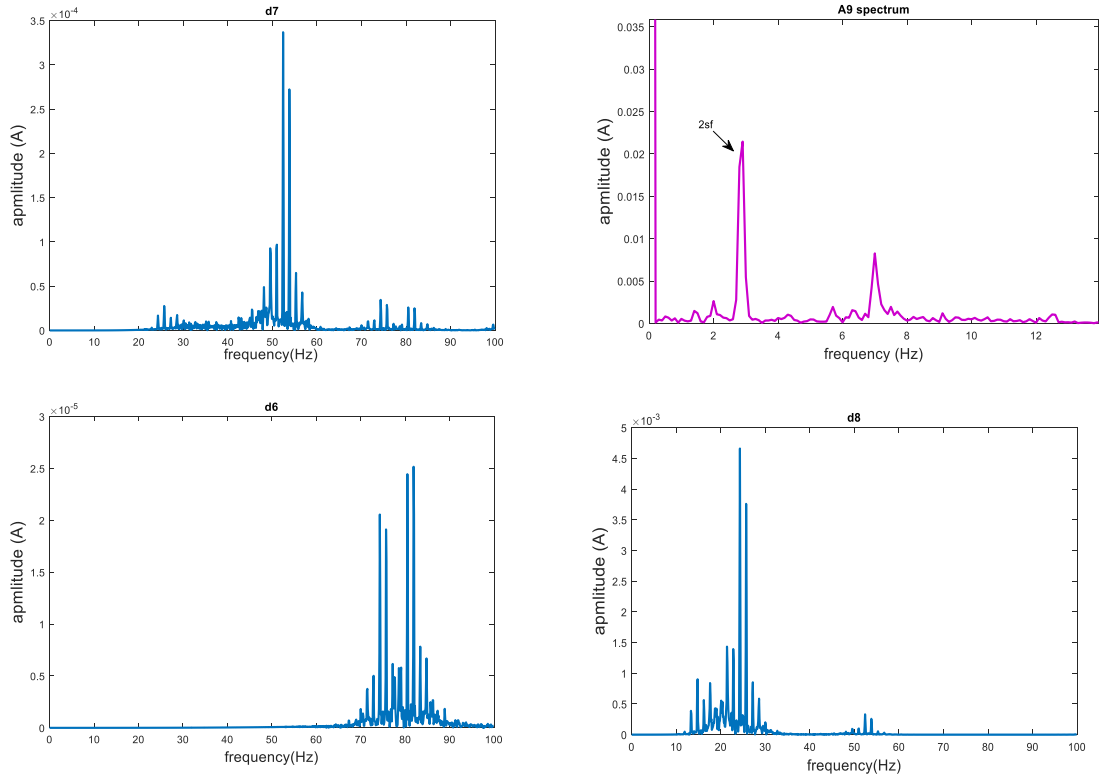


**Fig.IV.7** Spectrum of A9,d6,d7,d8 coefficients signals

- **Feature selection**

Feature selection emerges as a crucial step to enhance the performance of a detection system. In our study, we have identified the coefficient (A9) as a valuable characteristic feature, and its energy value is calculated using equation (IV.11):

$$CSD = \sqrt{\frac{1}{N_A}\sum_{i=1}^{N_A}(A_9(i))^2} \qquad \text{(IV.11)}$$

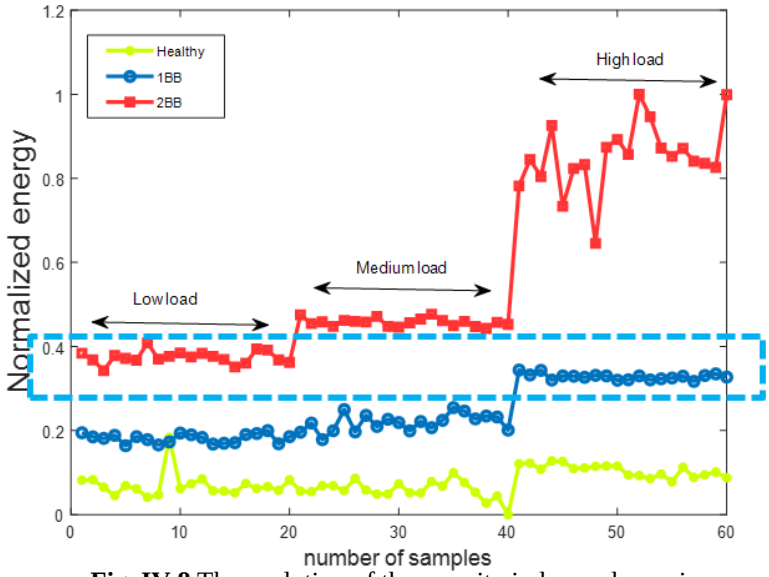


**Fig. IV.8** The evolution of the severity index under various

Figure IV.8 exhibits the evolution of the severity index resulting from equation (IV.11) under various loads and fault degrees. The results reveal that the severity index evolves in correlation with the fault degree and the load, making it a promising indicator. As the fault degree increases and the load effect is amplified, the severity index follows the same path. However, although the identified indicator is effective in differentiating healthy and faulty states, caution is necessary as it can potentially lead to false alarms. This concern arises from the presence of data overlap observed during our analysis, specifically between the machine operation under low load for two broken bars (depicted by red data) and high load for one broken bar (depicted by blue data). The overlapping data between these two cases may create a similarity effect giving the same value (0.4), making it challenging for analysts to distinguish between them. To ensure the accuracy and reliability of the fault diagnosis in the rotating machine system, it is crucial to address this data overlap issue and implement measures to minimize the risk of false alarms.

### IV.5.4 Analysis Based on Improved MUSIC

The Music technique known as is high resolution technique is vastly suited for BRB fault detection, as it was initially designed for the precise estimation and continuous tracking of spectral elements. Nonetheless, achieving accurate frequency estimation through the Music method necessitates a series of preliminary steps for signal enhancement. Specifically, these tasks involve data acquisition and filtering. Within this set of tasks, signal filtering emerges as particularly pivotal, directly influencing the overall quality of the results and therefore solving the overlapping data issue

### IV.5.4.1 Filtering

In this work, the primary purpose of filtering the stator current is twofold: first, to reduce the impact of noise, and second, to isolate the desired harmonics from unwanted spectral elements. To accomplish this, a narrow bandpass filter is designed and applied to the current signal after it has been acquired. This filter is created using the "fdesign.bandpass" function available in the Filter Design Toolbox of Matlab, and its parameters are carefully configured to exclusively allow the passage of the desired harmonics (figure IV.10). This approach is adopted because the Music method necessitates the examination of the signal within a narrow frequency band. As a result, there is no need to analyze the entire spectrum of the signal, as would be required by the Discrete Fourier Transform (DFT) method.

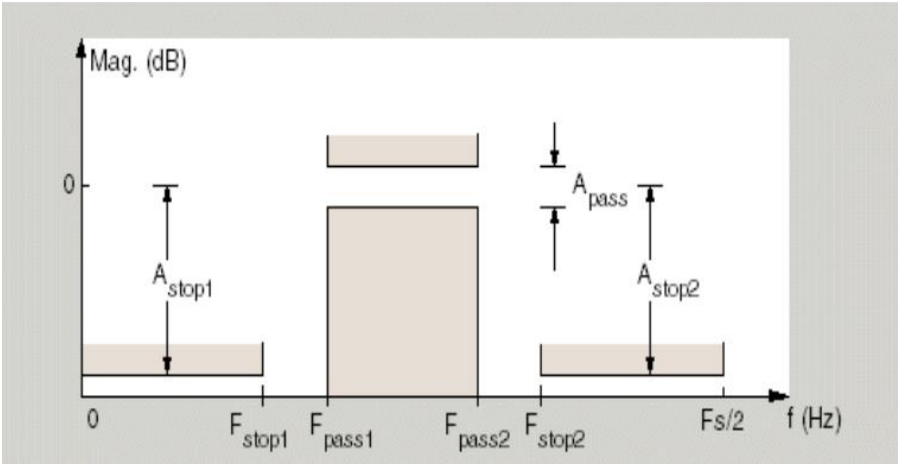


**Fig. IV.10** Design of Band-pass filter

### IV.5.4.2 Tracking amplitude and frequencies using TLS-Music

In the context of dynamic conditions, it becomes crucial to implement an automated tracking process to identify faults, such as broken rotor bars, in rotating machines operating under non-stationary signals. Although the high-resolution (MUSIC) method is effective for analyzing stationary signals, they often fail to detect faults under non-stationary conditions. To overcome this limitation, a Short Time Total Least Square Music's method (STTLS-Music) is proposed. This algorithm is inspired from short time Fourier transform (STFT) and take advantages of both MUSIC and STFT, utilizing an automatic tracking sliding short window to address the non-stationarity limitation and achieves high-resolution analysis with a reduced data measurements. In fact, the stator current is segmented into short time windows with overlapping regions, and each of these windows undergoes analysis using the STTLS-Music method, as illustrated in Figure IV.9. STTLS-Music is well suitable for the suggested fault diagnosis approach, due to its original design

to handle a limited number of data effectively. Unlike, the STFT, which requires a delicate compromise between time and frequency resolution. However, in practical applications, the MUSIC method often underestimates the number of sinusoidal components, thus potentially missing critical signals in the analyzed data. Additionally, this method tends to favor the detection of higher energy harmonics, which are not always the desired target harmonics with higher energy, which might not always be the desired target harmonics. To address these issues, preprocessing of the raw signal is essential. Filtering play pivotal role in enhancing result quality.

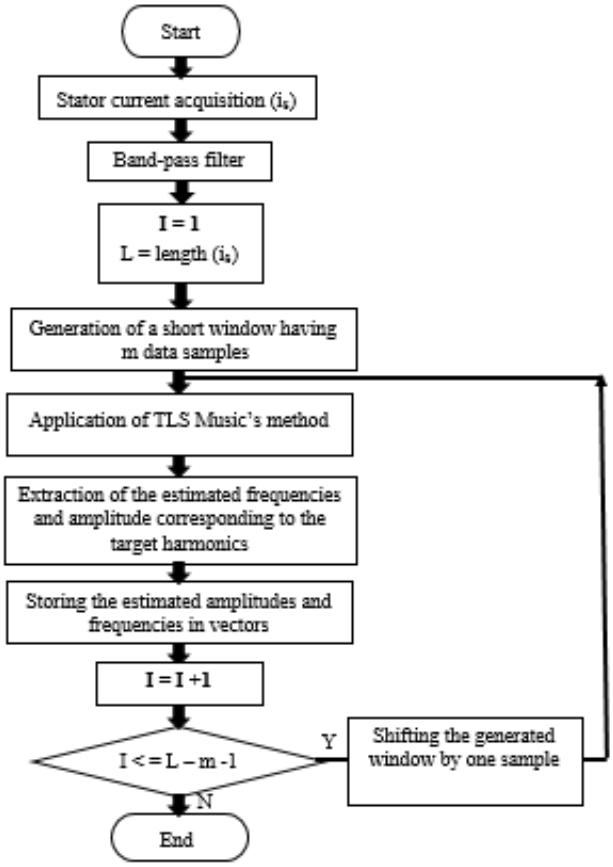


**Fig.IV.11** Flow chart of the STTLS –Music for an automatic tracking of the target harmonics for the amplitudes and frequencies estimation.

Preprocessing allows for noise elimination and extraction of the desired frequency range while discarding undesired spectral components and harmonics. The proposed method algorithm detailing can be found in figure IV.11, while its efficacy is assessed in both stable and non-stationary operational states as demonstrated further below.

### IV.5.4.3 Experimental results for stationary signals

In this section, the experimental evaluation of the motor's condition was conducted under stationary conditions at full load. To showcase the tracking capabilities of the STTLS-Music, the

stator current is segmented into numerous short overlapping time windows, each with a small size of 300 samples. The degree of overlap remains constant at 100 samples. Subsequently, each of these windows is subjected to analysis through the STTLS-Music method. Figure IV.12 and 13 display the three frequencies and the sideband amplitudes estimation results for healthy rotor and with two BRB respectively.

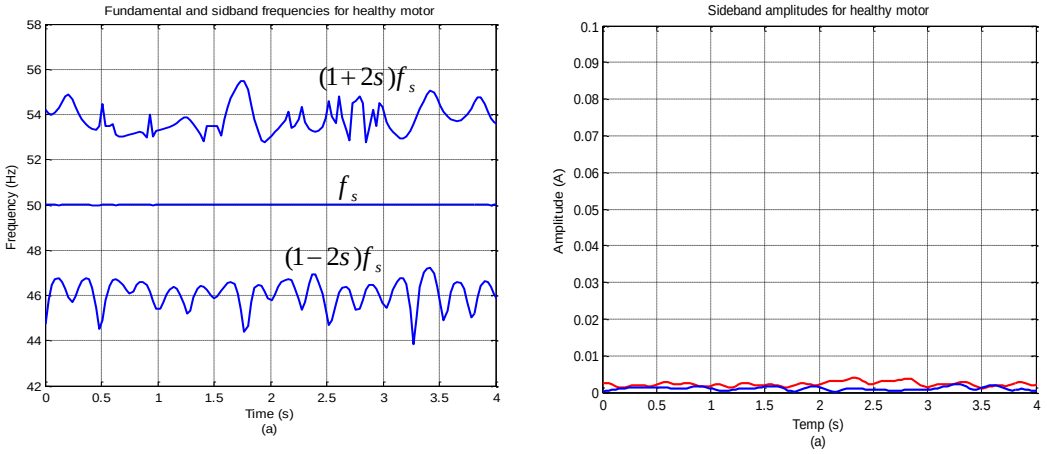


**Fig.IV. 12.** Experimental results: Frequency and amplitude tracking by the STTLS Music's method for healthy rotor a) Frequencies b) Sideband amplitudes

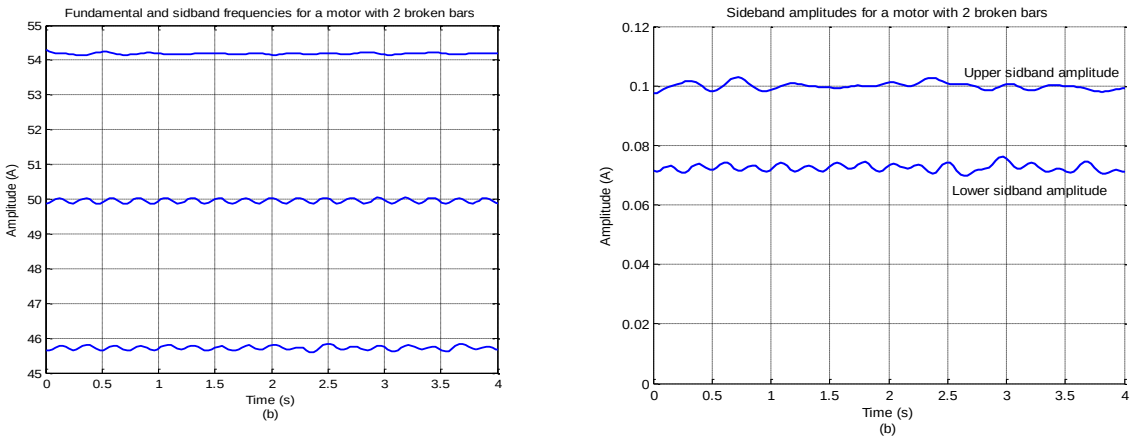


**Fig.IV. 13**. Experimental results: Frequency and amplitude tracking by the STTLS Music's method for rotor with two broken bars a) Frequencies b) Sideband amplitude

### IV.5.4.4 Experimental results for non-stationary signals

To assess the effectiveness of Short-Time-TLS Music in dynamic conditions, an experiment was conducted with the motor subjected to variable loads, inducing non-stationary behavior. The experimental findings illustrating this phenomenon are presented below. Initially, the motor operated with two broken rotor bars under a 3 Nm load, which was subsequently increased to 6 Nm after 3 seconds, while recording the stator current of induction motor. The time-domain representation of the stator current can be observed in Figure IV.14.

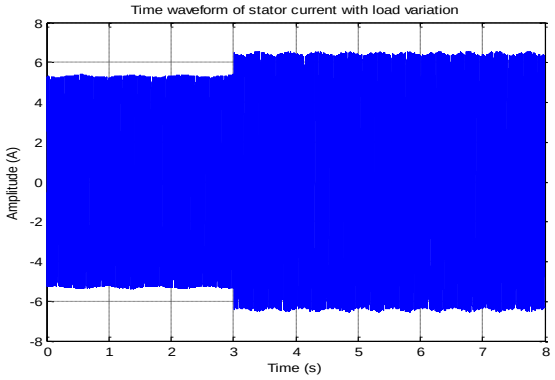


**Fig.IV.14** The time waveform of the stator current under non-steady conditions

Figure IV.15 shows that the upper sideband component moved away from the fundamental frequency after the load variation, and, at the same time, the amplitudes of the three components (fundamental and the two sideband component) increase approximatively from 0.011 A to 0.046A for the lower sideband component and from 0.025 A to 0.05A for the upper sideband component, (Fig. IV.16).The sudden variation of the load produces also an increase on the fundamental component amplitude from 4.8 A to 5.75 A, while the main frequency remains constant since there is no change on the supply frequency. These results demonstrate the usefulness of the STTLS-Music method, as it does not only allow an effective detection of the fault but also the extraction of additional important information from the motor signals at different operating conditions.

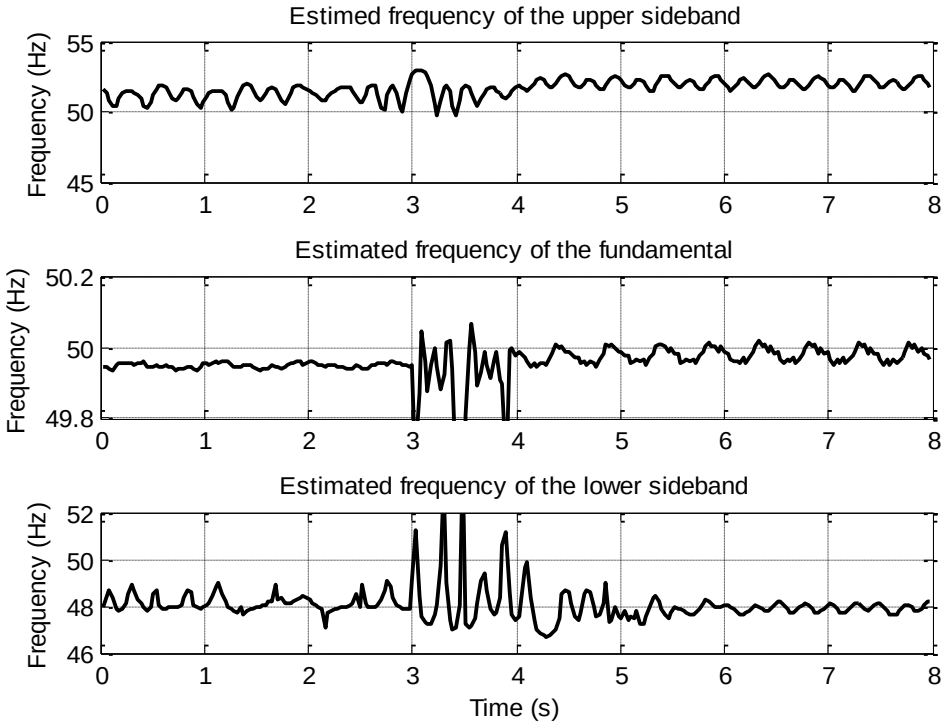


**Fig.IV.15** The frequency tracking for a faulty motor with a sudden load variation occurred at t=3 s

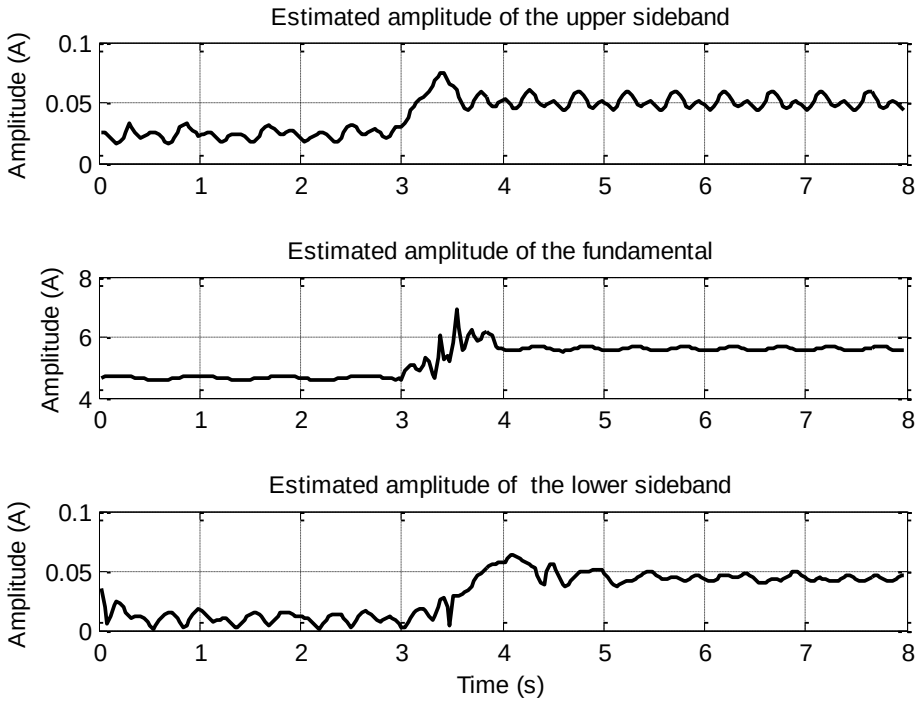


**Fig.IV.16** The amplitude tracking for a faulty motor with a sudden load variation occurred at t=3 s

## IV.6 Classification of BRB fault using ANN

In this section, we propose the architecture of the intelligent application capable of detecting the fault using a supervised classification technique based on the algorithm Music combined with MLP type ANN. Figure IV.9 shows that the diagnosis process consists of three steps: data preprocessing, feature extraction and, fault diagnosis using Neural Networks.

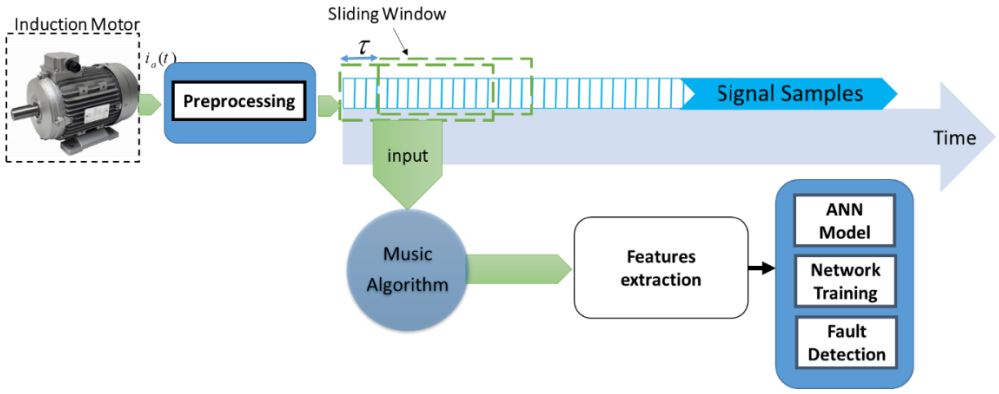


**Fig.IV.9** Methodology for fault detection and diagnosis using Music and ANN.

The concept revolves around identifying the fundamental and the two BRB frequency and subsequently deriving their amplitudes, which are used as ANN inputs.

### IV.6.1 Features extraction

In fact, the detection of a single faulty bar is largely sufficient for the diagnosis. However, the estimation of the number of broken bars is very important information that gives an idea of the extent of the rotor defect, and therefore helps maintenance experts in decision-making. In this work, our choice is based on the use of a new criterion that represent the sum of the sideband amplitudes of the BRB component as a fault indicators in the feature selection. The figure IV.17 (a) represents the evolution of the normalized value of this indicator according to the load and the severity of the

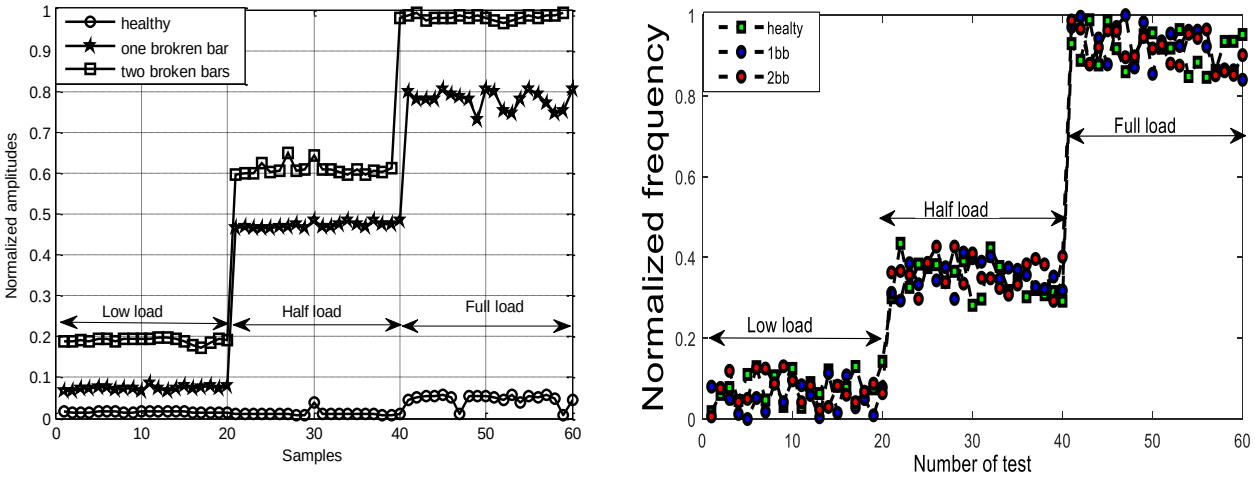


(a) (b)

**Fig. IV.17** Normalized features: (a) Normalized criterion (b) Normalized fundamental Amplitude

fault. It is clear that this indicator can discern between the healthy state and the defective state. Also, for a given load, it can discern between a broken faults of one or two bars. Nevertheless, an overlapping issue still occur for the case of one broken bar at low load and the healthy state at high load levels. Consequently, another criteria must be added to solve this problem for a reliable diagnosis. To overcome this problem, the fundamental amplitude is adopted as discriminate criterion. Figure IV.17 (b) displays the progression of the normalized values for the two features. It is evident that the first feature responds to both the fault severity and load variations, while the second feature primarily reacts to load variations alone.

### IV.6.2 Classification Based on ANN

Feature classification via Artificial Neural Networks (ANNs) is a common and powerful approach in machine learning and pattern recognition. ANNs are inspired by the human brains neural

structure, and they can be used for various tasks, including fault diagnosis. In our work, the neural network is invited to confirm, after each acquired data, the motor state (healthy or defective). Here is a general overview of how feature classification using ANNs works:

1. **Feature representation and data preparation:** the features extracted from the input data are fed into the input layer of the neural network. These features were prepared and then normalized in feature extraction and selection stages respectively.
2. **Network Architecture**: Design the architecture of the neural network. This includes specifying the number of layers, the number of neurons in each layer, the activation functions, and the type of connections between neurons. In this study, the selected ANN architecture is presented in Fig.IV.18. It is a feedforward multi-layer perceptron (MLP) composed by two inputs, the selected criterion and the fundamental amplitude, which are used to improve the reliability of the classification, and one output, which represent the state of the rotor, gives zero for the healthy machine, 0.5 for the case of one BRB and 1 for the case of two BRB. The “sigmoid" is the activation function of hidden and output layers
3. **Training**: Training an MLP involves adjusting the weights and biases of the connections between neurons to minimize a certain loss function (error), typically through an optimization process. In this study, backpropagation algorithm was chosen to train the ANN MLP
4. **Decision**: The output from the network is used to make a decision about the class or category of the input features.

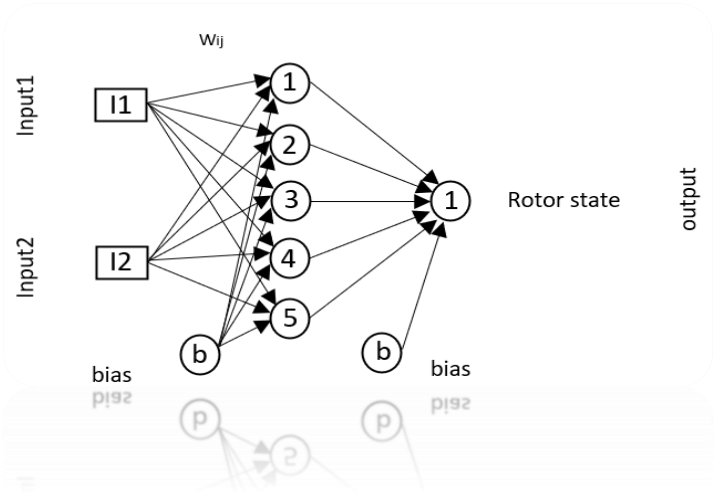


**Fig. IV.18.** Architecture of the used ANN classifier

### IV.6.3 k-cross validation

Stratified K-fold cross validation is a vital statistical technique employed in the assessment of machine learning models, especially when confronted with limited data, to prevent overfitting and fine-tune model parameters. This approach is grounded in the division of the data into k subsets of equal size or nearly so [CHA 23]. During each iteration, one subset serves as the validation set (testing data), and the remaining (k-1) subsets collectively contribute to training the model. The training and validation process is iterated k times, resulting in a comprehensive evaluation. Refer to Figure IV.19 for a visual depiction of the data segmentation in four cross-validation methods.

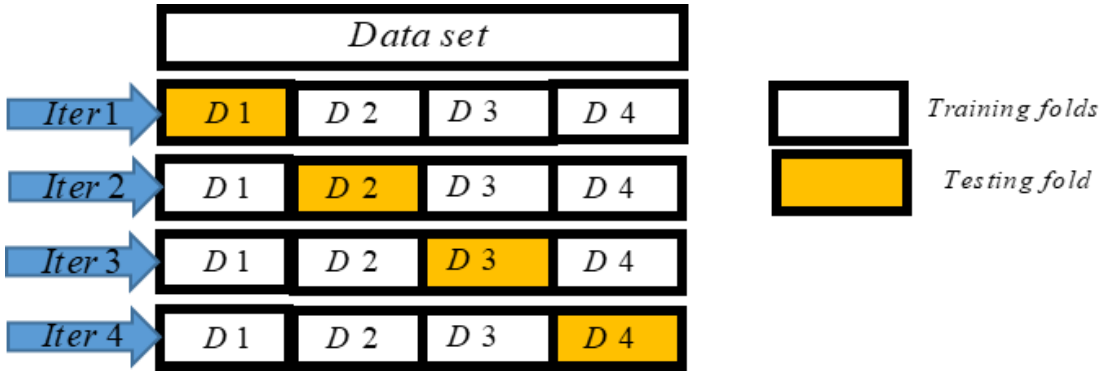


**Fig. IV.19.** Four folds cross validation method

### *IV.6.4 Evaluation Metrics*

In order to verify the accuracy of the proposed ANN methods to obtain the best appropriate model for BRB classification fault. Each model performance was quantified individually in the aim to compute its accuracy depending of the error. However, three statistical error rates was used, which is the mean square error (MSE), root mean squared error (RMSE) and the mean absolute error (MAE). These metrics were computed as described below:

$$MSE = \frac{1}{N}\sum_{i=1}^{N}(S_i - y_i)^2 \tag{IV.12}$$

$$RMSE = \sqrt{\frac{1}{N}\sum_{i=1}^{N}(S_i - y_i)^2} \tag{IV.13}$$

$$MAE = \frac{1}{N}\sum_{i=1}^{N}|S_i - y_i| \tag{IV.14}$$

### *IV.6.5 Results and discussion*

The selected MLP composed of two inputs, where the associated data is chosen carefully to improve the reliability of the classification as it discussed previously. In addition, it is consisted of one output, which represent the state of the rotor, where zero denote to the healthy state, 1 for one broken bar faulty state and 2 for two BRBs. For this purpose, a normalization treatment was applied to the collected experimental data to be then integrated into the training process. This database contains different collection of examples that cover the motor state (healthy or defective) under different load conditions (20%, 50% and 90% of the rated load). Fig. IV.20 shows the normalized used database. It is composed by two input databases Fig.IV.19 (a) and (b) as well as its corresponding target output database. The input database contain 60 examples for the healthy state and 120 examples for the faulty state, which the latter is divided into two sequences of 60

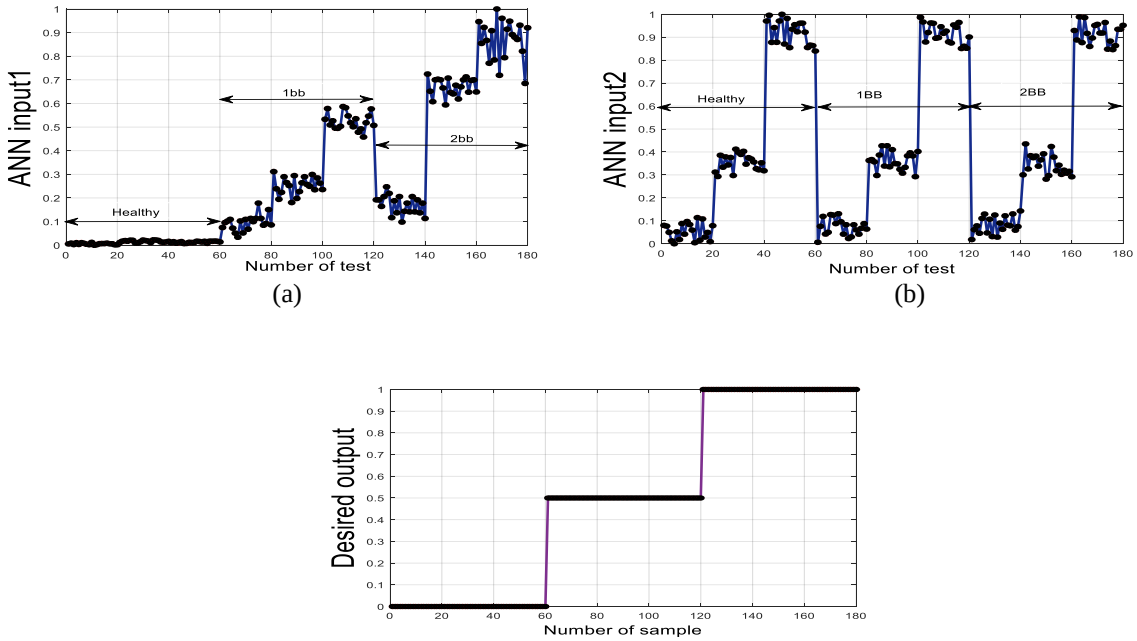


**Fig. IV.20** The used database

examples for one BRB and two BRBs respectively. During the training, 5-Fold cross validation technique was applied to prevent the overfitting issue and therefore improving the learning process.

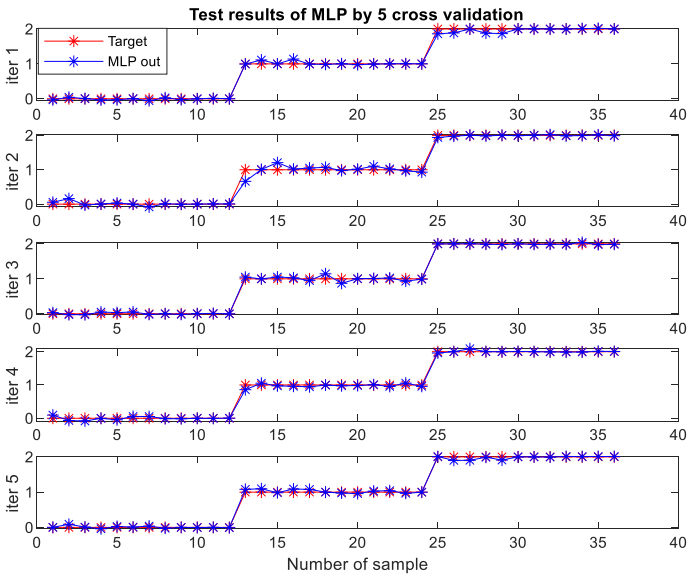


**Fig. IV.21** The test results of MLP for 5 cross validation

In fact, five sequences were repeated where in each one, 180 samples of this data was divided into 5 folds with 36 samples (Fig IV.21). However, one fold is reserved as testing dataset and the remaining four folds were selected as the training dataset validation. As it shown, the ANN has well learned the inputs data and has correctly reproduced the desired output. In addition, the ANN models has the ability to distinguish correctly between the healthy and faulty operating and it is capable to identify the fault severity without falling into data overlapping issue resulted from the load variation**.** In order to verify the accuracy of the proposed ANN method, three statistical error rates was used, which is the mean square error (MSE), root mean squared error (RMSE) and the mean absolute error (MAE), given by: Table IV.2 presents the error rate metrics evaluation results of the cross validation method for K=5 and k=10 for the testing phase. According to these results, it is clear that the MLP model provides a good results that is not too far from ENN model.

Table.IV.2 Metric evaluation

| Evaluation metric | FFNN K = 5 | FFNN K = 10 |
|---|---|---|
| MSE | 0.0040 | 0.0091 |
| RMSE | 0.0632 | 0.0952 |
| MAE | 0.0451 | 0.0556 |

## IV.7 Conclusion

This work has introduced an accurate and robust approach for early detecting and localizing of broken rotor bar fault automatically in the induction motor using a new indicator based on the STTLS-MUSIC combined with Artificial neural networks. First, various approaches were exposed and was validated by the experimental results where the main outcome can be summarized as following: The first approach is successful in detecting and locating the broken rotor bar fault under stable conditions. Although this method gives high resolution analysis of BRB sideband frequencies, while it clearly fails when the load is at a very low level. In this case, the two BRB sideband harmonics are so close to the fundamental that their detection is much more difficult. To overcome the last drawback, the second approach use the Hilbert transform method to extract the signal diagnostic without the presence of the fundamental. Nevertheless, these techniques exhibit optimal performance only when applied to signals with unchanging statistical properties over time. DWT are particularly useful for analyzing non-stationary signals because they provide both time and frequency localization. However, the fault indicator derived from this method can result in false alarms due to data overlap.

To overcome the mentioned limitation, our proposed approach has been created to identify and locate the BRB faults, even when the conditions are non-stationary. We address the issue of overlapping data by employing an artificial neural network. We utilize the STTLS-Music technique to extract relevant features for BRB fault classification. The statistical evaluation metrics demonstrate that the MLP model is well-suited for fault classification, achieving a good level of accuracy.

# Chapter 5

# Diagnostic of airgap eccentricity and ITSC by CNN

## V.1 Introduction

Due to the swift advancement of the manufacturing industry, the importance of machine fault diagnosis has grown substantially to guarantee the secure functioning of equipment and production processes. As a result, various methods have been investigated and refined over the previous years, with a notable rapid progression in intelligent algorithms. Among these approaches, the convolutional neural network stands out as a prime example of intelligent diagnostic models. Over the past five years, it has been extensively investigated and employed [JIN 20]. In this context, this chapter introduces a contribution, which aims to create two automated fault diagnosis based on conventional neural network models. The first one is dedicated to detect and classify air-gap eccentricity fault. The second is directed to diagnose the inter turn short circuit (ITSC) fault. These system are capable to classify precisely various type of faults by utilizing specified images.

This research is organized as follows: Section 2 analyzes previous work and presents our contribution. The proposed method is presented in section 3 involves data description, Encoding time-series signal into image, the construction map, and the proposed CNN model. Section 4 shows experimental results for airgap eccentricity fault. Sections 5 and 6 represent data description and experimental results for ITSC fault. Finally conclusion is drawn in section 7.

## V.2 Motivation

Mechanical failures in electrical machinery stand as the most prevalent, accounting for as much as 60% of all other defects. Among these, air gap eccentricity emerges as a frequent issue within the realm of mechanical faults. This defect typically arises due to factors such as bearing wear, shaft misalignment, load unbalance, or rotor deviation. When air gap eccentricity occurs, the motor generates oscillations in the electromagnetic torque (resulting in unbalanced magnetic pul), which diminishing productivity and potentially leading to friction between the rotor and stator. This friction-related wear then contributes to the degradation of insulation material, increasing the likelihood of inter-turn short circuit faults occurring in the stator coils. Consequently, the early diagnosis of eccentricity faults becomes crucial in curbing the emergence of other fault types [ZHI 22]. Data mining (DM) methodologies have demonstrated their effectiveness in handling scenarios characterized by intricacy, as evidenced by their successful application in diverse contexts. Machine learning-based techniques, serving as a prime example of data-driven strategies, has exhibited significant dynamism and success within the evolution of contemporary industrial sectors. This is particularly evident in the era of deep learning.

Over the past years, classical machine learning models, like support vector machines (SVM) and k-nearest neighbors have made notable advancements in recent years, certain limitations persist when confronted with the escalating demands of the industrial landscape. To illustrate, (i) these methods often necessitate manual feature extraction and selection, a constraint that proves inadequate in the realm of complex big data analysis. Additionally, effectively exploring high-dimensional features becomes challenging due to the inherent shallowness of their structure; (ii) the design of feature extraction and decision-making processes occurs independently, leading to a lack of synchronized optimization that results in significant time consumption and performance constraints; (iii) in the face of the growing diversity of sensors and machine complexity, coupled with the expanding volume of data characterized by increased dimensions and dynamics, traditional algorithms struggle to deliver satisfactory diagnostic outcomes [JID 20]. Deep learning (DL) algorithms have exhibited exceptional capabilities in the realm of image recognition and speech processing, surpassing human performance in numerous applications. Over the last half-decade, deep learning has also ignited the surge of intelligent fault diagnosis. Among these methodologies, the convolutional network [LAN 16] has taken the forefront as the leading architectural choice, showcasing cutting-edge performance across various domains. The conventional neural network founded fault diagnosis framework can be commonly recapitulated into three key phases, as depicted in Fig. 1: data collection, model construction, and the process of feature learning and decision making.

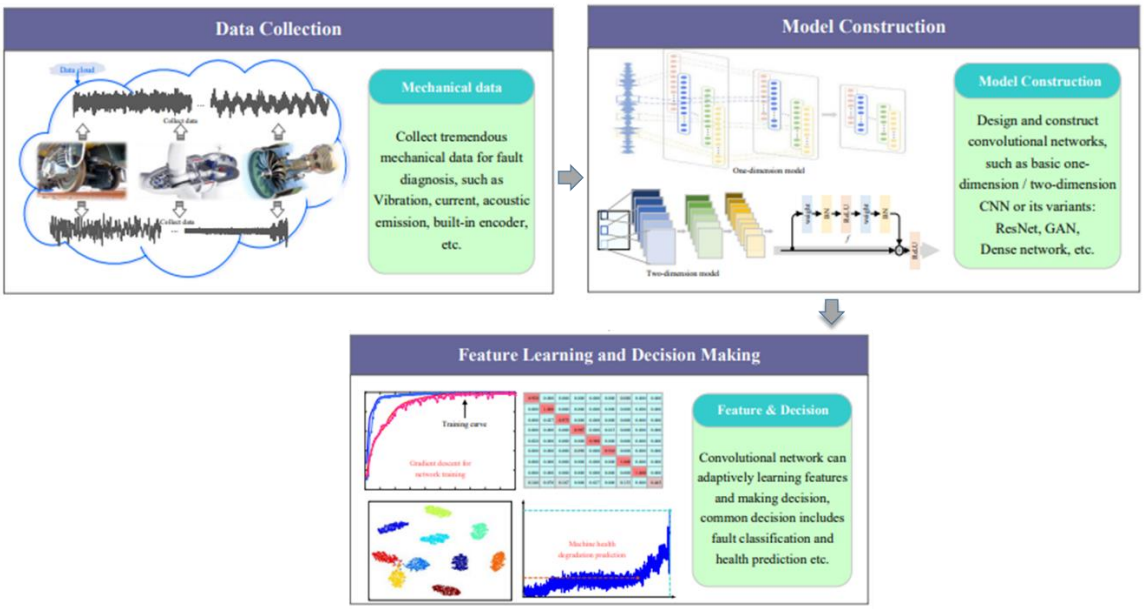


**Fig. V.1** Conventional neural network fault diagnosis framework [JID 20]

Several Convectional Neural Network (CNN) structures find application in fault classification literature, including: deep auto-encoder [LI 20, JIA 20] deep belief network [TAO 16; HUI 22a, HUI 22b], recurrent neural network [QIA 20; ZHU 2022;], and convolutional neural network (CNN) [DING 17, WAN 23], deep transfer learning [CHU 20, IMA 23]. The fundamental concept behind transfer learning (TL) involves utilizing a model that has been trained on a specific source task and repurposing it for a different target task. These results serve as inspiration for us to employ the fusion of these resilient techniques in order to create accurate diagnostic system for airgap eccentricity and inter-turn short circuit faults classification.

**Case study 1: diagnostic of airgap eccentricity using VMD and CNN**

## V.3 Proposed method

Taking into account multiple health states of motors across diverse operational conditions, the proposed method introduces an intelligent approach for diagnosing airgap faults. This method combines Variational Mode Decomposition (VMD) with a deep learning model. The structure of the suggested airgap diagnostic method is depicted in Figure V.2, encompassing two primary components: image construction and the proposed Convolutional Neural Network (CNN) model.

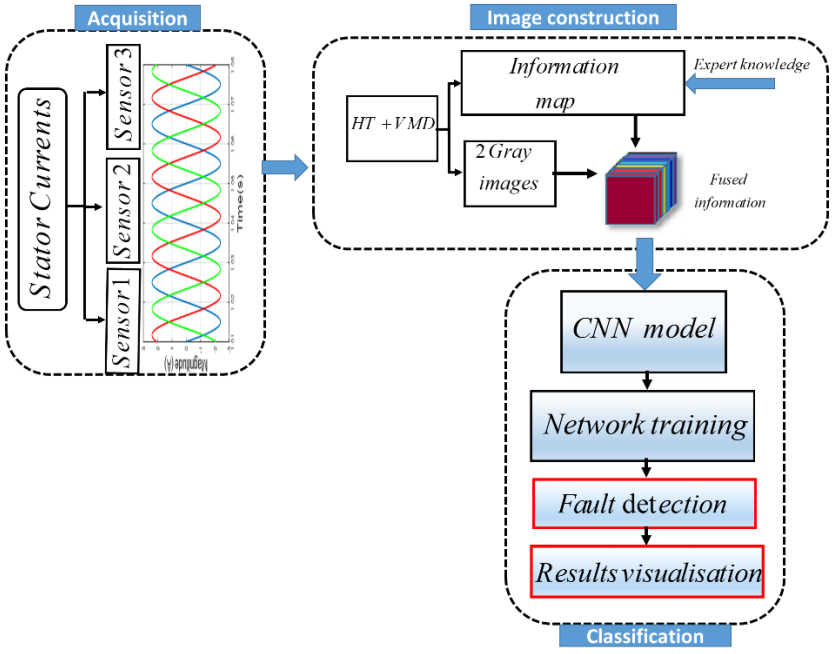


**Fig. V.2** The global structure of the proposed method

In conventional fault diagnosis techniques, accurately classifying the nature of a fault and determining its severity often demands significant expertise and experience in both data preprocessing and feature extraction. Moreover, the challenge lies in extracting optimal features

from a dynamic environment [Wan 19]. However, when the classifier encounters new information, such as variations in fault severity not encountered before, it can pose challenges. It might encounter difficulties in properly categorizing it. Hence, a Deep Learning (DL) model linked to a distinct combined input is introduced to effectively classify and diagnose air gap eccentricity faults. This specific fused input data encapsulates pertinent information that enhances the CNN model's generalization capability and aids in reducing computation time. The details of the proposed method are provided in the following sections.

### V.3.1 Data description

To evaluate the efficiency of our diagnostic approach, we apply the proposed model to experimental data encompassing various instances of airgap faults, and under diverse motor operating conditions. The used experimental test rig is shown in annex.

### V.3.2 Analysis Based on Variational mode decomposition (VMD)

In this section, we will explore the analysis of air-gap faults by employing the Variational mode decomposition (VMD). In fact, the obtained IMFS are presented in figure V.4, which are the segmented portions of the signal, encapsulate pertinent feature information.

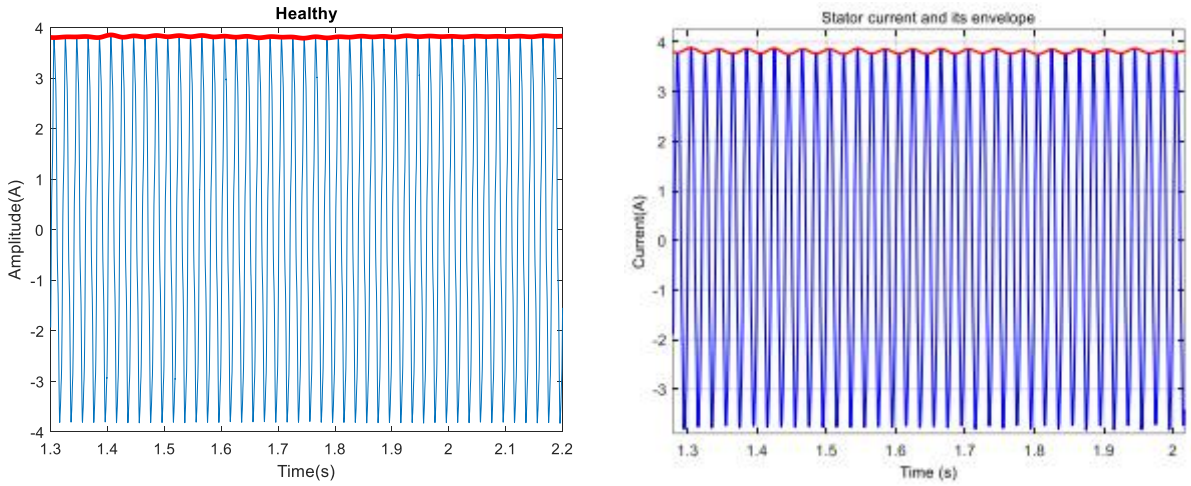


**Fig. V.** 3 Stator current and its envelope

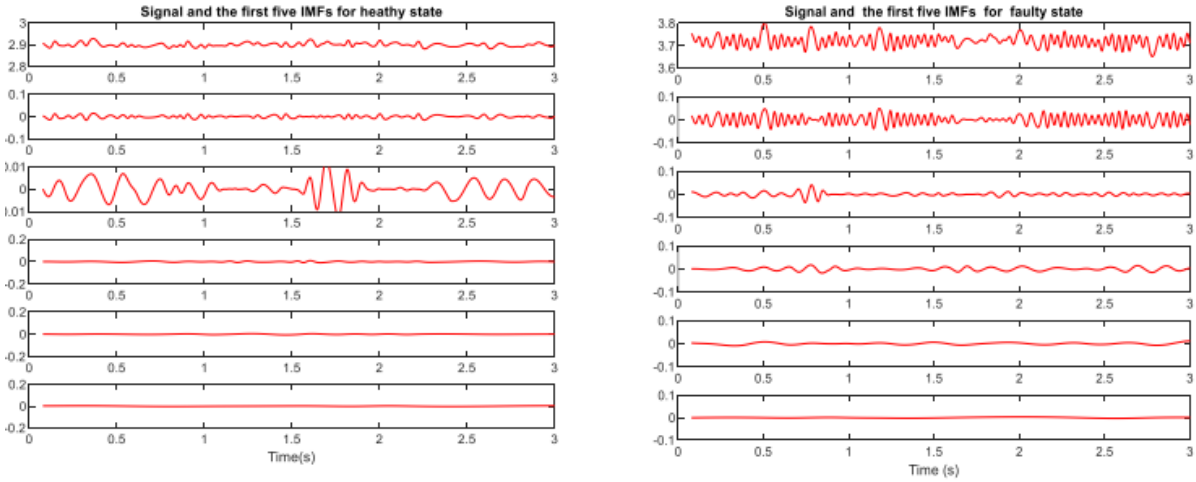


**Fig. V.4** Resulted IMFs at healthy state (left) with airgap eccentricity of 3% degree (right).

### V.3.3 Encoding time-series signal into image

In practical application, a predominance of the signals, such as stator current signals, frequently exhibit non-stationarity and contain abundant information irrelevant to fault diagnosis. Fortunately, the distinctive attribute of the DL model lies in its capability to effectively handle exceedingly intricate and nonlinear signals. This is made achievable by its convolutional layers, which function like filters (e.g., high-pass, pass, bandpass, or low pass filters). Thus, this means that the CNN is able to extract robust and identifiable features from a higher dimensional structure, such as 2D/3D images.

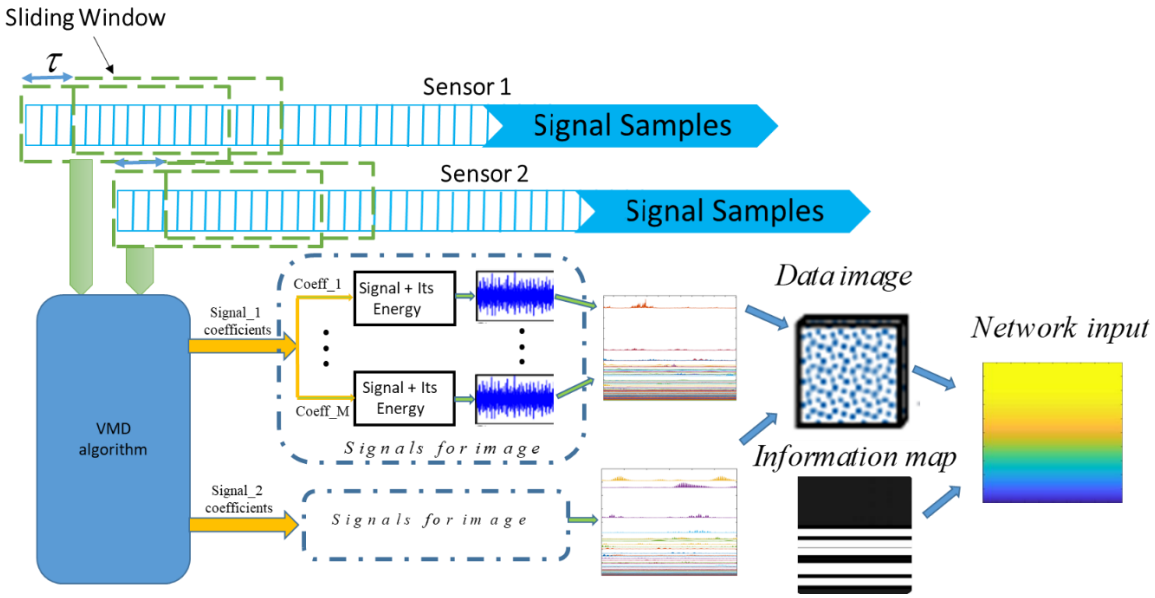


**Fig. V.5** Flow chart conversion of time-series signal to image

Usually, the time-series such as current, voltage and vibration signals are transformed into image aims to reveal fault-related features and patterns that might remain hidden in the original time-series signals. Current image transformation techniques can be categorized into three groups according to their approaches: arraying [Guo 16], coloring [Ma 09], and coordinate transformation [FAH 21]. In the array-based transformation, data is divided into vectors of equal sizes, arranged in a matrix, and subsequently mapped to an image. The coloring-based image transformation method involves a mapping of raw data to the corresponding color field, which operates in a one-to-many manner. The image transformation technique relying on coordinate transformation transforms a certain feature type into an alternative coordinate system, facilitating a more conspicuous differentiation of feature distributions through visual observation. However, these transformations lack a stringent logical foundation. In this work, a novel technique is proposed to create input CNN input. This image is generated through the fusion of data images and the knowledge map, as depicted in Figure V.5. An overlapping sliding window approach of length M is implemented to segment the stator phase current data into N segments. Subsequently, a set of 2D sample data is derived by applying the VMD transformations to each segment.

Taking advantage of this insight, the creation of the 2D data matrix involves utilizing both the sub-signals of the IMFs and their corresponding energy values, which can be computed as follows:

$$E_i = \sum_{n=1}^{M} [U_i(n)]^2, i = 1, 2...N \tag{V.1}$$

where, Ui signifies the IMF signal, with M representing the signal length and N denoting the number of modes. By leveraging both the energy content of the IMFs and their corresponding signals, the matrix is formed. In this study, the resultant data matrix assumes dimensions of (MxN) and is referred to as "combined energy IMF and signal" (CEIMS). Its construction unfolds as follows:

$$CEIMS\big|_{i,j}^{\tau} = E_i + U_{i,j}^2; \tag{V.2}$$
$$i = 1, 2..., N, \; j = 1, 2..., M$$

The ith vector within the CEIMS matrix is established as follows:

$$CEIMS_i = [y_i(1), y_i(1), ..., y_i(N)] \tag{V.3}$$

where:

$$y_i(j) = E_i + U_i^2(j) \tag{V.4}$$

Corresponding to equation (V.2), for each time delay τ, a CEIMS matrix is generated to portray the alterations in energy across the diverse resulted sub-signals. In this situation, the dynamic arrangement of frequency distribution can be translated into a CEIMS matrix, capable of accommodating essential feature descriptors. This transformation leads to a reduction in the computational complexity linked with texture-based fault analysis. Ultimately, each original signal contributes to the formation of a 2D data image with dimensions of M×N. The values within the CEIMS matrix are scaled to fit the range of 0 to 255, which directly corresponds to pixel intensity values located at coordinate points (i, j) in the grayscale image. By designating CEIMS (i, j) as the energy value, the pixel intensity of the image at the specific coordinates (i, j), where i and j are both within the range [1, M], can be succinctly expressed as:

$$CEIMS(i,j) = round\left\{\frac{255}{I_{\max} - I_{\min}}\left[CEIMS(i,j) - I_m\right]\right\} \tag{V.5}$$

With $I_{max}$ and $I_{min}$ denote the highest and lowest energy values within the IMFs, while round (·) signifies the rounding function.

### V.3.3 Construction of the information map

An information map (IM) serves as a visual depiction that effectively arranges data or information in a coherent manner. It acts as a valuable instrument for effectively displaying expert domain knowledge pertinent to a specific discipline or field. This knowledge encompasses a range of aspects, including fault characteristics, operational conditions, and diagnostic rules drawn from historical monitoring data [WOO 18]. Within the context of air gap eccentricity fault diagnosis, a significant type of domain knowledge is the frequency of eccentricity fault characteristics frequency (EFCF). It can be expressed as follows:

$$f_{exc} = fs \pm kf_r \tag{V.6}$$

(V.6) can be rewritten as follow:

$$f_{exc} = \frac{1}{1-g} f_r \pm kf_r = k_{EFCF} f_r \tag{V.7}$$

With:

$$k_{EFCF} = \frac{1}{1-g} \pm k = f_r, k = 1,2,..$$

It is evident that the computation of EFCF is possible when the shaft speed and slip variable are accessible. However, it is widely recognized that the harmonics associated with air gap eccentricity faults is situated in the low-frequency band. In order to reinforce the effectiveness of Deep Learning for air-gap eccentricity fault diagnosis, an information map (IM) is built to incorporate domain knowledge into the CNN input. In order to maintain the consistency of the information map data format with the resultant data images, diverse operating conditions are employed, each represented by varying grayscale intensities. Initially, the information map is established as an empty matrix sized M × M. Subsequently, the foundation background of the information map is defined by representing the operating condition information through gray levels $y_{ij}$, given by:

$$y_{ij} = \Delta f_r \tag{V.8}$$

Where $y_{ij}$ represents the gray value at the coordinate (i, j), and Δfr signifies the discretized rotating speeds. The fundamental steps for incorporating domain knowledge into the information map can be encapsulated as follows:

1. Stator currents were collected using multiple sensors and sampled at a frequency of 10 kHz, across various operating conditions that encompassed the recording of load and speed variations.
2. Extraction of the stator current envelope (SCE) signals.
3. Decompose the SCE signal into a series of sub-signals utilizing Variational Mode Decomposition (VMD).
4. Compute the correlation coefficients, as described in equation (V.10), between the derived decomposed signals and the synthetic signals defined as follows:

$$S_i(t) = A_i \sin(2\pi k_{FCF_i} f_r t) \tag{V.9}$$

$$r_{S,U_I} = \left| \frac{\sum_{i=1}^{M} \left(S - \bar{S}\right)\left(U - \bar{U}_i\right)}{\sigma_S \sigma_{U_i}} \right| \tag{V.10}$$

5 Subject to a predefined threshold, the signals verified the criteria are selected for the construction of the information map at the specified coordinates:

$$i_{FCF_d} = round\left( i_{fr} \frac{k_{FCF_d} \Delta f_r}{\Delta f_{FCF}} \right) \tag{V.11}$$

Where $\Delta f_{FCF,}$ ifr symbolize the discretization step of the EFCFs and the horizontal coordinates of the EFCF

Finally, the acquired information map is combined with the data images to form the input network. Subsequently, the created image is resized to dimensions of (227x227x3). Figure 6 illustrates the images pertaining to both healthy and three distinct types of faulty states.

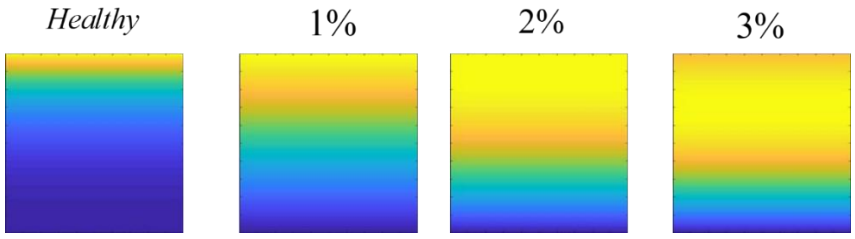


**Fig. V.6** The obtained input images representing healthy and faulty states.

### V.3.4 Proposed modified model

In recent times, a significant part of the research effort has been devoted to the development of lightweight models that meet diagnostic needs in the constrained conditions. . Notably, there has been a proliferation of contemporary strategies for crafting lightweight models that strike an optimal balance between speed and accuracy. Examples of such approaches include MobileNet, SqueezeNet, and ShuffleNet, which exhibit superior performance in terms of parameter efficiency and accuracy when compared to more resource-intensive models like ResNet [ZHAN 20]. This trend has also led to increased interest in integrating lightweight CNN architectures into various applications.

However, despite the compact design of lightweight neural networks, there remains considerable room for improvement in terms of their accuracy. This is especially true for real-time fault diagnosis tasks where achieving both high accuracy and fast processing is of paramount importance. To meet this challenge, our approach is inspired by two sources: on the one hand, the remarkable efficiency demonstrated by the Fire modules within the framework of SqueezeNet; and second, the adaptive capability of the variational mode decomposition (VMD) technique. This strategy is complemented by the incorporation of an attention block mechanism, complemented by a strategy modification that significantly improves detection accuracy without imposing excessive computational overhead.

SqueezNet stands out as a lightweight model, managing to attain a level of accuracy akin to that of AlexNet while operating with a mere 1/50th of the parameter count. Its architecture revolves around a straightforward configuration known as the Fire module, encompassing both the squeeze and expand layers. The squeeze layer is characterized by its reliance on 1 × 1 convolution filters,

leading to a remarkable reduction of parameters by a factor of nine compared to the use of 3 × 3 convolution filters. The expand layer, on the other hand, employs a blend of 1 × 1 and 3 × 3 filters. The overarching structure of SqueezNet is comprised of nine fire modules.


**Fig. V.7** The Improved Version of proposed SqueezeNet

This study employs a transfer learning approach founded upon an adapted SqueezNet model, complemented by an attention block, to facilitate airgap detection and classification. The customized SqueezNet model in question is characterized by a reduction to five fire modules instead of the original nine. To enhance training efficiency, the initial ReLU activation in the base model is substituted with a leaky ReLU activation. Additionally, the terminal convolutional layer within the SqueezNet architecture undergoes substitution with a new layer, purposefully tailored to suit our classification task. Furthermore, a novel coordinate attention mechanism is introduced, entailing the removal of the dropout layer in favor of batch normalization, while simultaneously incorporating global considerations. After the concatenation layer within the attention mechanism block, an average pooling operation was positioned. This can be visualized in Figure V.6. The attention block encompasses three lateral connections, as shown in Figure V.7. The first lateral connection integrates an average pooling layer, a convolution layer, and a clipped ReLU activation layer, while the second f2 lateral connection is composed of a batch normalization layer, a convolution layer, and a ReLU activation layer, the third encompasses a paypass layer initially

derived from the concatenation layer spanning from fire modules 5 up to the final concatenation layer.

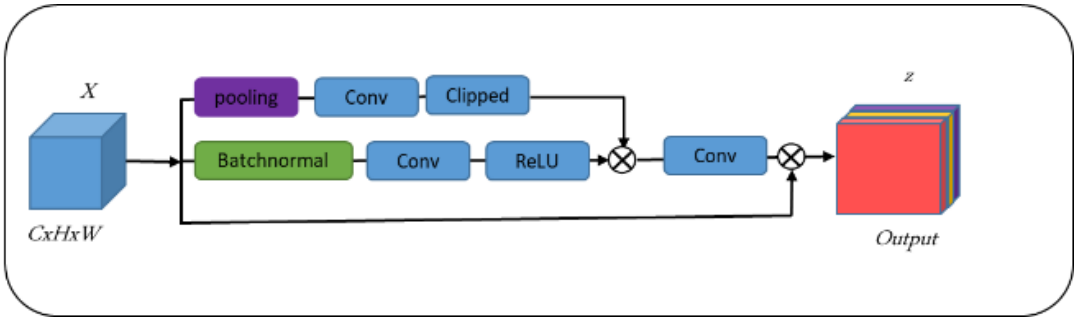


**Fig. V.8** The block attention module

The purpose of this block is to localize the airgap fault through low-frequency emphasis. The structure of this block is presented in figure V.8. In this case, concentrating on the horizontal direction proves sufficient for aggregating airgap fault features. Within this dimension, for a given input $X \in \Re^{CxHxW}$ where X is a member of the input space, we employ a spatial extent using a pooling kernel (1,W), This process encodes each channel across the vertical coordinates., resulting in the formulation of the output for the c-th channel at width w :"

$$P(X) = \frac{1}{W} \sum_{0 \le i \le W} x_c(h,i) \tag{V.12}$$

Equation (V.12) allows a global comprehensive receptive field while encoding accurate positional details. The specific value corresponding to this mechanism can be expressed as:

$$f_1 = \sigma_1\left(conv\left(P(x)\right)\right) \tag{V.13}$$

$$f_2 = \sigma_2\left(conv\left(\beta(x)\right)\right) \tag{V.14}$$

$$F = [f_1, f_2] \tag{V.15}$$

The result generated by our coordinate attention can be formulated as:

$$output = [conv(f), X] \tag{V.16}$$

where, the concatenation operation [·, ·] combines elements, while δ1, δ2 represent Clipped RELU and RELU activation functions, respectively, both accompanied by batch normalization.

## V.4. Experimental of air gap fault diagnosis results

In this section, the assessment of the proposed technique efficacy in diagnosing airgap faults is conducted. The key goal revolves around appraising the effectiveness and precision of the intelligent diagnostic based on Hilbert Transform (HT), Variational Mode Decomposition (VMD), and a deep learning model. An assortment of 3D images produced through VMD signal-to-image conversion, along with map data, is employed for the purpose of testing and assessing the suggested model. In fact, for every type of airgap eccentricity fault severity, the acquired stator currents are segmented into brief, overlapping time windows. Subsequently, the VMD algorithm was applied to analyze these segmented signals. For each signal, a collection of Intrinsic Mode Functions (IMFs) is generated, and their energies are computed following equation (V.2) to create the CEIMS matrix. The EWCS matrix is normalized and then combined with the knowledge map to create the fused 3D image containing integrated information. Lastly, the resulting image is resized to dimensions of 227x227.

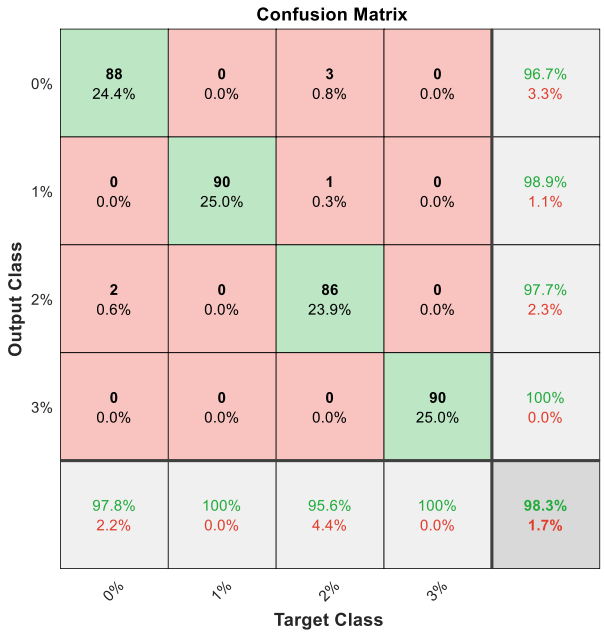


0.

**Fig. V.9** The matrix confusion

This resized image will serve as the input for our CNN model. The adapted CNN model was implemented within a MATLAB environment on a computer equipped with two E5-2667 v3 CPUs, a GTX1080Ti GPU, 32GB of memory, and a 1TB hard drive. We utilized a dataset

containing 300 images for each class, and these images were partitioned into distinct training and testing sets. The training set consisted of 70% of the data, leaving the remaining 30% for testing purposes. Throughout the training phase, the system acquired knowledge about distinctive features. Subsequently, the developed model was validated through the testing phase. The experimental results of the enhanced CNN model are illustrated in Figure V.9 and Figure V.10. These figures represent.

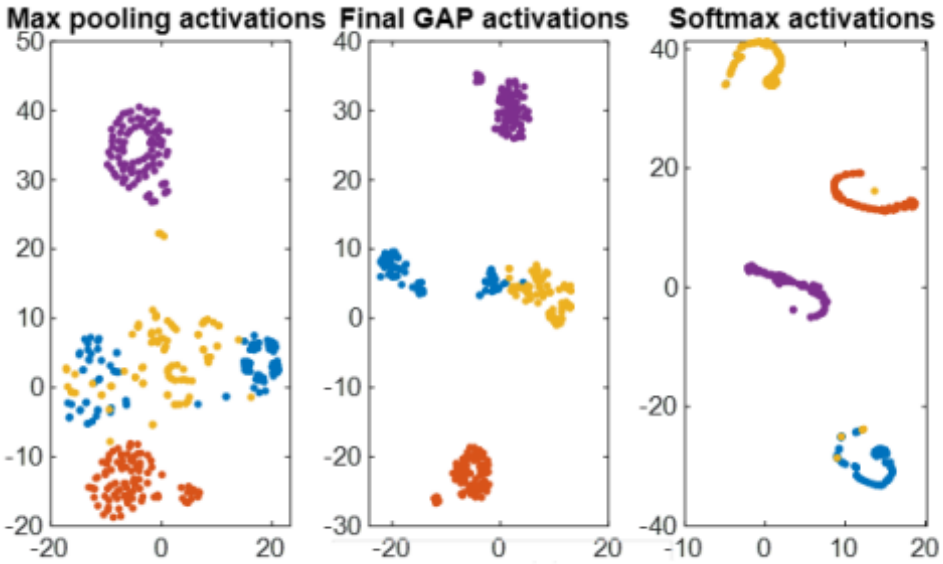


**Fig. V.10** T-SNE visualization

T-SNE visualization results, respectively. It can be observed that the model has achieved a prediction accuracy of over 99%. The evaluation of airgap eccentricity fault diagnosis accuracy using various deep learning algorithms based on CNN is outlined in Table 1. It is evident from the table that the proposed CNN model exhibits superior accuracy and speed when compared to standard models like SqueezeNet, AlexNet, ResNet-50, and MobileNet.

Table 1 Comparison with DL algorithms

| Index class | Type of fault (%) | Consuming time (s) |
|---|---|---|
| Proposed model | 99.4 | 72 |
| SqueezNet | 99.3 | 50 |
| Mobilenet | 99.7 | 72 |
| Alexnet | 99.5 | 72 |
| RESNET50 | 99.7 | 60 |

### Case study 2: diagnostic of inter turn short circuit (ITSC) fault using VMD and CNN

Short circuit faults in stator windings are widely acknowledged as the primary cause of failure in electrical machines. The detection of this fault is very challenging. In fact, even a small number of shorted turns can lead to significant issues. It can produce a tragic breakdown not only within the motor itself but also in its associated equipment. However, when a short circuit fault occur even for a low fault severity, it will affect the magnitude of the $f_{\mathrm{ITSCH}}$ it will affect the magnitude of the ITSC f harmonic as reported in (DE 2009; FAN 2021), and which can be described in a similar manner as the expression in (V.6).The advantage of this frequency is it characterize the fault of the short circuit frequency signature in the low frequency band that helps to discern between the faulty and healthy state. However, the challenging aspect of diagnosing this fault is that a very small number of turns in short circuit cannot be directly detected from the raw signal. To overcome this problem, Deep learning and advanced preprocessing data method can provide a solution to resolve this issue. The primary advantage of applying deep learning in fault diagnosis is that it can solve the aforementioned problem by treating signals or specific faults as unique image representations. However, regarding the study of this fault. Most DL approaches does not integrate its localizations or severity estimation. By adhering to the same fault diagnosis methodology outlined earlier, the detection of ITSC (Inter-Turn Short Circuit) faults can be effectively accomplished.

## V.5. Data description

This section explains the experimental data employed for the proposed CNN-based fault model for the identification and diagnosis of ITSC faults. In fact, the proposed improvement SqueezNet is conducted on the experimental data with multiple ITSC faults and under different motor operating conditions. Figure V.9 illustrates the experimental test bench utilized in this work, which is composed of a 1.1 kW squirrel-cage induction motor, an external box is incorporated to introduce ITSC faults into the stator phase, enabling the variation of the number of turns, as shown in Figure V. 10. The mechanical load consists of powder brake driven by a control unit. The currents in the three-phase stator of the induction motor were obtained through current sensors and sampled at a rate of 10 kHz using an NI 6036-E series data acquisition card.

The dataset, with 3000 samples, included ten different states of ITSC fault: healthy, and nine different faulty state, as shown in table 2. For training purposes, 210 samples were selected from each state, resulting in a total of 2100 training samples. For testing purposes, 90 samples were selected from each state, resulting in a total of 900 testing samples.

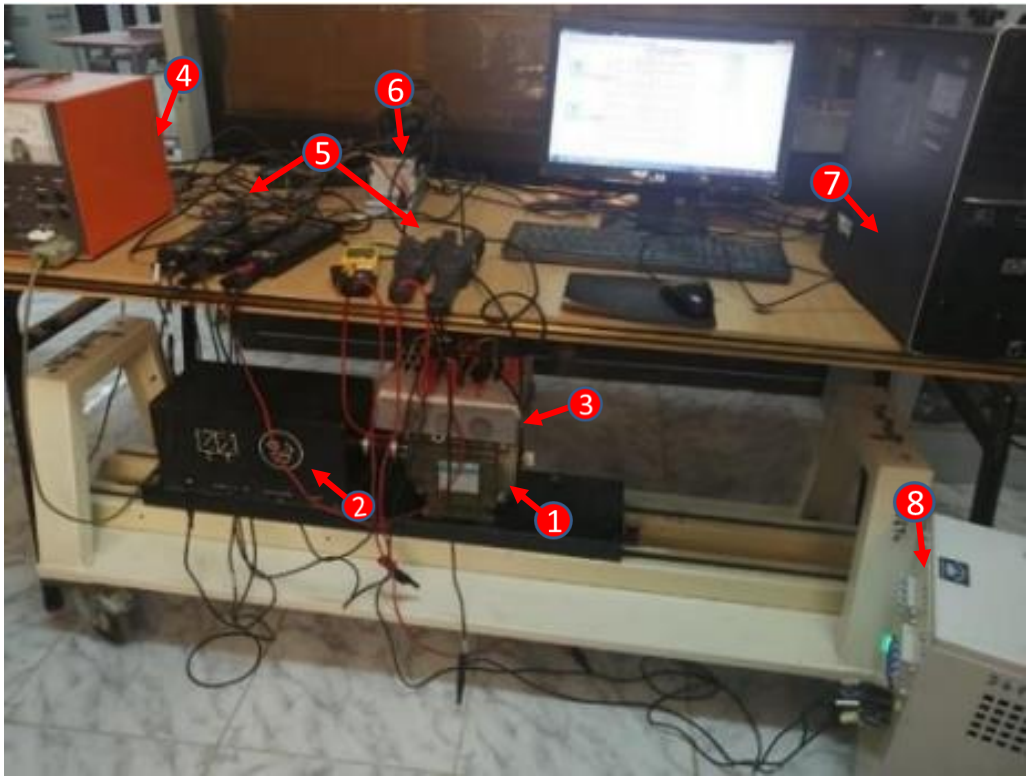


**Fig. V.11** The experimental setup: (1) 3-phase, 1.1 kW Induction motor, (2) powder brake, (3) External box with several ITSC fault, (4) Control unit of powder break, (5) current and voltage sensors, (6) NI 6036-E series data acquisition card, (7) (Pc) data processing unit, (8) 3-Phase Power

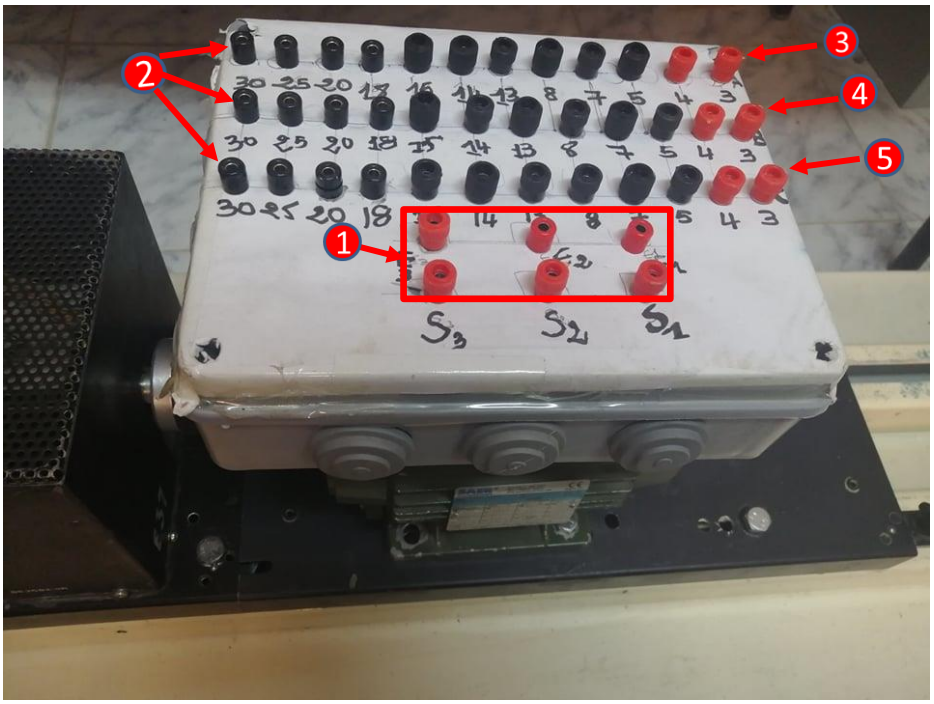


**Fig. V. 12** External box with several ITSC fault: (1) Three phases inputs and outputs of induction, (2) External box enables introducing the ITSC faults with different number of turns in three phases, (3, 4, 5) the stator three phases.

Table.V 2 Index class related to different type of fault

| Index class | Type of fault | Number of shorted terms |
|---|---|---|
| AF_a | ITSC_phaseA_no load | 7 |
| AF_b | ITSC_phaseA_no load | 13 |
| AF_c | ITSC_phaseA_no load | 15 |
| AF_e | ITSC_phaseA_30% of rated load | 5 |
| AF_d | ITSC_phaseA_30% of rated load | 7 |
| BF_a | ITSC_phaseA_30% of rated load | 13 |
| BF_b | ITSC_phaseB_no load | 20 |
| BF_c | ITSC_phaseB_50% of rated load | 13 |
| BF_d | ITSC_phaseB_50% of rated load | 15 |

## N V.6. Analysis Based on Variational mode decomposition (VMD)

The methodology adopted in this section is the same as presented in Figure V. First the stator current envelope was decomposed into Several IMFs via VMD method. Thus, the first five obtained IMFs for healthy and faulty state are shown in figure V. 13.

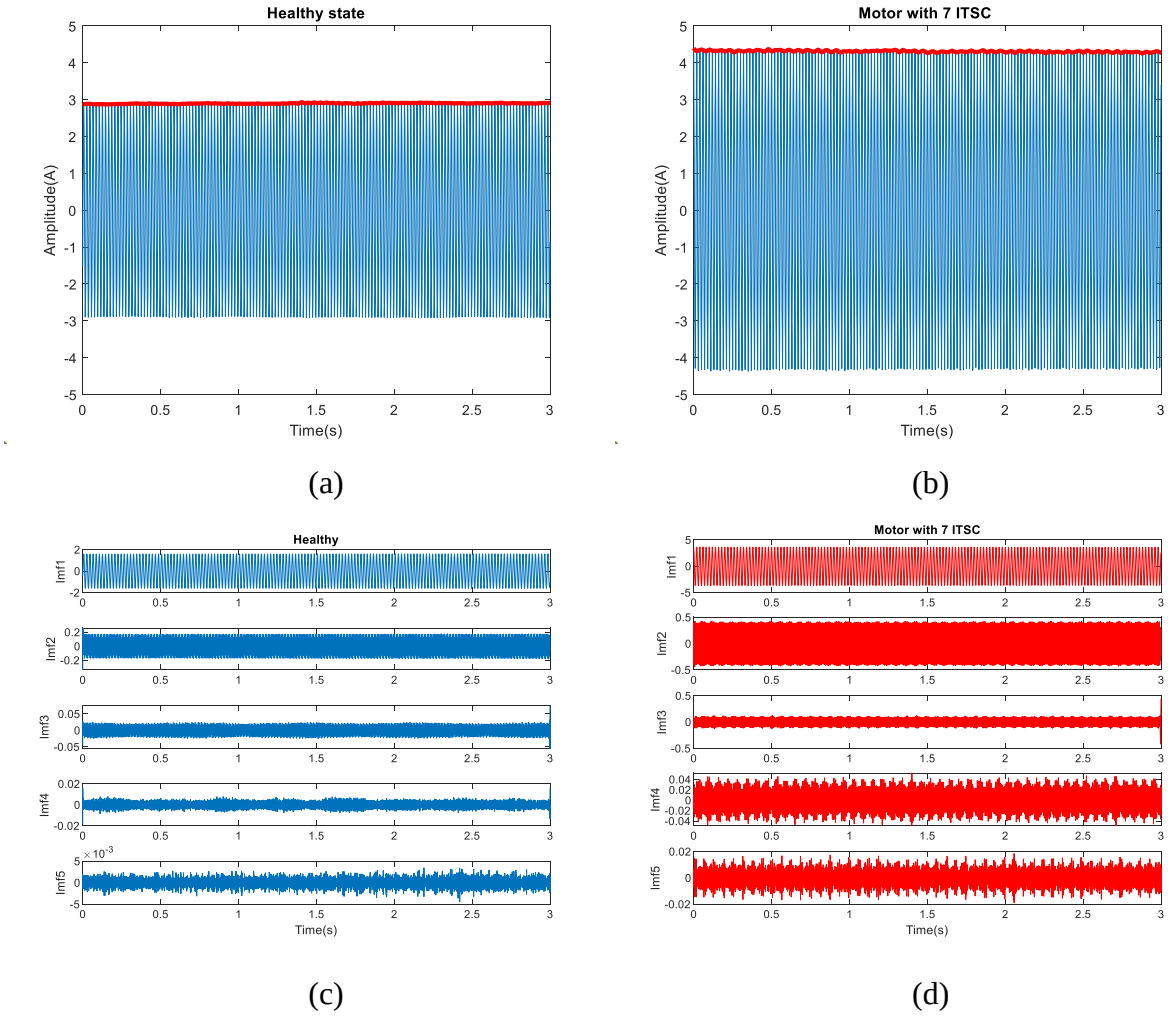


**Fig. V. 13 (a)** Stator current and its envelope for healthy state, (b) Motor with 7 ITSC

(c) IMFs healthy state (d) IMFs faulty state

## V.7 The Experimental results of ITSC faults classification via Deep Learning

In the second experiment, we have used a database composed by 3000 images. The dataset was divided into two subsets: training and testing. The training subset comprised 70% of the data, while the remaining 30% was allocated for testing. A significant performance improvement is achieved when the improved CNN model is applied.

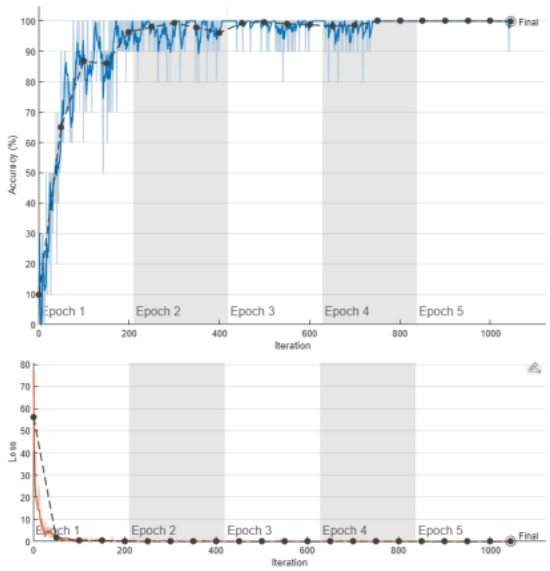


**Fig. 13** Accuracy training and testing of the proposed CNN.

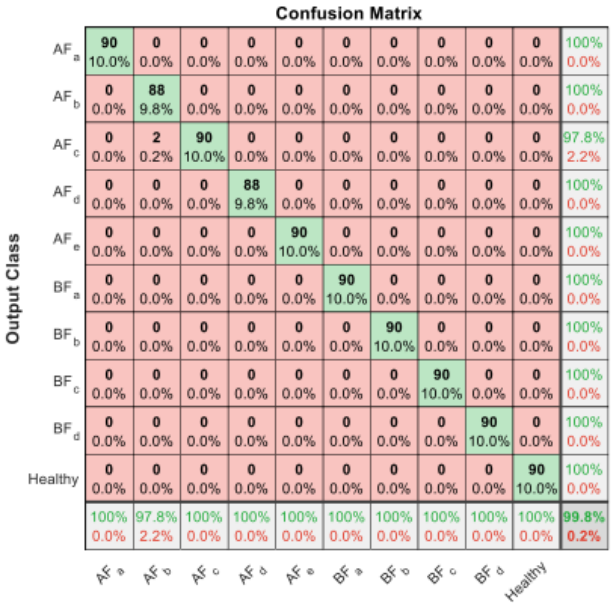


**Fig. V. 14**. Confusion matrix

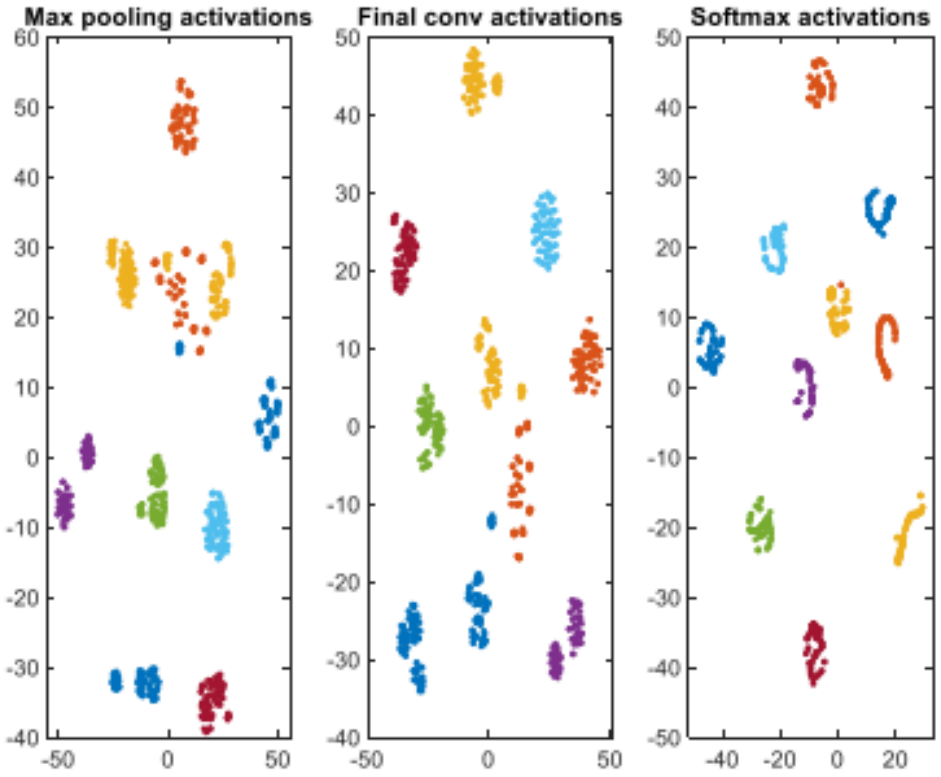


**Fig. V. 15** T-SNE visualization

The experimental results is illustrated in figure.V.13, figure.V.14 and figure V.15, which represent the training and testing accuracy, the confusion matrix and T-SNE visualization results respectively. We can see that the model has correctly predicted and classified the fault types and

degree under different conditions, which is also consistent with the T-SNE visualization as well. The evaluation metrics presented in table V.3 shows the performance of our CNN model. Experimental results showed a significant performance is achieved across all metrics.

Table V.3 Results obtained by applying CNN

| | | **Sensitivity** | **Specificity** | **Precision** | **F1-Score** | **Accuracy** |
|---|---|---|---|---|---|---|
| Dataset With ITSC fault | **AF_a** | 1 | 1 | 1 | 1 | 0.997772 |
| | **AF_b** | 1 | 0.9975 | 0.88 | 0.9351 | |
| | **AF_c** | 0.9782 | 1 | 1 | 0.989 | |
| | **AF_d** | 1 | 1 | 1 | 1 | |
| | **AF_e** | 1 | 1 | 1 | 1 | |
| | **BF_a** | 1 | 1 | 1 | 1 | |
| | **BF_b** | 1 | 1 | 1 | 1 | |
| | **BF_c** | 1 | 1 | 1 | 1 | |
| | **BF_d** | 1 | 1 | 1 | 1 | |
| | **Healthy** | 1 | 1 | 1 | 1 | |
| Airgap eccentricity fault | **1%** | 1 | 0.9777 | 0.989 | 0.989 | 0.9833 |
| | **2%** | 0.9555 | 0.9781 | 0.9772 | 0.9888 | |
| | **3%** | 1 | 1 | 1 | 1 | |
| | **Healthy** | 0.9777 | 0.9851 | 0.9670 | 0.9723 | |

## V.8 Conclusion

In this chapter, we have presented our main contribution that consist of developing an improvement CNN model served to classify the airgap eccentricity fault and the ITSC fault.. This work is based on two main points: (1) Data image quality: novel technique is proposed to create input CNN. This image is generated through the fusion of data images and the knowledge map, this amalgam facilities the pertinent feature extraction. (2) Appropriate architecture model: this is done using an improvement pretrained SqueezNet associated with attention block mechanism that achieved high accuracy in image classification. Results from applying CNN model confirmed that

# General Conclusion

Given the increasing evolution of asynchronous machines in industrial sectors, the early detection of faults in these machines has become an important economic issue. The growing interest of manufacturers in the maintenance of electric drives justifies the emphasis placed by research on the diagnosis of asynchronous machines. It is therefore important to develop detection and diagnostic tools to monitor the operating status of the machine.

The work presented in this manuscript contributes to the diagnosis of asynchronous machines faults. The objective of this thesis is to study the effectiveness of artificial intelligence techniques combined with advanced signal processing methods for the detection and automatic diagnosis of asynchronous machine faults.

Neural networks and deep learning are two techniques from artificial intelligence, which can provide an interesting solution for industrial equipment monitoring problems. In fact, their use does not require the existence of a formal model of this equipment. Furthermore, their capacities for memorization, learning and adaptation represent very useful functions for any autonomous monitoring system.

The proper functioning of a diagnostic approach using intelligent methods requires a rich and significant database to achieve this, it is essential to have good criteria, which best represents the defects. In this context, the issues addressed in this thesis led to the development of two key contributions that address the inquiries raised in the introduction. These contributions can be summarized as follows:

- The development of two automatic and robust diagnostic systems, aim to detect and identify the severity fault in the squirrel cage bars. The first combines discrete wavelet decomposition with artificial neural networks (ANN). While the second uses a high-resolution method known as MUSIC method, which aims to estimate the stator current parameters in order to create the best indicators, which are used as input to the ANN. the obtained results show the effectiveness of this technique in the detection automatic of the defect and the determination of its severity.

- The development of an improved conventional neural network (CNN) model, intended for the classification of eccentricity and short-circuit faults. This work is based on two tasks:

  **Quality of data images:** the used input images to the CNN, are generated through the fusion of the data image and the knowledge map. The first image is built from the analyzed multiple signal sensors via HT and VMD. While, the second image encompasses fault characteristics and domain information. This amalgamation facilitates the extraction of relevant characteristics.

  **Appropriate model architecture:** the association of an improved SqueezNet model with an attention block achieves this issue. This new structure gives high accuracy in image classification.

The work carried out within the framework of this thesis could give rise to other complementary studies on several points:

- Extend the study of faults, in particular the most frequent faults, which are the short circuit faults between phases of the stator and between phase and earth.
- Find other fault indicators allowing us to discern between the presence of a short circuit between turns of the same phase and on two phases.
- The application of our model for fault classification on other machines

. Caractéristiques des machines utilisées

| **Caractéristiques** | **Moteur asynchrone** 3 kW | **Moteur asynchrone 1.1 kW** |
|---|---|---|
| **La vitesse nominale** | 1430 tr/min | **1417 tr/min** |
| **La tension nominale** | 380 V | **380 V** |
| **Le courant nominal** | 6.40 A | **2.80 A** |
| **Nombre de barres rotoriques** | 28 | **28** |

## Annex A2

### The experimental test bench

To evaluate the efficiency of our diagnostic approach, we apply the proposed model to experimental data encompassing various instances of airgap faults, and under diverse motor operating conditions. The used experimental test rig is shown in figure A2.1. This setup involves a three-phase induction motor 1.1 kW, operating at 50 Hz with 4 poles. A mechanical load consists of powder brake driven by unit a control. The currents and voltage were obtained via the sensors and sampled at a rate of 10 kHz using dSpace 1104.

**Fig. A2.1** The experimental setup:

# Reference


[AFR 22] Afroz, Zakia, et al. "Predictive modelling and optimization of HVAC systems using neural network and particle swarm optimization algorithm." *Building and environment* 209 (2022): 108681.

[AHM 08] Ahmed and M. Ahmed, "Comparison of Stator Current, Axial leakage Flux and Instantaneous Power to Detect Broken Rotor Bar Faults in Induction Machines," in Proc. Australasian Universities Power Engineering Conference (AUPEC'08), pp. 1-6, 2008.

[AHM 22] Ahmed, Ammar, et al. "Empirical Mode Decomposition-Based Feature Extraction for Environmental Sound Classification." *Sensors* 22.20 (2022): 7717.

[ALB 17] Albawi, Saad, Tareq Abed Mohammed, and Saad Al-Zawi. "Understanding of a convolutional neural network." *2017 international conference on engineering and technology (ICET)*. Ieee, 2017.

[ALI 09] Ali IBRAHIM, “Contribution au diagnostic de machines électromécaniques : Exploitation des signaux électriques et de la vitesse instantanée ’. Doctoral thesis. Jean Monnet University, French, March 2009.

[ALI 22] Ali. Namdar, "A robust principal component analysis-based approach for detection of a stator inter-turn fault in induction motors." *Protection and Control of Modern Power Systems* 7.1 (2022): 1-24.

[ALL 88] Allianz, "Présentations des avaries. Machines électriques tournantes," s. CP2, prevention notebook. Allianz, 1988.

[ALT 22] Althubaiti, Adnan, Faris Elasha, and Joao Amaral Teixeira. "Fault diagnosis and health management of bearings in rotating equipment based on vibration analysis–a review." *Journal of Vibroengineering* 24.1 (2022): 46-74.

[ALZ 21] Alzubaidi, Laith, et al. "Review of deep learning: Concepts, CNN architectures, challenges, applications, future directions." *Journal of big Data* 8 (2021): 1-74.

[AMI 20] Amirat, Yassine, et al. "Modal Decomposition for Bearing Fault Detection." *Electrical Systems 1: From diagnosis to prognosis* (2020): 121-168.

[AND 08] R. N. Andriamala, H. Razik, L. Baghli, and F. M. Sargo," Eccentricity Fault Diagnosis of aDual-Stator Winding Induction Machine Drive Considering the Slotting Effects," IEEETransactions on Industrial Electronics, Vol. 55, pp. 4238-4251, December 2008.

[AND 12] C. Andrian, " Méthode Globale de Diagnostic des Machines Électriques,", Doctoral thesis, University of Lille de Nord French. ,February 2012.

[BAI 17] Baiche, Karim, and Lachouri Abderrazak. "A statistical parameters and artificial neural networks application for rolling element bearing fault diagnosis using wavelet transform preprocessing." *2017 5th International Conference on Electrical Engineering-Boumerdes (ICEE-B)*. IEEE, 2017.

[BAI 20] Bai, Mingliang, et al. "Long short-term memory network-based normal pattern group for fault detection of three-shaft marine gas turbine." *Energies* 14.1 (2020): 13.

[BAL 12] Baldi, P.: Autoencoders, unsupervised learning, and deep architectures. In: I. Guyon, G. Dror, V. Lemaire, G. Taylor, D. Silver (eds.) Proceedings of ICML Workshop on Unsupervised and Transfer Learning, Proceedings of Machine Learning Research, vol. 27, pp. 37–49. PMLR, Bellevue, Washington, USA (2012)

[BAN 20] Bank, D., Koenigstein, N., & Giryes, R. (2020). Autoencoders. *arXiv preprint arXiv:2003.05991*.

[BEL 20] Belkacemi, Bellal, et al. "Detection of induction motor improper bearing lubrication by discrete wavelet transforms (DWT) decomposition." *Instrum. Mes. Metrol* 19.5 (2020): 347-354.

[BEL 21] Belaala, A. (2021). *Big Data analytics using Artificial Intelligence techniques in medical PHM* (Doctoral dissertation, University Mohamed Kheider Bskra).

[BEN 07] Y. Bentaleb, "Analyse par ondelettes des signaux sismiques : Applications aux ondes de surface," Doctoral thesis, University of Mohamed V, Rabat, Maroc, 2007.

[BOG 12] Bogiatzidis, Ioannis X., Athanasios N. Safacas, and Epaminondas D. Mitronikas. "Detection of backlash phenomena appearing in a single cement kiln drive using the current and the electromagnetic torque signature." *IEEE Transactions on Industrial Electronics* 60.8 (2012): 3441-3453.

[BON 86] Bonnett, Austin H., and George C. Soukup. "Rotor failures in squirrel cage induction motors." *IEEE transactions on industry applications* 6 (1986): 1165-1173.

[BON 22] Bonet-Jara, Jorge, and Joan Pons-Llinares. "A precise, general, non-invasive and automatic speed estimation method for MCSA diagnosis and efficiency estimation of induction motors." *IEEE Transactions on Energy Conversion* (2022).

[BOU 01] T. Boumegoura, "Recherche de Signature électromagnétique des Défauts dans une Machine Asynchrone et synthèse d'Observateurs en

vue de Diagnostic," Doctoral thesis. Ecole centrale de Lyon, France, Mars 2001.

[BOU 07] Bouzid MBK, Champenois G, Bellaaj NM, Signac L, Jelassi K (2007) An effective neural approach for the automatic location of stator interturn faults in induction motor. IEEE Trans Industr Electron 55:4277–4289.

[CAN 07] Cann, P. M., et al. "Grease degradation in R0F bearing tests." *Tribology Transactions* 50.2 (2007): 187-197.

[CAN 19] Canizo, Mikel, et al. "Multi-head CNN–RNN for multi-time series anomaly detection: An industrial case study." *Neurocomputing* 363 (2019): 246-260.

[CHA 23] Chacón, Ana María Peco, Isaac Segovia Ramírez, and Fausto Pedro García Márquez. "K-Nearest Neighbour and K-fold cross-validation used in wind turbines for false alarm detection." *Sustainable Futures* (2023): 100132.

[CHE 20] Chen, Zhuyun, et al. "A deep learning method for bearing fault diagnosis based on cyclic spectral coherence and convolutional neural networks." *Mechanical Systems and Signal Processing* 140 (2020): 106683.

[CHU 20] Chuan, et al. "A systematic review of deep transfer learning for machinery fault diagnosis." *Neurocomputing* 407 (2020): 121-135.

[CLE 89] Clergeot, Henri, Sara Tressens, and Abdelaziz Ouamri. "Performance of high resolution frequencies estimation methods compared to the Cramer-Rao bounds." *IEEE transactions on acoustics, speech, and signal processing* 37.11 (1989): 1703-1720.

[COS 17] Coşkun, Musab, et al. "An overview of popular deep learning methods." *European Journal of Technique (EJT)* 7.2 (2017): 165-176.

[DEF 21] Defdaf, Mabrouk, et al. "A new transform discrete wavelet technique based on artificial neural network for induction motor broken rotor bar faults diagnosis." *International Transactions on Electrical Energy Systems* 31.4 (2021): e12807.

[DEV 02] V. Devanneaux, "Modélisation des machines asynchrones triphasées à cage d'écureuil en vue de la surveillance et du diagnostic,". Doctoral thesis 'Institut National Polytechnic of Toulouse, France, December 2002.

[DIA 22] Diarra, Mahamadou Negue, et al. "Induction Motors Speed Estimation by Rotor Slot Harmonics Frequency Using Zoom Improved Chirp-Z Transform Algorithm." *Energies* 15.21 (2022): 7877.

[DID 04] DIDIER. G, "Modélisation et Diagnostic de la machine asynchrone en présence de défaillances,". Doctoral thesis, University Henri Poincaré, Nancy-I, French, October 2004.

[DIN 17] Ding, Xiaoxi, and Qingbo He. "Energy-fluctuated multiscale feature learning with deep convnet for intelligent spindle bearing fault diagnosis." *IEEE Transactions on Instrumentation and Measurement* 66.8 (2017): 1926-1935.

[DIN 22] Ding J, C. Liu, R. Li, J. You, & L.Jia". An improved deep forest classification algorithm". International Journal of Modelling, Identification and Control,vol.40(4), pp.305-314.2022

[DRA 13] Dragomiretskiy, Konstantin, and Dominique Zosso. "Variational mode decomposition." *IEEE transactions on signal processing* 62.3 (2013): 531-544.

[DRE 22] Dreher, Nathali Rolon, et al. "Feature analysis by k-means clustering for damage assessment in rotating machinery with rolling bearings." *Journal of the Brazilian Society of Mechanical Sciences and Engineering* 44.8 (2022): 330.

[DRI 08] M. Drif, A. J. M. Cardoso, "Airgap-eccentricity fault diagnosis, in three-phase induction motors, by the complex apparent power signature analysis," IEEE Transaction on Industrial Electronics, Vol.55, n°3, Mar. 2008.

[DRI 09] M. Drif, A. J. M. Cardoso, "The use of the instantaneous-reactive-power signature analysis for rotor-cage-fault diagnostics in three-phase induction motors," IEEE Transaction on Industrial Electronics, Vol. 56, n° 11, pp. 4606–4614, Nov. 2009.

[EGA 17] Egan, Shannon, et al. "Long Short-Term Memory (LSTM) networks with jet constituents for boosted top tagging at the LHC." *arXiv preprint arXiv:1711.09059* (2017).

[ELB 17] Elbouchikhi, Elhoussin, et al. "Motor current signal analysis based on a matched subspace detector." *IEEE Transactions on Instrumentation and Measurement* 66.12 (2017): 3260-3270.

[ELB 21] Elbouchikhi, Elhoussin, et al. "Overview of signal processing and machine learning for smart grid condition monitoring." *Electronics* 10.21 (2021): 2725.

[ERE 17] Eren, Levent. "Bearing fault detection by one-dimensional convolutional neural networks." *Mathematical Problems in Engineering* 2017 (2017): 1-9.

[FAI 16 ] Faiz, Jawad, and S. M. M. Moosavi. "Eccentricity fault detection–From induction machines to DFIG—A review." *Renewable and Sustainable Energy Reviews* 55 (2016): 169-179.

[FUC 96] Fuchs, J-J. "Rectangular Pisarenko method applied to source localization." *IEEE transactions on signal processing* 44.10 (1996): 2377-2383. [GHE 21]

[GHE 21] Gherabi, Zakaria, et al. "Discrimination between demagnetization and eccentricity faults in PMSMs using real and imaginary components of stator current spectral analysis." *Journal of Power Electronics* 21 (2021): 153-163.

[GUE 20] Guedidi, Asma, et al. "Diagnosis and Classification of broken bars fault using DWT and Artificial Neural Network without slip estimation." *2020 XI International Conference on Electrical Power Drive Systems (ICEPDS)*. IEEE, 2020.

[GUE 23] Guedidi, Asma, et al. "Early detection and localization of stator inter turn faults based on variational mode decomposition and deep learning in induction motor." *Diagnostyka* (2023): 1-13.

[GUO 16] Guo, Xiaojie, Liang Chen, and Changqing Shen. "Hierarchical adaptive deep convolution neural network and its application to bearing fault diagnosis." *Measurement* 93 (2016): 490-502.

[GRY 12] Gryllias, Konstantinos C., and Ioannis A. Antoniadis. "A Support Vector Machine approach based on physical model training for rolling element bearing fault detection in industrial environments." *Engineering Applications of Artificial Intelligence* 25.2 (2012): 326-344.

[GUP 99] Gupta, P., & Sinha, N. K. (1999). of Nonlinear Systems: An Overview. *Soft Computing and Intelligent Systems: Theory and Applications*, 337.

[HAL 22] Halder, Sudip, et al. "Broken rotor bar fault diagnosis techniques based on motor current signature analysis for induction motor—A review." *Energies* 15.22 (2022): 85690

[HAN 20] Han, Tian, et al. "Bearing fault identification based on convolutional neural network by different input modes." *Journal of the Brazilian Society of Mechanical Sciences and Engineering* 42 (2020): 1-10.

[HEN 03] H. Henao, C. Demian, G. A. Capolino, "A frequency-domain detection of stator winding faults in induction machines using an external flux sensor," *IEEE Transactions on Industry Application,* V*ol. 39, No. 5, pp. 1272–1279, Sep./Oct. 2003.*

[HIN 11] Hinton, Geoffrey E., Alex Krizhevsky, and Sida D. Wang. "Transforming auto-encoders." *Artificial Neural Networks and Machine Learning–ICANN 2011: 21st International Conference on Artificial Neural Networks, Espoo, Finland, June 14-17, 2011, Proceedings, Part I 21*. Springer Berlin Heidelberg, 2011.

[HOC 97] Hochreiter, Sepp, and Jürgen Schmidhuber. "Long short-term memory." *Neural computation* 9.8 (1997): 1735-1780.

[HOS 19] Hossain, Md Anwar, and Md Shahriar Alam Sajib. "Classification of image using convolutional neural network (CNN)." *Global Journal of Computer Science and Technology* 19.2 (2019).

[HOW 17] Howard, Andrew G., et al. "Mobilenets: Efficient convolutional neural networks for mobile vision applications." *arXiv preprint arXiv:1704.04861* (2017).

[HUA 18] Huang, Ruyi, et al. "Deep decoupling convolutional neural network for intelligent compound fault diagnosis." *Ieee Access* 7 (2018): 1848-1858.

[HUI 22a] Huimin, Zhao,, et al. "Bearing fault diagnosis using transfer learning and optimized deep belief network." *Measurement Science and Technology* 33.6 (2022): 065009.

[HUI 22b] Huimin, Zhao et al. "Intelligent diagnosis using continuous wavelet transform and gauss convolutional deep belief network." *IEEE Transactions on Reliability* (2022).

[IMA 23] Iman, Mohammadreza, Hamid Reza Arabnia, and Khaled Rasheed. "A review of deep transfer learning and recent advancements." *Technologies* 11.2 (2023): 40.

[IRF 19] Irfan, Muhammad, et al. "Analysis of distributed faults in inner and outer race of bearing via Park vector analysis method." *Neural Computing and Applications* 31 (2019): 683-691.

[JAN 21] Janiesch, C., Zschech, P., & Heinrich, K. (2021). Machine learning and deep learning. *Electronic Markets*, *31*(3), 685-695.

[JIA 19] J. Jiao, M. Zhao, J. Lin, C. Ding, Deep Coupled Dense Convolutional Network With Complementary Data for Intelligent Fault Diagnosis, IEEE Trans. Ind. Electron., 66 (12) (2019) 9858-9867.

[JIA 20] Jiangquan. Zhang, et al. "A new bearing fault diagnosis method based on modified convolutional neural networks." *Chinese Journal of Aeronautics* 33.2 (2020): 439-447.

[JIA 23] Jia, Linshan, Tommy WS Chow, and Yixuan Yuan. "GTFE-Net: A Gramian time frequency enhancement CNN for bearing fault diagnosis." *Engineering Applications of Artificial Intelligence* 119 (2023): 105794.

[JIN 20] Jinyang Jiao,, et al. "A comprehensive review on convolutional neural network in machine fault diagnosis." *Neurocomputing* 417 (2020): 36-63.

[KAE 96] Kaelbling, L. P., Littman, M. L., & Moore, A. W. (1996). Reinforcement learning: A survey. *Journal of artificial intelligence research*, *4*, 237-285.

[KAI 16] Kaiming. He, et al. "Deep residual learning for image recognition." *Proceedings of the IEEE conference on computer vision and pattern recognition*. 2016.

[KAM 16] Karmakar, Subrata, et al. *Induction motor and faults*. Springer Singapore, 2016.

[KAN 14] Kangro, Rait, et al. "Air-gap eccentricity analysis of slow-speed slotless permanent magnet synchronous generator." *2014 Electric Power Quality and Supply Reliability Conference (PQ)*. IEEE, 2014.

[KAR 11] Karagiannis, Alexandros, and Philip Constantinou. "Computation time study in biomedical signal processing with Empirical Mode Decomposition: The case of electrocardiogram." *2011 17th International Conference on Digital Signal Processing (DSP)*. IEEE, 2011.

[KIA 07] Kia Shahin. H., H. Henao and G.-A. Capolino, "A High-Resolution Frequency Estimation Method for Three-Phase Induction Machine Fault Detection," IEEE Transaction on Industrial. Electrons., Vol. 54, n° 4, pp. 2305-2314, August 2007.

[KHA 12] . Khaled, Yahia, " Contribution au Diagnostic de la Machine Asynchrone Triphasée par une Approche Signal " Doctoral thesis, university of Biskra, Algeria, 2012.

[KHE 09] A. Khezzar, E. K. Oumaamar, M. Hadjami, M. Boucherma, H. Razik, "Induction motor diagnosis using line neutral voltage signatures," *IEEE Transactions on Industrial Electronics, Vol. 56, No. 11, pp. 4581-4591, Nov.2009.*

[KLE 22] Klein, C., et al. "Effect of Static Eccentricity on the Mean Values of the Inductances of PMSMs." *2022 IEEE 21st Mediterranean Electrotechnical Conference (MELECON)*. IEEE, 2022.

[KON 14] N. Konstantinos. Gyftakis, "Identification of the Broken Bar Fault in Induction Motors with Rotor Air Ducts Through the Torque Spectrum," International on electrical machines (ICEM), 2014.

[KUM 84] Kumaresan, Ramdas, Donald W. Tufts, and Loues L. Scharf. "A Prony method for noisy data: Choosing the signal components and selecting the order in exponential signal models." *Proceedings of the IEEE* 72.2 (1984): 230-233.

[KUM 19] Kumar, Sanjay, et al. "A comprehensive review of condition based prognostic maintenance (CBPM) for induction motor." *IEEE Access* 7 (2019): 90690-90704.

[KUM 23] Kumar, R. Senthil, et al. "A combined HT and ANN based early broken bar fault diagnosis approach for IFOC fed induction motor drive." *Alexandria Engineering Journal* 66 (2023): 15-30.

[LAA 17] Laala Widad, “Contribution à la détection des défauts dans la machine à induction et à leur diagnostique par l’utilisation des techniques se basant sur l’intelligence artificiel (système expert et logique floue ‘. Doctoral thesis, university of Biskra, Algeria, 2017.

[LAA 20] Laala, Widad, Asma Guedidi, and Abderrazak Guettaf. "Bearing faults classification based on wavelet transform and artificial neural network." *International Journal of System Assurance Engineering and Management* (2020): 1-8.

[LAN 16] Landola, Forrest N., et al. "SqueezeNet: AlexNet-level accuracy with 50x fewer parameters and< 0.5 MB model size." *arXiv preprint arXiv:1602.07360* (2016).

[LE 19] Le, Xuan-Hien, et al. "Application of long short-term memory (LSTM) neural network for flood forecasting." *Water* 11.7 (2019): 1387.

[LI 18] Li. Y, K. Ding, G. He, X. Jiao, Non-stationary vibration feature extraction method based on sparse decomposition and order tracking for gearbox fault diagnosis, Measurement 124 (2018) 453–469.

[LI 20] Li, Xiang, et al. "Intelligent cross-machine fault diagnosis approach with deep auto-encoder and domain adaptation." *Neurocomputing* 383 (2020): 235-247.

[LIN 20] Lin, Li et al. "Adaptive short-time Fourier transform and synchrosqueezing transform for non-stationary signal separation." *Signal Processing* 166 (2020): 107231.

[LIA 20] Liang, Pengfei, et al. "Intelligent fault diagnosis of rotating machinery via wavelet transform, generative adversarial nets and convolutional neural network." *Measurement* 159 (2020): 1077680

[LIU 04] Z. Liu, X. Yin, Z. Zhang, D. Chen, W. Chen, "Online rotor mixed fault diagnosis way based on spectrum analysis of instantaneous power in squirrel cage induction motors," IEEE Transaction on Energy Conversion, Vol. 9, n°3, pp. 483-490, Sep. 2004.

[LIU 21] Liu, Zijian, et al. "A review of modeling and diagnostic techniques for eccentricity fault in electric machines." *Energies* 14.14 (2021): 4296.

[LOU 04] Loutridis, S. J. "Damage detection in gear systems using empirical mode decomposition." *Engineering Structures* 26.12 (2004): 1833-1841.

LOU 05] Loutridis, Spyridon, Evanthia Douka, and L. J. Hadjileontiadis. "Forced vibration behaviour and crack detection of cracked beams using instantaneous frequency." *Ndt & E International* 38.5 (2005): 411-419.

[LUO 18] Luo, Ping, et al. "Towards understanding regularization in batch normalization." *arXiv preprint arXiv:1809.00846* (2018).

[MA 09] Ma, Ming-Da, et al. "Fault detection based on statistical multivariate analysis and microarray visualization." *IEEE Transactions on industrial informatics* 6.1 (2009): 18-24.

[MAL 99] S. G. Malat, “A theory for multiresolution signal decomposition: the wavelet representation,” IEEE Transaction on Pattern Analysis and Machine Intelligence, Vol. 2, n° 7, Jul. 1989.

[MAR 03] Maruster, L. (2003). *A machine learning approach to understand business processes*. Technische Universiteit Eindhoven

[MED 12] MEDOUED AMMAR, “Surveillance et diagnostic des defauts des machines electriques : Application aux moteurs asynchrone’’, Doctoral thesis. University of 20 Août 1955-Skikda, Algeria, March 2012.

[MIS 22] Misra, Sajal, et al. "Fault detection in induction motor using time domain and spectral imaging-based transfer learning approach on vibration data." *Sensors* 22.21 (2022): 8210.

[MOH 21] Mohd Ghazali, Mohamad Hazwan, and Wan Rahiman. "Vibration analysis for machine monitoring and diagnosis: a systematic review." *Shock and Vibration* 2021 (2021): 1-25.

[MON 09] Monia B.B, "Diagnostic de défauts de la machine asynchrone par réseaux de neurones,". Doctoral thesis, University Tunis El Manar, Tunis, January. 2009.

[MOH 16] Mohammed, M., Khan, M. B., & Bashier, E. B. M. (2016). *Machine learning: algorithms and applications*. Crc Press.

[MUH 22] Muhammad Altaf, et al. "A new statistical features based approach for bearing fault diagnosis using vibration signals." *Sensors* 22.5 (2022).

[NEJ 00] Nejjari, Hamid, and Mohamed El Hachemi Benbouzid. "Monitoring and diagnosis of induction motors electrical faults using a current Park's vector pattern learning approach." *IEEE Transactions on industry applications* 36.3 (2000): 730-735.

[OKS 00] Oksimovic, Gojko M., et al. "Dynamic simulation of dynamic eccentricity in induction machines-winding function approach." *IEEE Transactions on Energy Conversion* 15.2 (2000): 143-148.

[OND 06] O. ONDEL "Diagnostic par reconnaissance des formes : Application a un ensemble convertisseur – machine asynchrone," Doctoral thesis. Central school of Lyon, October 2006.

[PAI 21] Paiva, Pedro RR, et al. "Online fault diagnosis for smart machines embedded in Industry 4.0 manufacturing systems: A labeled Petri net-based approach." *IFAC Journal of Systems and Control* 16 (2021): 100146.

[PAN 09] Pan, Sinno Jialin, and Qiang Yang. "A survey on transfer learning." *IEEE Transactions on knowledge and data engineering* 22.10 (2009): 1345-1359.

[POD 19] Poddar, Surojit, and N. Tandon. "Detection of particle contamination in journal bearing using acoustic emission and vibration monitoring techniques." *Tribology international* 134 (2019): 154-164.

[PRI 20] Prist, Mariorosario, et al. "Online fault detection: A smart approach for industry 4.0." *2020 IEEE International Workshop on Metrology for Industry 4.0 & IoT*. IEEE, 2020.

[QIA 20] Qiao, Meiying, et al. "Deep convolutional and LSTM recurrent neural networks for rolling bearing fault diagnosis under strong noises and variable loads." Ieee Access 8 (2020): 66257-66269.

[RAM 20] Ramu, Senthil Kumar, et al. "Broken rotor bar fault detection using Hilbert transform and neural networks applied to direct torque control of induction motor drive." *IET Power Electronics* 13.15 (2020): 3328-3338.

[RED 17] Redondo, Marte, C. A. Platero, and K. N. Gyftakis. "Turn-to-turn fault protection technique for synchronous machines without additional voltage transformers." *2017 IEEE 11th International Symposium on Diagnostics for Electrical Machines, Power Electronics and Drives (SDEMPED)*. IEEE, 2017.

[ROM 13] Romary, R., et al. "Electrical machines fault diagnosis by stray flux analysis." *2013 IEEE Workshop on Electrical Machines Design, Control and Diagnosis (WEMDCD)*. IEEE, 2013.

[SAH 12] S. Sahnoun, "Développement de méthodes d'estimation modale de signaux multidimensionnels. Application à la spectroscopie RMN multidimensionnelle", Doctoral thesis, University of Lorraine, French 2012.

[SAR 21] Sarker, I. H. (2021). Machine learning: Algorithms, real-world applications and research directions. *SN computer science*, *2*(3), 160.

[SCH 86] R. Schmidt, "Multiple emitter location and signal parameter estimation," IEEE Transaction on Antennas and Propagation, Vol. 34, n°3, pp. 276–280, 1986.

[SHA 13] Shashidhara, S. M., and P. S. Raju. "Stator winding fault diagnosis of three-phase induction motor by parks vector approach." *International Journal of Advanced Research in Electrical, Electronics and Instrumentation Engineering* 2.7 (2013): 2901-2906.

[SHA 15] Sharma, Amandeep, et al. "A review of fault diagnostic and monitoring schemes of induction motors." *Int. J. Res. Appl. Sci. Eng. Technol* 3 (2015): 1145-1152.

[SHA 20] Shaikh, Muhammad Faizan, Jongsan Park, and Sang Bin Lee. "A non-intrusive leakage flux based method for detecting rotor faults in the starting transient of salient pole synchronous motors." *IEEE Transactions on Energy Conversion* 36.2 (2020): 1262-1270.

[SID 05] Siddique, Arfat, G. S. Yadava, and Bhim Singh. "A review of stator fault monitoring techniques of induction motors." *IEEE transactions on energy conversion* 20.1 (2005): 106-114.

[SIN 21] Sinha, Ashish Kumar, et al. "ANN-based pattern recognition for induction motor broken rotor bar monitoring under supply frequency regulation." *Machines* 9.5 (2021): 87.

[SON 18] Song. L, H. Wang, P. Chen. “Vibration-based intelligent fault diagnosis for roller bearings in low-speed rotating machinery.” IEEE Trans. Instrum. Meas. 67 (2018) 1887–1899.

[SRI 09] Srinidhi, S, Tiwari, M, Burra, R, Gowda, H, & Siemers, PA. "Bearing Wear Due to Mechanical Stresses and Electrical Currents." *Proceedings of the ASME/STLE 2009 International Joint Tribology Conference*. *ASME/STLE 2009 International Joint Tribology Conference*. Memphis, Tennessee, USA. October 19–21, 2009. pp. 499-502.

[SRI 14] Srivastava, Nitish, et al. "Dropout: a simple way to prevent neural networks from overfitting." *The journal of machine learning research* 15.1 (2014): 1929-1958.

[SUN 18] Sun, Chuang, et al. "Sparse deep stacking network for fault diagnosis of motor." *IEEE Transactions on Industrial Informatics* 14.7 (2018): 3261-3270.

[SZE 15] Szegedy. C, W. Liu, Y. Jia, P. Sermanet, S. Reed, D. Anguelov, D. Erhan, V. Vanhoucke, and A. Rabinovich, “Going deeper with convolutions,” in Proceeding of the IEEE Conference on Computer Vison and Patter Recognition, Boston, MA, 2015, pp. 1-9.

[TAO 16] Tao, Jie, Yilun Liu, and Dalian Yang. "Bearing fault diagnosis based on deep belief network and multisensor information fusion." *Shock and Vibration* 2016 (2016).

[THO 95] O.V. THORSON, & M. DALVA"A survey of fault on induction motors in off shore oil industry, gas terminals, and oil refineries," IEEE Transaction on Industry Applications, Vol., 31, n°.5, pp.1186-1196, September 1995.

[THO 98] Thomson, William T., and Alexandra Barbour. "On-line current monitoring and application of a finite element method to predict the level of static airgap eccentricity in three-phase induction motors." *IEEE Transactions on Energy Conversion* 13.4 (1998): 347-357.

[TOR 10] Torrey, Lisa, and Jude Shavlik. "Transfer learning." *Handbook of research on machine learning applications and trends: algorithms, methods, and techniques*. IGI global, 2010. 242-264.

[TRA 09] Trajin B, «Analyse et traitement de grandeurs électriques pour la détection et le diagnostic de défauts mécaniques dans les entraînements asynchrones » Doctoral thesis, University of Toulouse, French, December 2009.

[TRA 10] Trajin, Baptiste, Jérémi Regnier, and Jean Faucher. "Comparison between vibration and stator current analysis for the detection of bearing faults in asynchronous drives." *IET electric power applications* 4.2 (2010): 90-100.

[WAN 19] Wang. J, Z. Mo, H. Zhang and Q. Miao, "A Deep Learning Method for Bearing Fault Diagnosis Based on TimeFrequency Image," in IEEE Access, vol. 7, pp. 42373- 42383, 2019,

[WAN 21] Wang. X., M. Dongxing & L. Xiaodong ". Bearing fault diagnosis based on vibro-acoustic data fusion and 1D-CNN network. Measurement, vol. 173, pp. 108-518. 2021.

[WAN 23] Wang, Huan, et al. "Interpretable convolutional neural network with multilayer wavelet for Noise-Robust Machinery fault diagnosis." *Mechanical Systems and Signal Processing* 195 (2023): 110314.

[WEI 21] Wei, X., Zhang, L., Yang, H. Q., Zhang, L., & Yao, Y. P. (2021). Machine learning for pore-water pressure time-series prediction: Application of recurrent neural networks. *Geoscience Frontiers*, *12*(1), 453-467.

[WOO 18] Woo, Sanghyun, et al. "Cbam: Convolutional block attention module." *Proceedings of the European conference on computer vision (ECCV)*. 2018.

[YAN 19] Yuan, Zhenyu, et al. "An enhanced fault-detection method based on adaptive spectral decomposition and super-resolution deep learning." *Interpretation* 7.3 (2019): T713-T725.

[YAN 21] Yang, Zhanshe, et al. "Fault diagnosis of mine asynchronous motor based on MEEMD energy entropy and ANN." *Computers & Electrical Engineering* 92 (2021): 107070.

[YAN 22] Yang, Shengkang, et al. "Deep multiple auto-encoder with attention mechanism network: A dynamic domain adaptation method for rotary machine fault diagnosis under different working conditions." *Knowledge-Based Systems* 249 (2022): 108639.

[YAN 23] Yan, Xiuting, et al. "Simulation Analysis of Tooth Break Faults of Gear Transmission System based on Electromagnetic Torque

Signal." *Journal of Physics: Conference Series*. Vol. 2508. No. 1. IOP Publishing, 2023.

[YAT 23] Yatsugi, Kenichi, et al. "Common Diagnosis Approach to Three-Class Induction Motor Faults Using Stator Current Feature and Support Vector Machine." *IEEE Access* 11 (2023): 24945-24952.

[YE 21] Ye, Lihao, Xue Ma, and Chenglin Wen. "Rotating machinery fault diagnosis method by combining time-frequency domain features and CNN knowledge transfer." *Sensors* 21.24 (2021): 8168.

[YU 22] Yu, Jie, et al. "Adaptive online extraction method of slot harmonics for multiphase induction motor." *Energies* 15.18 (2022): 6643.

[ZHA 18] Zhang, Xiangyu, et al. "Shufflenet: An extremely efficient convolutional neural network for mobile devices." *Proceedings of the IEEE conference on computer vision and pattern recognition*. 2018.

[ZHA 20] Zhang, Ying, et al. "An enhanced convolutional neural network for bearing fault diagnosis based on time–frequency image." *Measurement* 157 (2020): 107667.

[ZHA 22] Zhang, Jianqun, et al. "A two-stage fault diagnosis methodology for rotating machinery combining optimized support vector data description and optimized support vector machine." *Measurement* 200 (2022): 111651.

[ZHE 12] zhevsky, A., Sutskever, I., and Hinton, G. Imagenet classification with deep convolutional neural networks. In F. Pereira, C.J.C. Burges, L. Bottou, and K.Q. Weinberger, editors, Advances in Neural Information Processing Systems 25, pp. 1097– 1105. Curran Associates, Inc., (2012)

[ZHE 22] Zhe, Yang, Piero Baraldi, and Enrico Zio. "A method for fault detection in multi-component systems based on sparse autoencoder-based deep neural networks." *Reliability Engineering & System Safety* 220 (2022): 108278.

[ZHO 20] Zhou, Yan, et al. "Review of research on lightweight convolutional neural networks." *2020 IEEE 5th Information Technology and Mechatronics Engineering Conference (ITOEC)*. IEEE, 2020.

[ZHI 22] Zhiyuan. Li, et al. "Diagnosis of rotor demagnetization and eccentricity faults for IPMSM based on deep CNN and image recognition." *Complex & Intelligent Systems* 8.6 (2022): 5469-5488.

[ZHU 22] Zhu, Junjun, et al. "Application of recurrent neural network to mechanical fault diagnosis: A review." Journal of Mechanical Science and Technology 36.2 (2022): 527-542